Energy
Advances

ROYAL SOCIETY
OF CHEMISTRY

REVIEW ARTICLE

View Article Online
View Journal | View Issue

Check for updates

Cite this: *Energy Adv.*, 2024, 3, 2704

Controlled synthesis of copper sulfide-based catalysts for electrochemical reduction of CO_2 to formic acid and beyond: a review

Anirban Mukherjee,[a] Maryam Abdinejad,*[b] Susanta Sinha Mahapatra[c] and Bidhan Chandra Ruidas*[a]

Converting carbon dioxide (CO_2) into value-added chemicals is considered as a promising strategy to mitigate climate change. Among the various CO_2 reduction techniques, electrochemical CO_2 reduction (ECO_2R) using renewable energy sources holds significant potential. Consequently, the design and development of electrocatalysts capable of offering both high performance and cost-effectiveness hold the potential to expedite reaction kinetics and facilitate widespread industrial adoption. In recent years, abundant copper sulfide (Cu/S)-based nanomaterials among various metal–chalcogenides have attracted extensive research interest due to their semiconductivity and low toxicity, enabling them to be used in a wide range of applications in the ECO_2R field. This review highlights the progress in engineered Cu/S-based nanomaterials for ECO_2R reactions and elaborates on the correlations between engineering strategies, catalytic activity, and reaction pathways. This paper also summarises the controllable synthesis methods for fabricating various state-of-the-art Cu/S-based structures and outlines their possible implementation as electrocatalysts for CO_2 reduction. Finally, challenges and prospects are presented for the future development and practical applications of Cu/S-based catalysts for ECO_2R to value-added chemicals.

Received 10th May 2024,
Accepted 2nd September 2024

DOI: 10.1039/d4ya00302k

rsc.li/energy-advances

1. Introduction

Since industrialization, the utilization of non-renewable energy sources, which encompass fossil fuels, *i.e.*, coal, crude oil, and natural gas, has tremendously increased.[1] Fossil fuels, as non-renewable energy sources, have two disadvantages: (1) limited supplies cannot meet increasing demands for energy, resulting

Anirban Mukherjee

Mr Anirban Mukherjee completed his Master of Engineering at Jadavpur University, Kolkata. Currently, he is pursuing his PhD as an institute research fellow at the Birla Institute of Technology, Mesra (BIT Mesra), Ranchi 835215, India. His research mainly focuses on synthesizing and characterizing high-performance electrocatalysts for the electrochemical reduction of CO_2 *into value-added products.*

Maryam Abdinejad

Dr Maryam Abdinejad completed her PhD at the University of Toronto, followed by a postdoc at the Delft University of Technology. In 2022 she continued her research as an associate postdoc researcher at the Massachusetts University of Technology (MIT). Her research mainly focuses on the rational design and development of novel high-performance homogeneous and heterogeneous catalysts for the capture and electrochemical reduction of CO_2 *to value-added materials.*

---

[a] *Department of Chemical Engineering, Birla Institute of Technology, Mesra, Ranchi 835215, India. E-mail: bidhanruidas@gmail.com*
[b] *Department of Chemical Engineering, Massachusetts Institute of Technology, 77 Massachusetts Avenue, Cambridge, Massachusetts 02139, USA*
[c] *Department of Chemistry, Birla Institute of Technology, Mesra, Ranchi 835215, India*

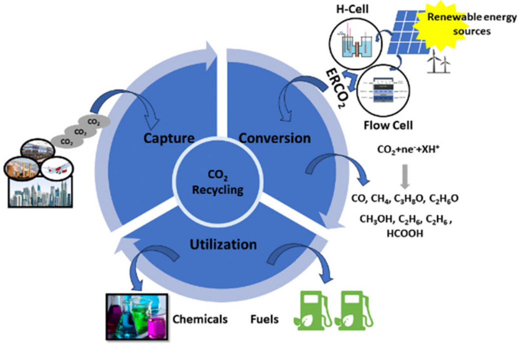

Fig. 1 A graphical illustration of CO_2 capture, utilization, and storage (CCUS).

in a severe energy crisis and (2) the consumption of fossil fuels for energy generation releases a substantial amount of CO_2 into the earth's atmosphere, contributing to global ecological issues such as global warming, global sea level rise, land degradation, and many more.[1–3] To achieve a sustainable future, reducing CO_2 concentrations in the atmosphere is crucial.[4] In this context, the scientific community has made numerous efforts to achieve this goal by using the CO_2 capture, utilization, and storage (CCUS) approach, as depicted in Fig. 1.[5,6] The conversion of CO_2 into C_1 and highly dense C_2 products through chemical routes has been considered a promising technology for reutilizing CO_2.[7,8] It can be achieved by several methods, such as photochemical,[9] electrochemical,[10,11] photo-electrochemical,[12] and biochemical methods.[13] Among these methods, electrochemical CO_2 reduction (ECO_2R) has gained a lot of attention owing to its (a) controllable process parameters (*i.e.*, potential and temperature), (b) feasibility with the reaction environment (*e.g.*, organic and aqueous electrolytes), and (c) ability to scale up.[14,15] Additionally, ECO_2R can be conducted using renewable energy resources such as solar and wind as power sources, allowing for renewable energy storage and redistribution.[16] Therefore, ECO_2R has emerged as a significant research area with industrial prospects, and, in the recent past, much progress has been made in this prospering domain.[17,18]

As reported in the scholarly literature and with the progress of research outcomes, the ECO_2R catalysts are classified into metal and metal-free catalysts based on their design, synthesis, and product selectivity.[19] Nonmetal electrocatalysts are mostly made of carbon-based nanoparticles.[20] On the other hand, metal electrocatalysts include bare metals and their hybrid complexes, such as metal alloys,[19,21,22] metal oxides,[23,24] metal sulfides,[25] and metal complexes.[26,27] The activity and selectivity for the ECO_2R vary with different metal catalysts owing to variations in the activity and adsorption strength of the intermediates.[28] Thus, metal catalysts are further classified into four categories based on their selectivity for final products: (a) Cd, Hg, Tl, Sn, In, Bi, and Pb produce the $HCOO^-$ intermediate, resulting in formate as their primary product;[29–34] (b) Au, Ag, Zn, and Pd produce CO as their main reduction product because of the weak CO adsorption capacity;[35–42] (c) Ni, Fe, Si, V, and Pt produce H_2 owing to the low HER potential;[43–47] and (d) Cu produces up to sixteen carbon-based nanomaterials, comprising several highly energy-dense multi-carbon products, under different conditions.[48,49] Hori *et al.*[50] conducted ECO_2R in 0.5 M $KHCO_3$ at 5 mA cm^{-2} for an hour on various polycrystalline metal electrodes. The outcomes showed that each metal electrode needs a significant overpotential to reach a particular current density (in this case, 5 mA cm^{-2}). Au requires the lowest overpotential (-0.6 V_{RHE}) to obtain CO (87%), but Pb needs the highest overpotential (-1.1 V_{RHE}) to produce formate (97%).[50]

Although significant progress has been made, some challenges still exist with the industrial aspects of ECO_2R,[51,52] such as (1) high overpotential for ECO_2R as CO_2 is a linear molecule that is thermodynamically stable and chemically inert;[53] (2) sluggish kinetics of CO_2 electroreduction because the complex proton-coupled electron transfer (PCET) steps and kinetics of electron transfer were slowed down by the insolubility of CO_2 in the aqueous medium;[54] (3) low exchange current densities; a

Susanta Sinha Mahapatra

Dr Susanta Sinha Mahapatra is an Assistant professor at the Chemistry Department at the Birla Institute of Technology, Mesra, Ranchi, India. He received his MSc in Chemistry and MTech in Energy Science & Technology from Visva-Bharati, Santiniketan, India, and Jadavpur University, Kolkata, India, respectively, and his PhD from Indian Institute Engineering Science & Technology, Shibpur, India. His research mainly focuses on direct alcohol fuel cells, electrochemical supercapacitors, electrochemical CO_2 reduction and hydrogen evolution reactions.

Bidhan Chandra Ruidas

Dr Bidhan Chandra Ruidas completed his PhD in Chemical Engineering at the Indian Institute of Technology Kharagpur, India. Currently, he is working as an Assistant Professor in the Department of Chemical Engineering at the Birla Institute of Technology, Mesra Ranchi, India. His research mainly focuses on enhanced oil recovery and electrochemical reduction of CO_2 to value-added chemicals.

majority of CO_2 electrocatalysts reported thus far operate at less than 20 mA cm^{-2}; however, this is significantly less than those of the commercial electrolyzers, which generally operate at over 70% efficiency at current densities exceeding 200 mA cm^{-2};[55] (4) unsatisfactory selectivity, suggesting expensive separation procedures;[56] (5) catalyst deactivation in less than 100 h, limiting practical application and industrialization of technology;[57] and (6) competitive hydrogen evolution reaction (HER); the HER surpasses the ECO_2R due to its favourable energy conditions at higher overpotentials, leading to a higher FE_{H_2} (faradaic efficiency) than FE for other ECO_2R products.[58] Recently, much research has concentrated on designing and synthesizing innovative, cost-effective, and robust electrocatalysts that can counter these bottlenecks and reduce CO_2 at high rates with minimal overpotential.[57,58]

As pointed out in an earlier paragraph, Cu can electrochemically reduce CO_2 to highly energy-dense C_{2+} products, which has gained massive attention.[59] However, the critical path of the C–C coupling process required for the C_{2+} product formation introduces a high activation energy barrier, resulting in low activity and poor selectivity.[60,61] In this context, synthesizing Cu-based electrocatalysts is crucial for overcoming the energy barrier in ECO_2R. Researchers showed that the CO_2 electroreduction performance (*i.e.*, activity and selectivity) of Cu catalysts is affected by multiple factors. For example, in their work, Hori *et al.*[62,63] showed that Cu with several crystal facets could yield various ECO_2R products. The Cu(111) surface produces methane as a primary product, while C_2 products such as ethylene and ethanol are formed over Cu(100) surfaces. Reske and colleagues[64] also showed that faradaic efficiency and current density of Cu nanoparticles were significant compared to bulk Cu, while Chen *et al.*[65] demonstrated that the single-atom Cu showed better ECO_2R performance than other reported Cu-based materials, *i.e.*, bulk metal Cu.

Moreover, bimetallic Cu-based electrocatalysts have shown promise in enhancing copper's selectivity and overall catalytic performance. For example, Burdyny's group[58] could electrochemically reduce CO_2 to formate as the primary product using bimetallic Cu–Pd with a faradaic efficiency of 93% and a current density of 150 mA cm^{-2} at a cell potential of $-2.9\ V_{RHE}$ using a zero-gap flow cell, also known as the membrane electrode assembly cell. They successfully demonstrated how the engineering design of an electrochemical cell, coupled with catalyst structure, achieves the highest overall reported energy efficiency (EE) for formate production at 47%. These results show the benefit of using non-post-transition metals as primary catalysts for formate production. Another study shows that catalyst morphology is also essential: Chorkendorff *et al.*[66] found that metallic Cu with varying surface roughness exhibits distinct selective ECO_2R product formation. They discovered that the Cu nanoparticle-coated electrocatalysts have improved hydrocarbon selectivity compared to non-coated electrocatalysts. Motivated by the aforementioned work, several research groups synthesized different morphologies, such as nanowires,[67,68] films,[69] microcubes,[70,71] core–shell,[72,73] and Cu-based bimetallic[58] catalysts and studied their catalytic activity towards ECO_2R. They showed that the catalytic activity of Cu-based catalysts towards ECO_2R can be remarkably enhanced by tailoring the catalysts' structure and morphology.

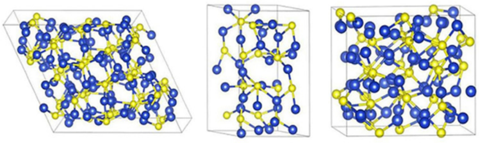
(a) Low-Chalcocite Cu_2S (b) High-Chalcocite Cu_2S (c) Cubic-Chalcocite Cu_2S

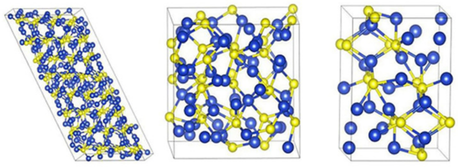
(d) Djurleite $Cu_{1.94}S$ (e) Digenite $Cu_{1.8}S$ (f) Anilite $Cu_{1.75}S$

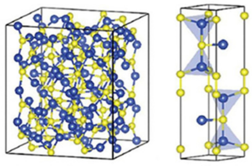
(g) Roxbyite $Cu_{1.81}S$ (h) Covellite CuS

Fig. 2 Crystal structures of some representative copper sulfide phases. Blue spheres – copper atoms and yellow spheres – sulfur atoms, surrounded by black lines showing each unit cell boundary ((a)–(f) reproduced with permission from ref. 95, copyright American Institute of Physics 2012 and (g) and (h) reproduced with permission from ref. 77, copyright RSC 2019).

In recent years, Cu/S-based nanomaterials have gained significant attention as electrocatalysts due to their p-type semiconducting, earth-abundance and nontoxic characteristics. Various phases of copper sulfide are reported in the literature, namely chalcocite (Cu_2S), djurleite ($Cu_{1.97}S$), digenite ($Cu_{1.80}S$), anilite ($Cu_{1.75}S$), geerite ($Cu_{1.60}S$), spionkopite ($Cu_{1.40}S$), yarrowite ($Cu_{1.12}S$) and covellite ($Cu_{1.00}S$) as copper-rich systems, while villamanite (CuS_2) as a sulfur-rich system and covellite (CuS) as a 1/1 system, usually denoted as $Cu_{2-x}S$ having minimal values of x.[74–77] Based on the packing of sulfur atoms in the lattice, the aforementioned crystal structures have been grouped into three categories, as illustrated in Fig. 2, specifically cubic close packing (anilite and digenite), close hexagonal packing (djurleite and chalcocite), and a combination of close hexagonal packing and covalent bonding of the sulfur atoms (covelline).[77] But for the remaining forms, *i.e.*, yarrowite, spionkopite, and geerite, crystal structures remain unknown. It is to be noted that copper sulfides' electrical conductivity depends on their phases, decreasing from copper-deficient to copper-rich.[78,79] For example, it has been observed that at 1.63 K, the naturally occurring covellite phase of CuS exhibits exceptional electrical conductivity.[80] Therefore, owing to their unique versatile properties, copper sulfides are fascinating nanomaterials for various applications, *i.e.*, optoelectronic devices,[81] photocatalysis,[82] photovoltaic cells,[83] sensors,[84] battery electrodes,[85] and biomedical applications.[86] Thus, numerous studies have focused on the engineering strategies of these materials for modifying their properties, including the electronic structure modulation for ECO_2R. Notably, developing ECO_2R catalytic systems that can overcome bottlenecks is becoming an essential topic with the increasing use of this electrocatalytic technology. According to the reported literature, a variety of physical[87] and chemical[75] methods, such as hydrothermal and solvothermal,[88,89] ball-milling,[90] electrodeposition,[91] microwave irradiation,[92] thermolysis,[93] and template-assisted[94,95] approaches, have been widely used for constructing different nano-dimensional (*i.e.*, zero-dimensional, one-dimensional, two-dimensional, and three-dimensional) Cu/S-based nanomaterials. So far, several synthetic processes have yielded various shapes of Cu/S-based nanostructures, such as nanoparticles, nanoplates, hollow spheres, nanorods, nanowires, nanotubes, nanosheets, *etc.* Therefore, the significant connections within several nanomaterials and their distinct properties have prompted research into the controlled fabrication of valuable electrocatalysts with altered nanostructures.

Until recently, many outstanding review articles on Cu/S-based nanomaterials for several energy applications have been published,[74,79,96] including the preparation, characterization methods, and the effects of modification strategies on catalytic activity. However, an in-depth and systematic investigation of synthesis strategies of Cu/S-based electrocatalysts and electron modulation effects on ECO_2R is lacking and is desired. This review summarizes the most recent advancements in Cu/S-based catalysts for ECO_2R reactions and outlines the connection between catalytic efficiency and several engineering approaches. The primary section discusses various modification strategies for Cu/S-based nanomaterials. After this, the effects of these strategies on electron modulation will be summarized. This fundamental understanding can help with the design of high-efficiency ECO_2R catalysts. Finally, this article highlights the research challenges and future prospects of Cu/S-based nanomaterials for ECO_2R.

2. Characteristics for improving the ECO_2R performance of Cu/S-based catalysts

This section discusses the essential features of Cu/S-based catalysts to understand their fundamental characteristics, which are mentioned below in each subsection.

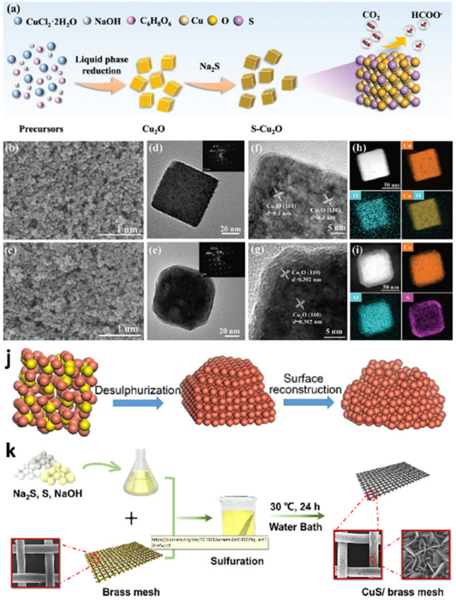

Fig. 3 Synthesis and morphological characterization. (a) Schematic illustration of the electrocatalyst preparation process. SEM images of (b) S0-Cu_2O-70 and (c) S3-Cu_2O-70. TEM images of (d) S0-Cu_2O-70 and (e) S3-Cu_2O-70 (the inset shows the selected area electron diffraction (SAED) patterns). HRTEM images of (f) S0-Cu_2O-70 and (g) S3-Cu_2O-70. The corresponding elemental mappings of (h) S0-Cu_2O-70 and (i) S3-Cu_2O-70 (reproduced with permission from ref. 99, copyright Wiley-VCH GmbH 2023). (j) Diagrammatic representation of the conversion from $Cu_{2-x}S$ to Cu-s (reproduced with permission from ref. 100, copyright Springer Nature 2021). (k) Diagrammatic representation of the CuS NS arrays/BM synthesis method (reproduced with permission from ref. 101, copyright ACS 2021).

2.1 Exposed facets for improving electrocatalytic performance

As reported by many literature studies, tuning the exposed facets of nano-electrocatalysts may alter atomic rearrangements, reaction intermediate affinity, and surface energy, influencing the electrochemical activity.[97,98] Inspired by this, a research group presented a simple and effective technique for limiting product distribution using sulfur-modified Cu_2O electrocatalysts.[99] A wet chemical technique was used to synthesize distinct morphologies of Cu_2O effectively with varied exposed facets (Fig. 3a). Surprisingly, they observed that the faradaic efficiency of formate on sulfur-modified Cu_2O electrocatalysts was significantly sensitive to Cu_2O crystal facets, as shown in Fig. 3b–i, with selectivity in the order of $Cu_2O(100) > Cu_2O(100)/(111) > Cu_2O(111)$. Among all the sulfur-modified Cu_2O electrocatalysts prepared, the optimized S3-Cu_2O-70 demonstrated a FE of 90% at $-0.9\ V_{RHE}$ and an extended stability of more than 80 h in an H-type cell. Furthermore, a flow-associated cell system achieved a $j_{formate}$ of 260 ± 16 mA cm^{-2}, outperforming most formate-producing Cu-based electrocatalysts. Sulfur can improve water activation for synthesizing unique H_2 species and reduce the activation energy of *OCHO intermediate formation on the surface of sulfur-modified Cu_2O, boosting formate selectivity in ECO_2R, according to experimental data and density functional theory (DFT) calculations. Similarly, He *et al.*[100] investigated the role of rich high-index facets of polycrystalline Cu (Cu-s) nanoparticles successfully derived from $Cu_{2-x}S$ nanocrystals, as illustrated in Fig. 3j. They observed that the formation of high-index facets during surface reconstruction is beneficial for providing surface active sites for C–C coupling, thus boosting C_2H_4 generation. The Cu–S nanocatalysts exhibited high catalytic performance with an FE of 68.6% (a $j_{C_2H_4}$ of 40.8 mA cm^{-2}) for C_2H_4 because of vicinal facet formation during surface engineering. Furthermore, *in situ* studies demonstrated that Cu–S electrocatalysts use the *COCHO intermediate route for producing C_2H_4 *via* ECO_2R. Similarly, Dou *et al.*[101] investigated the facet-dependent selectivity and activity of CuS nanosheet arrays on brass mesh for ECO_2R prepared *via* a facile and green chemical bath deposition approach (Fig. 3k). Meanwhile, connecting CuS with BM increased overall performance (j = 75 mA cm^{-2} at -0.7 V_{RHE} and FE_{HCOO^-} = 67.8 ± 1%) for ECO_2R. Instead, PTFE-coated CuS/BM achieved more enhanced CO_2 conversion to generate HCOOH/$HCOO^-$ (FE = 70.2 ± 1% at 0.7 V_{RHE}) than CuS/BM. Their investigations reveal that the reconstruction of CuS/BM resulted in a uniform nanowire framework with abundant active surfaces during the ECO_2R, considerably increasing catalytic reactivity. They integrated DFT research with experimental findings. The work attributes the high selectivity for $HCOO^-$ production to the reconstructed formation of the Cu(111)/CuS(102) facets throughout the electrolysis process. According to the theoretical investigation, S under the CuO layer reduces the binding energies of HCOO* and *COOH on Cu(111)/CuS(102) compared to the Cu(111) plane, allowing the development of HCOOH or HCOO*.

2.2 Edge engineering for improving electrocatalytic performance

Recent research has established that the exposed edges of transition metal chalcogenides are more catalytically active than planar surfaces in electrochemical reactions.[102,103] The more exposed edges on the electrode/electrolyte interfaces can improve the electrochemical performance owing to more active sites. Owing to the sufficiently exposed-edge planes, the hierarchical hollow CuS microcubes (MCs) exhibited remarkable electrocatalytic properties for CO_2 reduction with a FE_{CO} of 32.7% at a lower onset potential of -0.2 V_{RHE}. Shao *et al.*[104] reported a novel engineered surface and morphology-enhanced exposed edge sites, offering significantly higher electrocatalytic activities and selectivity toward ECO_2R. They demonstrated CO_2 electro-reduction with lower overpotential for hollow CuS microcubes (MCs). According to the morphological characterization, it has been shown that as-synthesized h-CuS MCs lead to a higher density of defective edge exposed sites, essential for enhanced conversion activity and selectivity.

2.3 Porosity effect for improving electrocatalytic performance

Owing to their high specific surface areas, nanoporous structures significantly accelerate surface reactions and facilitate mass transfer by enhancing contact between the electrolyte and the active site.[105] The adsorption and transformation of intermediates, the release and diffusion of gas products, and the lowering of electron transfer resistance are all significantly more accessible by the active sites of the nanoporous structures.[106,107] Inspired by this, Li *et al.*[108] designed and synthesized hollow-ordered porous copper sulfide cuboctahedra (HOP CuS-CO) with regulated shell thicknesses, as shown in Fig. 4a–h, to selectively produce formate from ECO_2R. The hollow shells of HOP CuS-CO possess uniformly distributed and interconnected pores. With these advantages and benefits of porous cages, the HOP CuS-CO catalyst exhibited an exceptional $FE_{formate}$ of 70.3% with stability of up to 26 h at a potential of -1.1 V_{RHE}. *In situ* Raman spectroscopy studies showed that the HCOO* intermediate adsorption energy is favourable on the surfaces of HOP CuS-CO by a spatial confinement effect, resulting in highly effective ECO_2R for formate generation.

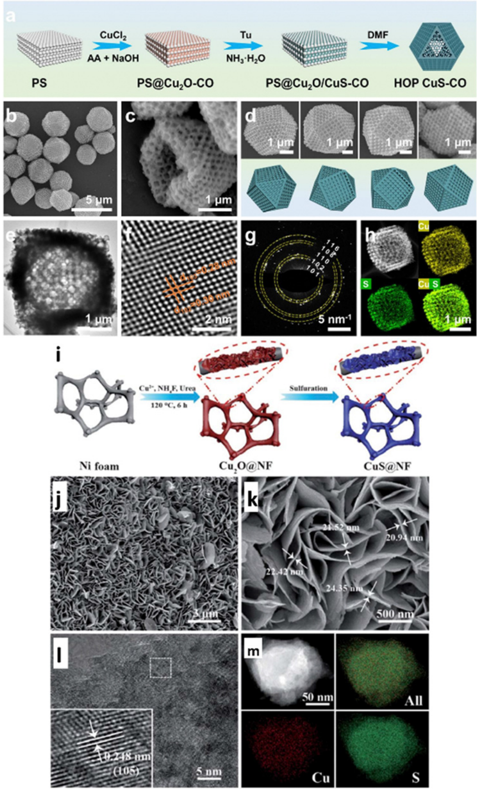

Fig. 4 (a) Schematic illustration of synthesis of HOP CuS-CO. (b) SEM image of HOP CuS-CO. (c) SEM images of one individual HOP CuS-CO crystal projected from four different directions. (d) SEM image of partially broken HOP CuS-CO particles. (e) TEM and (f) HRTEM images and (g) SAED patterns of HOP CuS-CO. (h) HAADF-STEM image and the corresponding elemental maps of Cu (yellow) and S (green) (reproduced with permission from ref. 108, copyright Elsevier 2024). (i) Schematic illustration of synthesis of CuS@NF samples. (j and k) SEM images of CuS@NF samples with lower and higher magnification. (l) HR-TEM and (m) HAADF STEM images and corresponding EDS elemental mapping of CuS@NF samples. (reproduced with permission from ref. 110, copyright RSC 2017).

The above studies provided insights into designing novel morphologies for more outstanding formate production using ECO_2R. Recently, Yabuki *et al.*[109] employed the thermal breakdown of a sulfur and copper–amine complex ink to create copper sulfide film electrodes. Furthermore, the XRD study confirmed that $Cu_{1.8}S$ and CuS nanoparticles were present in the film. The copper sulfide film possessed variations in the surface area caused by the film's micropores, resulting in ECO_2R to CO, CH_4, and C_2H_4, with a more significant percentage of C_2H_4 (C_2 product) than a copper electrode.

Zhu *et al.*[111] synthesized highly porous Cu_2S-decorated copper foam (Cu-foam), an active CO_2 reduction electrocatalyst, in an H-cell system. They used anodization followed by a heat treatment process to deposit Cu_2S nanoarrays on Cu foam. Anodization was placed in the first phase in an electrocatalytic cell, employing platinum foil as the cathode and Cu-foam as the anode in an aqueous Na_2S solution. After the anodization, the anodized Cu-foam was washed multiple times with distilled water, followed by thermal treatment. The 3D-shaped Cu_2S/Cu-foam electrode produces much more HCOOH (FE_{co} = 85% with

j = 5.3 mA cm^{-2} at −2.0 $V_{Ag/AgCl}$) than the Cu-foam (FE_{co} = 38.9% at −1.8 $V_{Ag/AgCl}$). Using a simple hydrothermal procedure, Zhao *et al.*[110] efficiently fabricated economical, robust and highly porous CuS nanosheet arrays successfully decorated on a porous nickel foam support, as illustrated in Fig. 4i, for ECO_2R activity. The CuS nanosheet is highly dense and is evenly dispersed over the highly porous Ni foam structure, forming a 3D organized foam CuS/NF, as shown in Fig. 4j–m. The thicknesses of the highly porous CuS/NF framework range from 20 to 25 nm. Their findings revealed that S concentration in the electrodes facilitates CO_2 adsorption and speeds up the rate-limiting step by converting CO_2 to $CO_2^{\bullet-}$ intermediates. Next, the $CO_2^{\bullet-}$ intermediate produces CH_4 by PCET reaction. Thus, CuS@NF achieved an extraordinary faradaic efficiency of 73.5% at −1.1 V_{RHE} for CH_4 formation and was stable up to 60 h.

3. Emerging regulations for improving the ECO_2R activity

3.1 Phase effect for improving electrocatalytic performance

This section discusses the ECO_2R activity of catalysts, which is determined by the final stage of the active metal's conversion, not the initial phase.[112–114] Notably, Cu/S-based materials typically act as pre-catalysts for ECO_2R due to their conversion to oxide form during electrolysis. Due to their high oxidation potential, Cu/S-based materials could be almost totally/partially transformed into their oxide species.[115,116] For example, Chen *et al.*[117] observed that during the ECO_2R, copper sulfide nanoflowers (Fig. 5a and b) undergo restructuring to metallic Cu (Fig. 5c), and S^{2-} ions are released into the electrolyte and adsorbed on the surface of Cu catalysts. This phenomenon suppressed the formation of other hydrocarbon products, resulting in high selectivity towards HCOOH during ECO_2R. Copper sulfide pre-catalysts with high S content may absorb more S^{2-} ions on the Cu surface, resulting in higher FE_{HCOOH}. To assess this hypothesis, they used copper foil as the electrode and added varying amounts of K_2S to the $KHCO_3$ electrolyte. Later, they discovered that the FE_{HCOOH} of copper gradually increased with increasing K_2S concentrations. In this context, Phillips *et al.*[118] used *in situ* electro-reduction to investigate selective formate production over copper sulfide-derived copper surfaces (S-derived copper) (Fig. 5d–i). As evidenced by surface-enhanced infrared absorption (SEIRA) spectroscopy, the aforementioned electrocatalyst reduces H_2 and CO formation while enhancing formate selectivity. The authors interpreted this increase in formate selectivity by describing a plausible reaction mechanism in which the active sites are occupied by CO_{ads}, preventing the adsorbed hydrogen molecules (H_{ads}) from combining and producing an H_2 molecule. As a result, H_{ads} could only generate H_2 in solution by making bonds with protons *via* PCET. Theoretical simulations suggest that H_{ads} might create HCOOH by reacting with a solution-phased-CO_2 molecule rather than an H^+-containing solution. As a result, H_{ads} molecules adsorbed on S-derived Cu surfaces and generated HCOOH by interacting with solution-phase CO_2 *via* PCET.

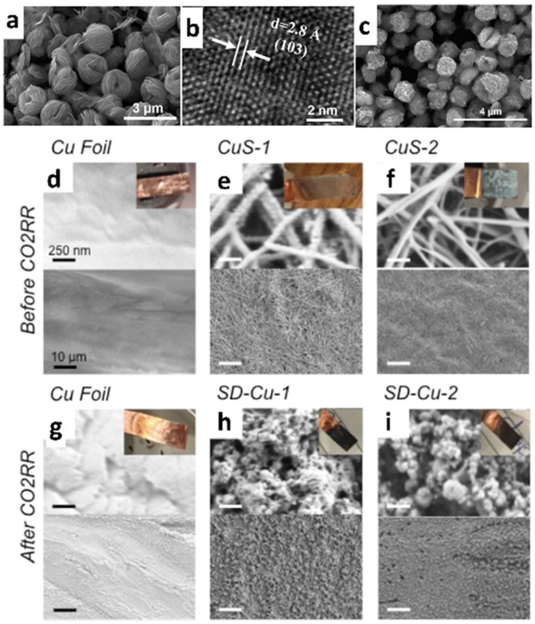

Fig. 5 (a) SEM image and (b) HR-TEM image of CuS nanoflowers before ECO_2R; (c) SEM image of CuS nanoflowers after ECO_2R (reproduced with permission from ref. 117, copyright Elsevier 2024). SEM image of catalyst surfaces (d)–(f) before and (g)–(i) after ECO_2R. (d) and (g) Copper foil, (e) and (h) copper sulfide (CuS) electrodeposited for 30 min (CuS-1), and (f) and (i) CuS electrodeposited for 2 h (CuS-2). The CuS samples convert to SD-Cu after ECO_2R (top scale bars – 250 nm and bottom scale bars – 10 μm for each panel, reproduced with permission from ref. 118, copyright ACS 2018).

In a different work, through a straightforward two-step coupling procedure *via* a hydrothermal method followed by pyrolysis, as illustrated in Fig. 6a, Zhang *et al.*[119] created a $Cu_{1.81}S$ catalyst supported by a multi-walled carbon nanotube (MWCNT). Due to the highly active sites of the uniformly dispersed $Cu_{1.81}S$ particles and the effective electron transport and active sites provided by the MWCNT, the $Cu_{1.81}S$@MWCNT-600 composite catalyst (Fig. 6b–e) was able to achieve superior ECO_2R performance with 30 h stability during continuous operation. Later, they reported that $Cu_{1.81}S$@MWCNT-600 ($Cu_{1.81}S$@MWCNT-600-OD) with oxide modification showed improved catalytic activity and had a high $FE_{Formate}$ of 82%. According to the authors, copper oxide, which changed the phase into a needle-shaped structure during ECO_2R, provided more active sites and improved electrocatalytic activity (Fig. 6f–i). In another work, Oversteeg *et al.*[120] investigated the role of phase engineering *via* Cu_{2-x}s derived copper sulfide-supported carbon (CuS/C and Cu_2S/C) (Fig. 6j, m and n) ECO_2R catalysts synthesized using the liquid phase sulfidation of CuO/C nanoparticles (Fig. 6l and o). All the prepared phases are confirmed by XRD analysis, as shown in Fig. 6k. According to the electrochemical and *in situ* X-ray absorption (XAS) spectroscopy investigations, the metallic Cu reduction occurs in CuS@C and Cu_2S/C nanoparticles during electrochemical CO_2 reduction (Fig. 6p and q). Later, their observation revealed that CuS/C- and Cu_2S/C-derived catalysts had higher selectivity towards creating formate at low current densities than the CuO/C-derived electrocatalyst. Surprisingly, the catalyst only needed less

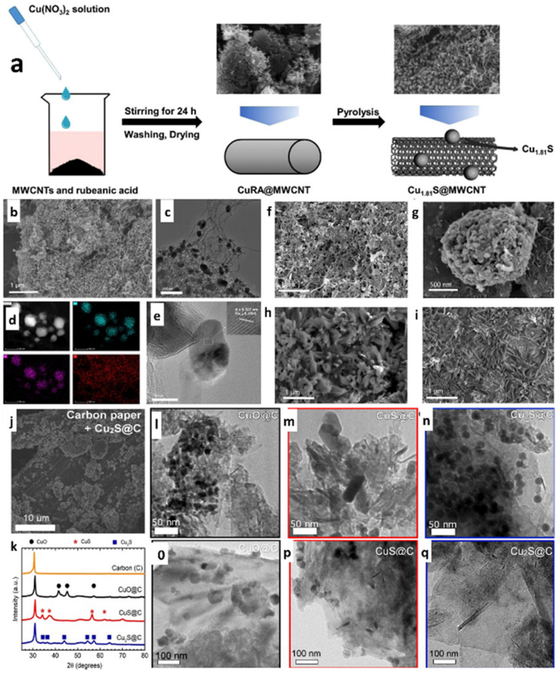

Fig. 6 (a) Schematic illustration of the preparation of $Cu_{1.81}S$@MWCNT. (b) SEM and (c) TEM images of $Cu_{1.81}S$@MWCNT-600. (d) HAADF-STEM image and the corresponding EDS maps revealing the uniform distribution of Cu (blue) and S (purple) in the $Cu_{1.81}S$ particles. (e) HRTEM image of $Cu_{1.81}S$@MWCNT-600. SEM images of used $Cu_{1.81}S$@MWCNT-600-OD after (f) 10 min, (g) 20 min, (h) 1 h, and (i) 20 h of ECO_2R (reproduced with permission from ref. 119, copyright Elsevier 2020). (j) SEM images of the carbon paper substrate with Cu_2S@C deposited on the carbon fibres by spraying. (k) XRD patterns of the bare GNP-500 carbon support (orange) and of CuO@C (black), CuS@C (red) and Cu_2S@C (blue) nanoparticles on this carbon support. TEM images of (l) CuO@C, (m) CuS@C and (n) Cu_2S@C nanoparticles before electrolysis; TEM images of the (o) CuO@C-, (p) CuS@C-, and (q) Cu_2S@C-derived catalysts after 5 h of ECO_2R (reproduced with permission from ref. 120, copyright Elsevier 2021).

carbon surface coverage (<4%) for total formate selectivity to achieve the highest FE (12%). The efficiency of formate generation in ECO_2R can be increased using sulfur-derived copper with carbon catalysts.

An interesting approach has been reported recently, in which they created a series of CuS catalysts using different precursors and examined the relationship between phase restructuring and ECO_2R catalytic activity during electrolysis. First, Guo *et al.*[121] employed hydrothermal synthesis to create several CuS-based catalysts using different sulfur precursors (*i.e.*, TU = thiourea, STS = sodium thiosulfate, TAA = thioacetamide, and SS = sodium sulfide). Surprisingly, in terms of ECO_2R activity, CuS-TU outperformed the other electrodes (*i.e.*, CuS-STS, CuS-TAA, and CuS-SS) in CO_2-saturated 0.1 M $KHCO_3$ electrolytes, with an FE_{CO} of 72.67% (-0.51 V_{RHE}) and a high CO selectivity. They hypothesized that the thiourea precursor's rapid S decomposition led to a higher concentration of dissolved S^{2-} in the electrolyte, enabling quicker nucleation and restructuring of a nanoflower like CuS–thiourea electrocatalyst for more enhanced mass transfer kinetics and favourable ECO_2R.

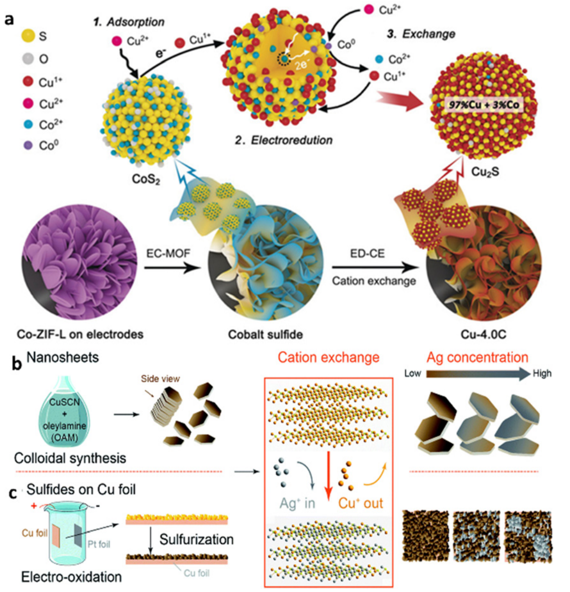

Fig. 7 (a) Schematic illustration of the experimental pathways and mechanisms for electrochemically driven cation exchange (ED-CE). Synthetic strategies for Ag/Cu sulfide catalysts (reproduced with permission from ref. 122, copyright Wiley-VCH 2020). (b) Cu sulfide nanosheets (C-nano-0, 100 nm lateral dimension, 14 nm thick) were obtained through colloidal synthesis with CuSCN in oleylamine (OAM). (c) Cu sulfides on Cu foil (C-foil-*x*) were obtained through electrooxidation in 1 M NaOH to produce an oxide layer of a few 10 s of microns thick, followed by sulfurization with 0.1 M Na_2S. After cation exchange where Ag^+ replaces the Cu^+ in the Cu sulfides, Ag/Cu sulfide nanosheets (CA-nano-*x*) remain in nanosheet structure with some distortion in shape as the Ag/Cu mass ratio ranges from 0.3 to 25, while for C-foil-*x*, Ag nucleates at higher Ag concentration, which impedes the uniform distribution of Ag and Cu (reproduced with permission from ref. 123, copyright RSC 2021).

The phase engineering of a target nanocrystal (NC) can be systematically varied by carefully substituting metal cations in a prefabricated NC template using an emerging electrochemically driven cation exchange (ED-CE) approach. He and coworkers[122] recently designed a Cu_2S catalyst for ECO_2R from the CoS_2 template *via* the ED-CE approach (Fig. 7a). Employing the ion exchange process, Cu almost entirely replaces Co cations in CoS_x, and the Cu/S atomic ratio is ~2.4. The Cu_2S catalyst produced by converting the predesigned template retains the initial morphology of CoS_2 by preserving its high grain-boundary density, improving CO_2 adsorption. Also, the electronic structure of the nearby Cu sites has changed due to electronegative S heteroatoms, creating positively charged Cu^+ sites. The primary formate intermediate, *OCHO species, is formed when partially positive-charged Cu sites adsorb CO_2 molecules with more electronegative oxygen. The as-prepared 3D-shaped Cu_2S catalysts showed an FE of 87% with a current density of 19 mA cm^{-2} at -1.9 V_{RHE} in a 0.1 M $NaHCO_3$ medium for CO_2 conversion to HCOOH. Li *et al.*[123] utilized copper sulfide nanosheets as a template to develop Ag/Cu electrocatalysts through a straightforward ED-CE process (Fig. 7b and c). When the Ag^+ concentration in the exchange solution increased, the crystal structure of $Cu_{2-x}S$ nanosheets with lateral dimensions of 100 nm and a thickness of 14 nm progressively changed from Cu_7S_4 to Ag_2S (CA-nano-*x*, cation-exchanged nanosheets, where *x* indicates a higher concentration of Ag). The Ag/Cu mass ratio varied between 0.3 and 25. Hence, at an average overpotential ($-0.2\ V_{RHE}$), both C-nano-0 and CA-nano-*x* exhibited outstanding FE_{HCOOH}. Surprisingly, when the Ag content increases, formate-producing C-nano-0 can generate C_{2+} products at $-1.0\ V_{RHE}$. This observation concludes that the nanosheets show shape distortion as the Ag content rises while maintaining their original morphology after the cation exchange process.

In 2024, Goh *et al.*[124] investigated phase-engineered sulfide-derived Cu–Sb electrodes for electrochemical CO_2 conversion in a gas diffusion electrode (GDE) based cell. They synthesized several distinct Cu–Sb–S phases, skinnerite (SK; Cu_3SbS_3), tetrahedrite (TH; $Cu_{12}Sb_4S_{13}$), and chalcostibite (CS; $CuSbS_2$) using a heat-up colloidal nanoparticle route, as illustrated in Fig. 8a–f, and each showed a different selectivity for ECO_2R with CO as the main product, which contrasts with the individual CuS_x and SbS_x control samples, which show a preference for the formate product. They also demonstrated that the different elemental compositions caused the different selectivity patterns when the parent phases were reduced using fundamental composition characterization after reduction. Interestingly, lower Cu concentrations reduce phase segregation into harmful S-doped Cu that converts CO_2 to HCOO and H_2, whereas higher sulfur concentrations disrupt crystallinity and promote CO formation. This outstanding performance is attributed to the tetrahedral Cu–Sb–S sample, which has the highest residual sulfur, with a CO_{FE} of about 80.5% at $-1.0\ V_{RHE}$ and a $j_{geometrical}$ of 37.6 mA cm^{-2}. Post-electrocatalysis characterization combined with DFT calculations demonstrated that adding sulfur to Sb sites enhances *COOH binding compared to *CO, rupturing scaling relations and aiding in CO(g) formation afterwards.

Similarly, in 2023, Mai *et al.*[125] used a facile solvothermal technique to create several cuprous sulfide nanoparticle-modified copper hydroxide nanowire array (S-CNW) pre-catalysts for elucidating the reaction mechanism of ECO_2R (Fig. 8g–n). They explored the effect of cuprous sulfide nanoparticle modification on formate generation during CO_2 reduction and observed sulfur modification changes in the intermediate during CO_2 reduction, leading to improved formate selectivity (60% of FE_{co} with j_{HCOO^-} = 10 mA cm^{-2} at $-0.58\ V_{RHE}$). Therefore, the role of trace sulfur alteration of copper surfaces in selective formate production is investigated using DFT. According to the study, sulfur modification in copper, as compared to a pure copper surface, can accelerate the synthesis of *OCHO, a critical step along the formate pathway.

3.2 Size effect for improving electrocatalytic performance

Researchers discovered that the surface of tiny nanoparticles is rich in unsaturated atoms and defective sites compared to the bulk, exposing the number of active sites to improve catalytic activity.[126] Reducing nanoparticles even further to nanoclusters (NCs), which are made up of a few hundred or fewer atoms and have an average size of about 2 nm, reveals intriguing electrochemical performance with significant quantum size effects.[127] Shinagawa *et al.*[128] used a wet chemistry approach to create carbon-supported CuS nanocatalysts by controlling the size. The experimental investigation demonstrated that during ECO_2R the aforementioned nanometric-sized CuS was restructured and reformed to S-modified copper (Cu–S). As a result, at considerable overpotential (−0.8 V *vs.* RHE), Cu–S catalysts produced formate with an FE of >60% and negligible quantities of CO as a byproduct. They discovered that as the particle size dimension became 3 nm to 20 nm, there was a slight increase in HCOOH production, highlighting the catalytic size–activity relationship. Following this, in a similar article, it was demonstrated that solvothermally prepared submicron-sized CuS electrodes had better FE_{HCOOH} (80%) for ECO_2R to HCOOH than nanometric CuS (FE_{HCOOH} > 60%), indicating the important link between the particle size and electrochemical activity. Later, Lim *et al.*[129] studied the impact of size engineering by fabricating a size-controlled CuS_x electrocatalyst in an aqueous medium using Cu foil dipped in industrial CO_2 that contains H_2S (Fig. 9a–c). As per their observations, the Cu foil and the sulfur interacted appropriately when the concentration of sulfur in the solution increased. The simultaneous interactions raised the average particle size and surface sulfur density of CuS_x nanoparticles (NPs) to 133.2 ± 33.1 nm and 86.2 ± 3.3%, respectively, as shown in energy dispersive X-ray spectroscopy (EDX) images (Fig. 9c). When the sulfur percentage and sizes of the CuS_x nanoparticles increased steadily, the $FE_{Formate}$ improved from 22.7 to 72.0% at $-0.6\ V_{RHE}$ (Fig. 9d–g). Although the CuS_x nanocatalysts had a lower current

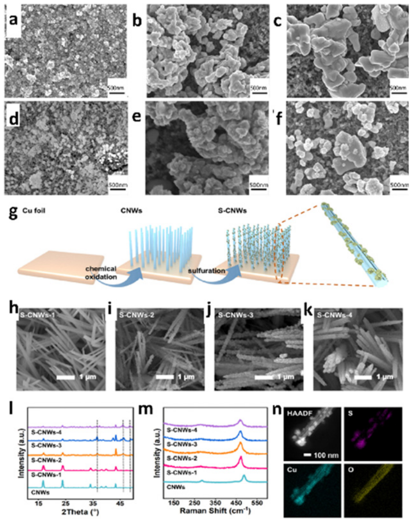

Fig. 8 SEM characterization of the samples before reduction. (a)–(c) SEM images of the samples SK (a), TH (b) and CS (c) sprayed on carbon paper. SEM characterization of the samples after reduction. (d)–(f) SEM images of the samples SK (d), TH (e) and CS (f) sprayed on carbon paper (reproduced with permission from ref. 124, copyright RSC 2024). Morphological and structural characterization; (g) schematic illustration of S-CNW preparation, (h)–(k) SEM images of S-CNWs with different loadings of TAA at 75 °C for 0.75 h, (50, 75, 100, and 200 mg per 80 mL) for S-CNWs-1, S-CNWs-2, S-CNWs-3, and S-CNWs-4, respectively; (l) XRD patterns of CNWs and S-CNWs with different degrees of vulcanization, (m) Raman spectra of CNWs and S-CNWs with different degrees of vulcanization, (n) HAADF-STEM and the corresponding EDS images of S-CNWs (reproduced with permission from ref. 125, copyright ACS 2023).

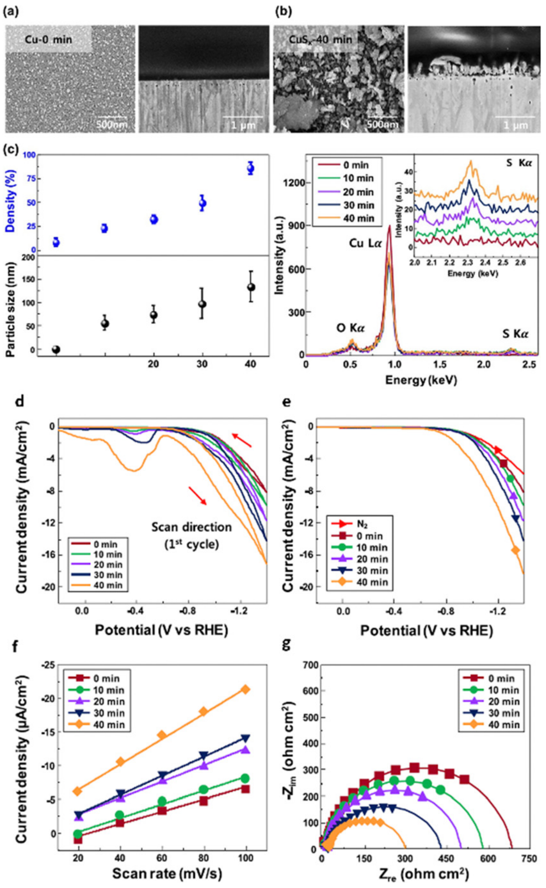

Fig. 9 Top-view and cross-sectional SEM images of (a) Cu-0 min without sulfur species and (b) CuS$_x$-40 min catalysts. (c) The average particle size and surface density of CuS$_x$ NPs were calculated using a computing-based image analyzer and EDX spectra of Cu and CuS$_x$ catalysts. (d) CV (1st scan) of CuS$_x$ catalysts with different amounts of sulfur species. (e) LSV curves in N_2-purged and industrial CO_2-purged 0.1 M $KHCO_3$ electrolytes at a scan rate of 50 mV s^{-1}. (f) Current density plots at various CV scan rates. The current densities were obtained from the double-layer charge/discharge curves at 0.40 V_{RHE} in industrial CO_2-purged 0.1 M $KHCO_3$ electrolyte. (g) Nyquist impedance plots of catalysts in industrial CO_2-purged 0.1 M $KHCO_3$ electrolyte from 1 MHz to 0.1 Hz with 30 mV amplitude at −0.6 V_{RHE} (reproduced with permission from ref. 129, copyright ACS 2020).

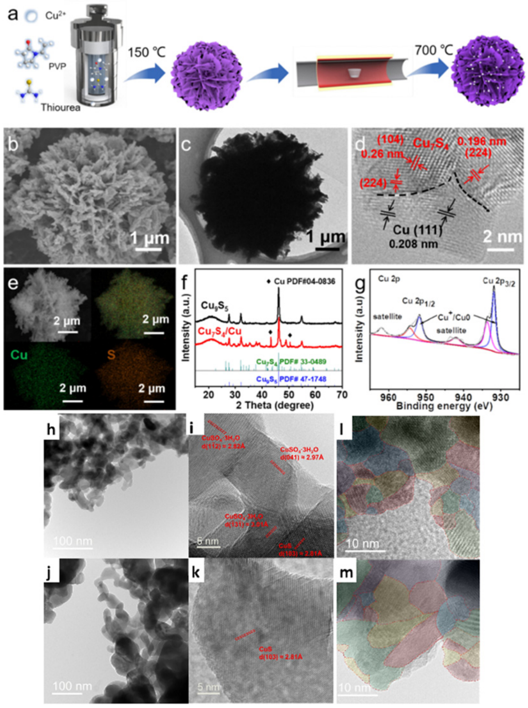

Fig. 10 (a) Schematic illustration of the synthetic process, (b) SEM image, (c) TEM image, (d) HRTEM image, (e) EDS elemental mapping, and (g) XPS pattern of Cu_7S_4/Cu. (f) XRD patterns of Cu_7S_4/Cu and Cu_9S_5 (reproduced with permission from ref. 134, copyright Wiley-VCH 2024). Morphological and structural characterization of CuS 811 and CuS MKL before ECO_2R by electron imaging. (h) and (i) Aberration-corrected TEM images of (h) CuS 811 and (i) CuS MKL. (j) and (k) HRTEM images of (j) CuS 811 and (k) CuS MKL. The crystal facets with heterogeneous species are highlighted in (j) and (k). Structural characterisation of CuS 811 and CuS MKL post ECO_2R by electron imaging. (l) and (m) HRTEM images of (l) CuS 811 and (m) CuS MKL. Red dash-dotted lines highlight the boundaries of induced grains, and the grains with heterogeneous lattice fringes are marked in various colours (l) and (m). The marking colours are only used to distinguish every grain, and there is no correlation between the colour and phase (reproduced with permission from ref. 135, copyright Wiley-VCH 2024).

density, the 72-hour stability must be addressed for industrial CO_2 conversion.

3.3 Grain boundary effect for improving electrocatalytic performance

Grain boundaries (GBs) can be efficient active sites for catalytic processes because they provide an electrodynamically beneficial surface.[130,131] Also, it has been shown that catalytically energized surfaces can be stabilized using grain boundaries (GBs).[132,133] For example, Yang *et al.*[134] used electrochemical reduction techniques to synthesize S-Cu_2O/Cu hybrid catalysts derived from Cu_7S_4/Cu nanoflowers (Fig. 10a–g). They showed that GB surface defects in Cu_2O/Cu interfaces were more energized than grain surfaces for ECO_2R. They observed that Cu_7S_4/Cu is dynamically restructured *in situ* to provide an S-Cu_2O/Cu hybrid catalyst for efficient ECO_2R to formate with a FE_{HCOOH} of up to 70% at −1.0 V_{RHE} and a partial current density of 5 mA cm^{-2}), thus outperforming Cu_2O/Cu and Cu_7S_4. The authors attributed this performance to (i) thermodynamic and experimental investigations suggesting that the optimized adsorption of the HCOO* intermediate on the S-Cu_2O/Cu surface is modified, and S-doping suppresses the H_2 route (surface H), (ii) GBs at the Cu_2O/Cu interfaces reduce the adsorption energy favoured by S-doping and increased formate efficiency by inhibiting the HER route and CO_2-to-CO conversion. In another work, Wang *et al.*[135] fabricated S-doped Cu_2O derived from CuS 811 (consisting of CuS and $CuSO_4 \cdot 3H_2O$) using the electrolysis method to study the relationship between the catalytic activity and GBs. This catalyst performed exceptionally well for formate production in ECO_2R, reaching an optimal FE of 92% in an H-type cell and an excellent $j_{formate}$ of 321 mA cm^{-2} in a flow cell while retaining an FE of more than 80%. The authors explained this outstanding performance from two viewpoints. (1) Structural studies showed that $CuSO_4 \cdot 3H_2O$ inhibits CuS growth and *vice versa*, leading to lower grain sizes and more primary GBs (Fig. 10h–k). After electrolysis and electrochemical reduction, these grains break down into the smaller ones, resulting in more dense grain boundaries suitable for electrocatalysis (Fig. 10l and m). (2) The kinetics of S shedding during electrochemical ECO_2R are comparatively slow because of the initial mixture of multi-crystalline phases; this leads to a higher S content and a relatively complete CuS crystalline phase in CuS 811 post ECO_2R. They did DFT calculations and showed that retaining sulfur–sulfur bonds from covellite may reduce the binding energy, mainly by weakening the binding energies with several reaction intermediates, thus decreasing the energy barriers and facilitating the desorption steps and increasing formate generation activity. The catalytic impact of the GB was comparable to its dislocation strain field, establishing a way for a more comprehensive application of the GB effects in heterogeneous catalysts. More extensive research is required to understand the fundamental principle of GBs and apply it to developing advanced catalytic schemes for the ECO_2R into valuable products.

3.4 Defect/vacancy creation effect for improving electrocatalytic performance

Defect engineering, such as vacancy creation, exposing edge sites, and heteroatom doping, is essential for electrocatalytic activities because defects are usually rich in active sites.[136,137] Furthermore, defects can modulate the electronic properties of active sites, increasing the density of catalytic active sites. As a result, defect engineering has become a strategy mostly used to increase active sites and improve charge transfer ability to fine-tune electrocatalytic activity.[138,139] Therefore, considering the connection between diverse defects and the specific catalytic properties of various materials is critical for developing advanced catalysts.[140,141]

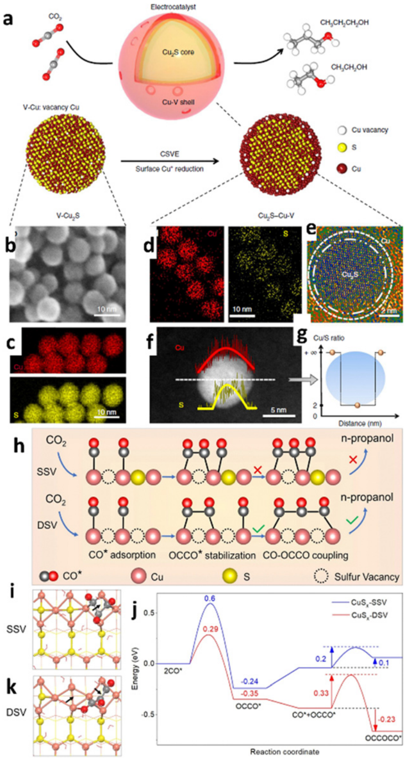

Fig. 11 Catalyst design and structural characterization. (a) Schematic illustration of Cu_2S–Cu–V CSVE electrocatalyst design for production of multi-carbon alcohols by CO_2 reduction. (b) and (c) TEM (b) and EDS (c) mapping of the original V–Cu_2S nanoparticles, showing the uniform size and the homogeneous distribution of Cu and S. (d)–(g) EDS mapping (d), high-resolution TEM (e), EDS line scan (f) and the ratio of Cu/S concentration (g) of the reduced CSVE nanocatalysts after electrochemical reduction, showing the removal of S from the nanoparticle surface. V–Cu indicates Cu with surface vacancies (reproduced with permission from ref. 142, copyright Nature 2018). (h) The mechanism of *n*-propanol formation on adjacent CuS_x-DSV shows the dimerization of CO–CO followed by CO–OCCO coupling. (i) and (k) Top views of the optimized OCCOCO* intermediate configurations on the (100) surface of (i) CuS_x-SSV and (k) CuS_x-DSV. The arrows indicate the positions of sulfur vacancies. (j) The corresponding energy diagrams of CuS_x-SSV (blue curve) and CuS_x-DSV (red curve) at 0 V *vs.* RHE. The pink, yellow, grey, and red spheres and red wireframe in (h)–(k) represent copper, sulfur, carbon, and oxygen atoms and water molecules, respectively (reproduced with permission from ref. 143, copyright Nature 2021).

For example, it is difficult to obtain the *n*-propanol product during electrolysis because of the complicated C_3 creation mechanism that requires the stabilization of $^*C_2$ intermediates and subsequent C_1–C_2 coupling. Zhuang and colleagues[142] synthesized a bifunctional core–shell nanostructure (Fig. 11a) showing that adding sulfur atoms to the catalyst core and copper vacancies to the shell named core–shell vacancy engineered Cu (CSVE-Cu) results in excellent ECO_2R activity towards *n*-propanol formation. The CSVE-Cu electrocatalyst exhibited satisfactory reduction performance by generating highly energy-dense C_{2+} alcohols (*i.e.*, C_3H_7OH and CH_3CH_2OH) with a FE of 32% ± 1%. The alcohol-to-ethylene ratio increased sixfold compared to simple copper nanoparticles, indicating an alternative route for producing alcohols instead of alkenes. According to DFT modelling, the incorporated vacancy, as shown by morphology analysis from Fig. 11b–g, on a bifunctional core–shell catalyst raises the activation energy of the C_2H_4 route (1.148 eV). Still, it does not affect the CH_3CH_2OH path (0.427 eV). Peng *et al.*[143] created a double-sulfur vacancy (DSV) engineering structure to achieve enhanced ECO_2R performance. The mechanistic study showed that the DSV-engineered CuS(100) planes facilitated the stabilization of both CO* and OCCO*, a $^*C_2$ dimer which undergoes the subsequent interaction with a third *CO *via* CO–OCCO coupling (Fig. 11h–k). The DSV-engineered CuS_x exhibited an improved $FE_{n\text{-PrOH}}$ of ∼15.4% $-1.05\ V_{RHE}$ for *n*-propanol formation in 0.1 M $KHCO_3$ medium in a H-cell set up, but in flow cells, $j_{n\text{-PrOH}}$ was increased to 9.9 mA cm^{-2}. This study provides an appealing strategy for using the lithium electrochemical tuning method to create an array of novel frameworks with ion vacancies as active sites for electrochemical reactions.

3.5 Heterostructure effect for improving electrocatalytic performance

A heterostructure commonly comprises more than one component that accomplishes different roles in the electrocatalytic reactions.[144] Modification of physical and chemical properties will enhance each component's combined advantages. As a result, the various components will produce a synergistic effect, contributing to ECO_2R kinetics.[145,146] Unlike single-component catalysts, the synergistic effects caused by heterogeneous interfaces can significantly improve catalytic activity.[147] Inspired by this, recently, Tao *et al.*[148] developed a novel $Cu_2S/SnO_2@C$ nanocomposite by solvothermal heating, where $SnO_2@C$ is confined on the snowflake-like Cu_2S surface and has a combined interfacial effect at the Cu_2S sites (Fig. 12a–e). Specifically, the Cu_2S snowflake improves the CO_2 concentration near the surface, and carbon spheres increase the surface electron transport capacity. Afterwards, the as-synthesized $Cu_2S/SnO_2@C$ nanocomposites are used as a working electrode to investigate ECO_2R to HCOOH. They varied the loading amount to examine the impact of the $SnO_2@C$ content on the ECO_2R. The prepared $Cu_2S/1\%SnO_2@C$ catalyst shows good selectivity and activity for ECO_2R to form liquid HCOOH products, thus outperforming all the existing Cu-based electrocatalysts. The electrochemical study demonstrated a high ECSA, exceptional CO_2 adsorption capacities and a fast electron transport rate on the surface of $Cu_2S/1\%SnO_2@C$. Additionally, DFT calculations revealed the plausible reaction pathways for the enhanced HCOOH production by $Cu_2S/SnO_2@C$. Notably, through heterostructure construction, this work provides an easy method to fabricate effective Cu-based catalysts that can improve HCOOH selectivity and activity in the ECO_2R process.

Another work used a redox process at ambient temperature to create a heterostructure of CuS and S-doped SnO_2 (CuS/SnO_2-S) for ECO_2R, as shown in Scheme 1 in Fig. 13.[149] Structure analysis methods revealed the structural regeneration phase that had occurred during the first electrolysis (Fig. 13a–i). The unique restructuring of the CuS/SnO_2-S heterostructure to $Cu/Sn/Cu_{6.26}Sn_5$ nanowires reduces CO_2 adsorption energy while increasing *H adsorption and reducing the competing HER. During ECO_2R, at -0.8 V_{RHE}, it achieves a formate conversion with a FE of 84.9% and a yield of 8860 μmol h^{-1} cm^{-2} in an H-cell at a $j_{formate}$ of 18.8 mA cm^{-2}. This research focused on the structural development of CuSn sulfides from precursor materials' early state as well as the process of formate production.

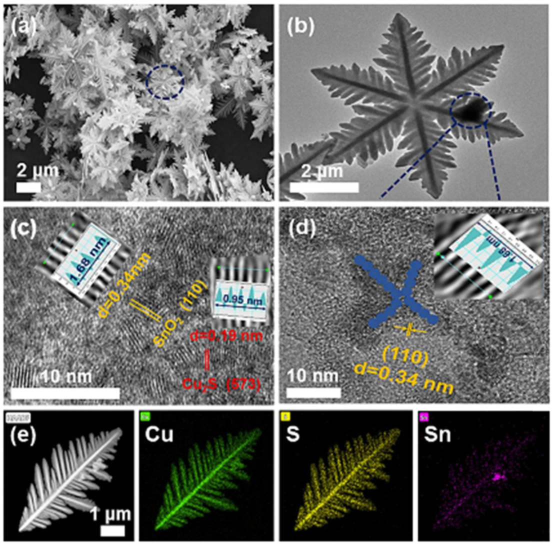

Fig. 12 SEM image (a) and TEM image (b) of $Cu_2S/SnO_2@C$. HRTEM images of $Cu_2S/SnO_2@C$ (c) and $SnO_2@C$ (d). The HAADF-STEM image and the corresponding elemental mapping of $Cu_2S/SnO_2@C$ (e) reveal the distribution of Cu (green), S (yellow), and Sn (rosy), respectively (for interpretation of the references to colour in this figure legend, the reader is referred to the web version of this article; reproduced with permission from ref. 148, copyright Elsevier 2023).

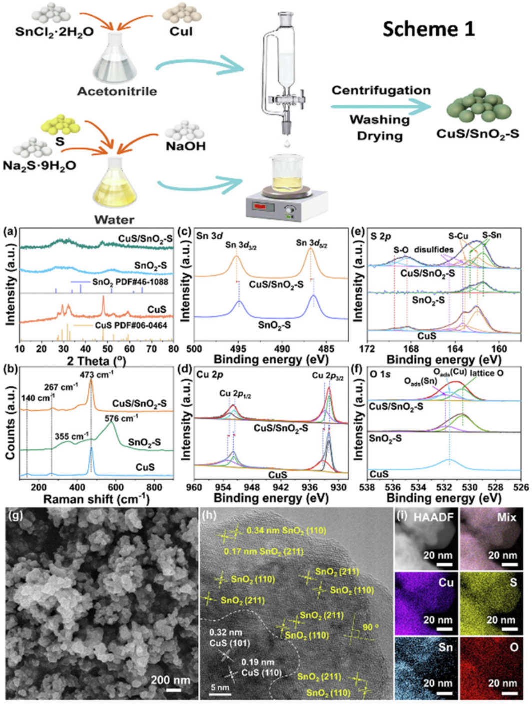

Fig. 13 Scheme 1: the synthetic process of CuS/SnO_2-S. (a) XRD patterns, (b) Raman spectra and (c)–(f) XPS analysis of Sn 3d, Cu 2p, S 2p and O 1s of CuS/SnO_2-S RCu/Sn high, SnO_2-S and CuS. (g) SEM images and (h) HRTEM and (i) HAADF image and EDS mapping of as-prepared CuS/SnO_2-S RCu/Sn high (reproduced with permission from ref. 149, copyright Elsevier 2023).

Wang *et al.*[150] created an innovative framework of 0D/2D composites of SnO_2 nanoparticles dispersed on CuS nanosheets (SnO_2/CuS) for selective syngas generation (a CO/H_2 ratio of 0.11–3.86), as illustrated in Scheme 1 in Fig. 14. The electrocatalytic system was highly efficient for syngas selectivity, with a faradaic efficiency of nearly 85%, a turnover frequency (TOF) of 96.12 h^{-1}, and stability of 24 hours. They explained the increased catalytic activity based on two factors: (a) the most active sites are provided by the uniformly distributed ultrasmall SnO_2 nanoparticles on ultrathin CuS nanosheets, enabling a faster electron transfer rate (Fig. 14a–c) and (b) the interfaces between SnO_2 and CuS lower the activation energy of reaction intermediates, enhancing ECO_2R performance to generate high-ratio tunable syngas. Both the SnO_2(110) and CuS(001) facet surfaces, as shown in Fig. 14d and e, favoured HCOOH creation. In contrast, the SnO_2/CuS contact considerably lowered the free energy of COOH* intermediate synthesis by 0.52 eV and encouraged CO formation.

In 2023, Liu and group[151] reported the production of monoclinic-phase colloidal Cu_2SnS_3 nanoplates with precise

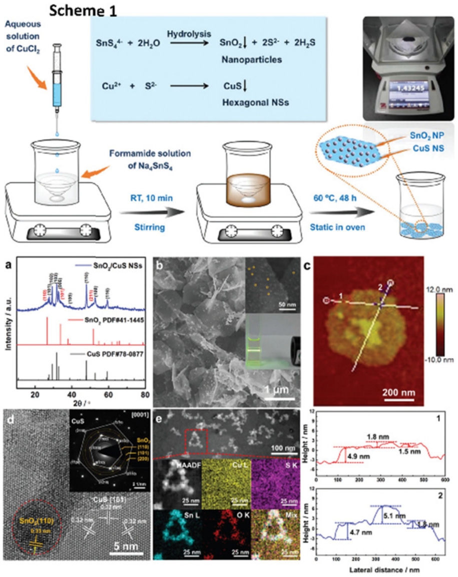

Fig. 14 Scheme 1: schematic illustration and the proposed reaction mechanism for the one-pot scalable synthesis of hierarchical SnO_2/CuS NSs. Structural characterization of SnO_2/CuS NSs. (a) XRD patterns. (b) SEM and (inset) magnified SEM image of the surface and photograph of the dispersion of SnO_2/CuS NSs in EtOH, demonstrating the Tyndall effect with a laser pointer. (c) AFM image and the corresponding height profiles of the as-obtained ultrathin SnO_2/CuS NSs marked by lines in different colours. (d) HRTEM image and the corresponding SAED pattern (inset). (e) HAADF-STEM images and the corresponding elemental mapping images of SnO_2/CuS NSs (reproduced with permission from ref. 150, copyright RSC 2020).

surfaces (Fig. 15a–h). Their findings revealed that thiocyanate-capped plate-shaped Cu_2SnS_3 nanoparticles exhibit outstanding formate selectivity over a broad spectrum of potentials, observing a formate production with a FE_{max} of 92% with a $j_{formate}$ as high as 181 mA cm^{-2} in a GDA-based flow cell. Compared to prior studies of mono metal- and bimetal-based Cu– and Sn–sulfide nanoparticles that typically experienced phase separation or the creation of metal-based domains, Cu_2SnS_3 demonstrated outstanding structural robustness, as demonstrated by the concurrent retention of nanoplate morphology and the crystal phase during ECO_2R. *In situ* and DFT studies, as shown in Fig. 15i–m, have demonstrated that the Sn site basal-planes are the multi-active sites for favourable HCOO* adsorption to produce formate by ECO_2R. According to DFT studies, thiocyanates also inhibit Cu sites on the surface, and the Sn site's electronic structure modulation is observed, favouring the activation energy barrier of ECO_2R to formate.

Also, Xiong *et al.*[152] used a homogenous mixing approach to create bimetallic $CuInS_2$ hollow nanoparticles. According to their observations, the synergy between metal centres and hollow-shaped nanostructures accelerates the electron transfer kinetics. Consequently, the bimetallic catalyst had a FE_{CO} of 82.3% at −1.0 V_{RHE} and a FE_{HCOOH} of 72.8% at −0.7 V_{RHE}. *In situ* studies showed faster conversion of CO_2 to $CO_2^{\bullet-}$ radicals as the rate-limiting step, and afterwards, electron redistribution happened at different potentials, leading to a product distribution shift (CO to HCOOH). Furthermore, Nyquist plots showed that hollow-like $CuInS_2$ nanocomposites have a substantially greater interfacial charge-transfer rate during electrocatalysis than Cu_2In because the interfacial charge-transfer impedance (R_{ct}) of Cu_2In is lower than that of $CuInS_2$.

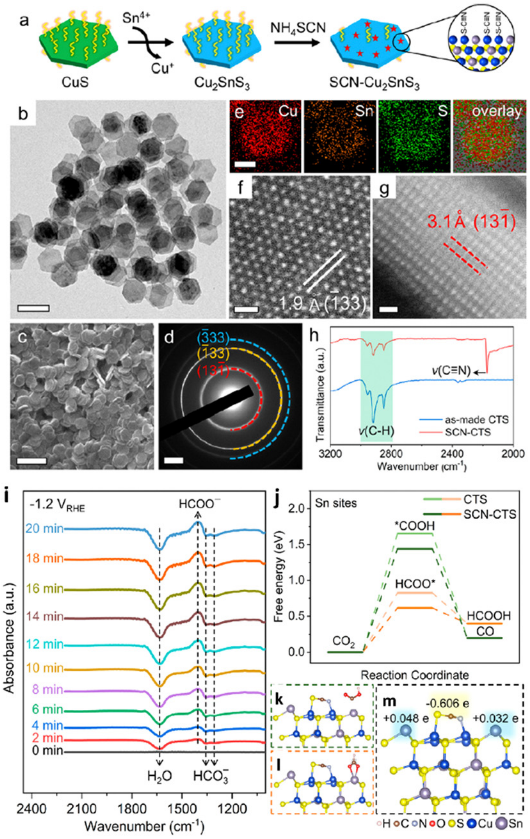

Fig. 15 Synthesis and characterization of Cu_2SnS_3 nanoplates. (a) Synthetic scheme of Cu_2SnS_3 nanoplates and ligand exchange with NH_4SCN. (b) TEM and (c) SEM images, (d) SAED pattern, (e) STEM-EDS elemental maps, (f) top-view and (g) side-view ACSTEM images of Cu_2SnS_3 nanoplates. (h) FTIR spectra of Cu_2SnS_3 nanoplates (basal plane edge length: 41.2 ± 2.4 nm) before and after ligand exchange with NH_4SCN. Scale bars: (b) 100 nm, (c) 200 nm, (d) 2 nm^{-1}, (e) 30 nm, (f) and (g) 0.5 nm. (i) *In situ* FTIR spectra recorded at different times for CTS-3 at −1.2 V *vs.* RHE. (j) Free energy diagrams of ECO_2R into formate and CO on Cu_2SnS_3 nanoplates. (k)–(m) Optimized geometric structures of *COOH (j), HCOO* (k), and SCN-modified Cu_2SnS_3 (001) surface (m). Also shown in (m) are charge transfers obtained using Bader charge analysis where *e* is the elementary charge (reproduced with permission from ref. 151, copyright ACS 2023).

Graphdiyne (GDY) is a novel 2D all-carbon structure where alkyne bonds (sp-hybridized C) bind each benzene ring (sp^2-hybridized C). GDY's particular sp-/sp^2-hybridized architecture provides numerous distinctive and intriguing qualities that are exceptional to standard carbon materials, *i.e.*, abundant carbon chemical bonds, massive conjugated pi structures, a favourable band gap, *etc.*[153] More enticingly, the exceptionally variable distribution of surface charges and incomplete charge transfer between GDY and metal centres can offer more active sites, higher intrinsic activity, and efficient control of reaction intermediates' adsorption and desorption behaviour on functional site surfaces.[153] Owing to these advantages, in 2023, Li and colleagues[153] discovered a novel graphdiyne/copper sulfide (GDY/CuS$_x$) heterostructured electrocatalyst (Fig. 16a) controlling *in situ* development of GDY over the surface of CuS$_x$, as illustrated in Fig. 16b–x. The authors showed that the imperfect charge transfer between GDY and atomic Cu increased catalytic conductivity, providing additional active sites and enhancing the conversion performance. Thus, the heterostructure accomplished an FE of 70% and a j_{total} of 65.6 mA cm^{-2} at −0.9 V$_{\text{RHE}}$ for ECO$_2$R to formic acid.

Heterostructure engineering modulates interfacial charge distribution and promotes CO$_2$ adsorption. Wen *et al.*[154] used a local sulfur doping strategy (SHKUST-1) to appropriately develop an isolated Cu@S motif on the HKUST-1 pre-catalyst (Fig. 17a). The *in situ* reconstruction of S-HKUST-1 results in a Cu(S) array and active biphased copper/copper sulfide (Cu/Cu$_x$S$_y$) interfaces (Fig. 17b), achieving highly selective ethylene (C$_2$H$_4$) formation in the H-cell with a FE$_{\text{max}}$ of 60.0%. In a flow cell configuration, ECO$_2$R occurred at a high current density of 400 mA cm^{-2} with a FE$_{\text{C}_2\text{H}_4}$ of approximately 57% and FE$_{\text{C}_2}$ (FE of C$_2$H$_4$, C$_2$H$_5$OH and CH$_3$COOH) of 88.4%. The S motif is stable before and after the ECO$_2$R, as evidenced by the systematic characterization (Fig. 17c–h). The researchers explain S-HKUST-1's superior selectivity as follows: the approximate distance between Cu^0 and Cu$^{\delta+}$ favours the *CO dimerization step at the interface of Cu/Cu$_2$S. Also, a high S-concentrate electrocatalyst (*i.e.*, Cu$_2$S) showed a significant Cu–Cu distance that practically restricted *CO dimerization. Compared to a pure metallic Cu catalyst, the Cu/Cu$_2$S interface decreased to *CO species binding energy at the surface and fastened *CO dimerization (Fig. 17i–m). Similarly, in 2023, Yu *et al.*[155] constructed a Cu$_2$S nanocrystal on Cu nanosheets (Cu–Cu$_2$S), as shown in Fig. 18a, for ECO$_2$R to C$_2$H$_5$OH. The author's design focuses on attaining three discrete features: (i) the nanocomposites produce a positive charge locally on Cu (Cu$^{\delta}$+) to offer multi-active sites during ECO$_2$R; (ii) the evenly dispersed tiny Cu$_2$S on Cu generate interfaces, as illustrated in Fig. 18b–g, between Cu$^{\delta}$+ and Cu in the zero-valence state Cu^0; and (iii) the uneven and stepped Cu–Cu$_2$S surface offers a spatially advantageous arrangement for C$_2$H$_5$OH production. Due to these structural features, a total FE of 90% for C$_{2+}$ products (a FE of 6% for C$_2$H$_5$OH and a FE of 15% for C$_2$H$_4$) with a partial current density of 45 mA cm^{-2} at −1.2 V$_{\text{RHE}}$ was attained in a H-cell configuration. According to the *in situ* spectroscopy and DFT investigations, as illustrated in Fig. 18h–l, they showed that the three characteristics of Cu–Cu$_2$S work together to (1) improve CO$_2$ adsorption by enabling high electronic conductivity, (2) facilitate the adsorption of the *CO intermediate on the Cu–Cu$_2$S surface, (3) lower the energy barrier for forming the *COCO intermediate, and (4) make the reaction path more thermodynamically viable for C$_2$H$_5$OH over C$_2$H$_4$. This study emphasizes the potential for commercializing alcohol and related product formation from CO$_2$ by proposing an effective method and the underlying mechanism for the significant increase of ECO$_2$R to C$_2$H$_5$OH conversion.

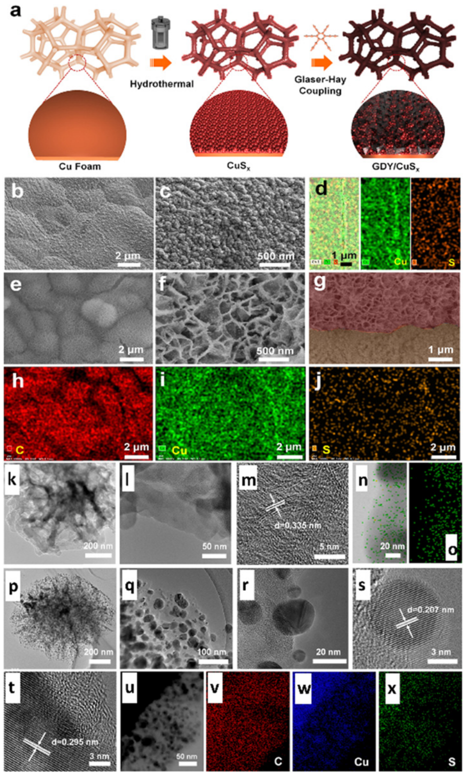

Fig. 16 (a) Schematic representation of the synthesis route of GDY/CuS$_x$; and (b) low- and (c) high-magnification SEM images of CuS$_x$. (d) Energy dispersive spectroscopy mapping of CuS$_x$. (e) Low- and (f) high-magnification SEM images of GDY/CuS$_x$. (g) Cross-sectional SEM image of GDY/CuS$_x$; and (h)–(j) energy dispersive spectroscopy mapping of GDY/CuS$_x$. (k) TEM and (l) and (m) HRTEM images of the GDY nanosheet. (n) STEM image (left) and (o) the corresponding elemental mapping (right) of the elemental carbon of GDY. (p)–(r) TEM and (s) and (t) HRTEM images of GDY/CuS$_x$, (u) STEM image and the corresponding elemental mapping of (v) C, (w) Cu, and (x) S elements of the GDY/CuS$_x$ electrode (reproduced with permission from ref. 153, copyright RSC 2023).

Mosali *et al.*[156] developed an array of Cu$_x$Zn$_y$S nanoparticles (Fig. 19a–l) with varying Cu:Zn compositions and that are electrochemically stabilized, resulting in SD-Cu$_x$Zn$_y$S catalysts. The catalysts showed composition-dependent product selectivity during ECO$_2$R. Operating in an H-cell configuration, it was discovered that SD-Cu$_x$Zn$_y$S catalysts with a higher copper content exhibited a significantly higher FE$_{\text{CH}_4}$ than the Zn-rich catalysts. In contrast, Zn-rich counterparts produced CO as the primary ECO$_2$R product. The best composition of 1 : 1 Cu : Zn resulted in highly selective CH$_4$ as the main product, with an FE of 76 ± 3% at −0.98 V$_{\text{RHE}}$. The current density increased after switching to a flow cell arrangement for ECO$_2$R in 1.0 M KHCO$_3$ or 1.0 M KOH electrolyte. However, the selectivity changed to produce syngas, with molar ratios of 2 : 3 to 3 : 2 for the formation of H$_2$/CO. This tendency holds irrespective of the applied potential, particularly in the 1.0 M KOH electrolyte. An *ex situ* investigation revealed a significant reduction in CuS in electrocatalysts with higher copper content. In addition, pre-reduction of CuZnS catalysts and time-dependent observations showed the importance of copper's higher oxidation state and the interaction of partially reduced

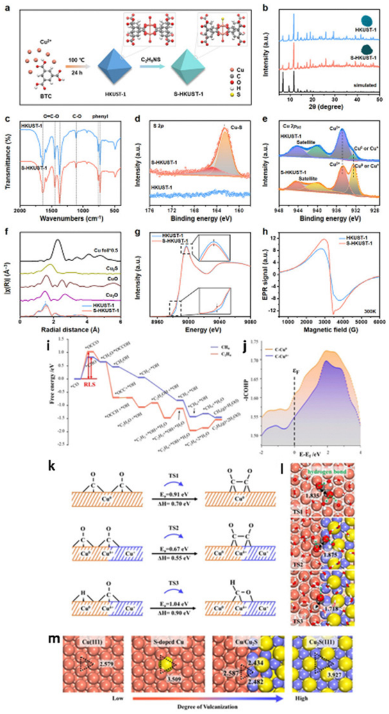

Fig. 17 (a) Schematic diagram of the preparation of S-HKUST-1. (b) XRD patterns of the prepared S-HKUST-1 and HKUST-1 precatalysts are well indexed to the simulated HKUST-1. The insets are digital photos of S-HKUST-1 (dark green) and HKUST-1 (blue). (c) FTIR spectra of S-HKUST-1 and HKUST-1 precatalysts indicate negligible differences. The XRD and FTIR results prove that the long-range ordered structure is not destroyed after S incorporation. (d) and (e) High-resolution XPS spectra of S-HKUST-1 and HKUST-1 precatalysts in the (d) S 2p region, showing the characteristic Cu@S bonds in the S-HKUST-1 precatalyst and (e) Cu 2p region, showing the increased content of $Cu^{\delta+}$ or Cu^0 species. (f) FT of the EXAFS spectra and (g) Cu K-edge XANES spectra of HKUST-1 and S-HKUST-1 precatalysts. The inset in (g) is the magnified image. The XAFS results in (f) and (g) prove the successful incorporation of local heteroatoms, which might be bonded to Cu atoms in MOFs. (h) EPR spectra of the samples measured at 300 K. (i) Calculated free energy profiles for ECO_2R to CH_4 and C_2H_4 over a pure Cu(111) surface, indicating that the initial *CO hydrogenation and dimerization steps determine the CH_4 and C_2H_4 product distribution. (j) Integrated crystal orbital Hamilton population (−ICOHP) curves of Cu $Cu^{\delta+}$–CO and Cu^0–CO bonds. (k) The reaction barriers together with enthalpies and (l) the corresponding transition state configurations for *CO dimerization and hydrogenation over Cu(111) and Cu/Cu_2S surfaces, respectively. Yellow, red, grey, white, orange and blue balls refer to S, O, C, H, Cu^0 and $Cu^{\delta+}$ atoms, respectively. (m) Surface configuration (top view) of Cu-based structures with different degrees of vulcanization. The distances between two neighbouring Cu atoms on different surfaces are given in b (reproduced with permission from ref. 154, copyright Wiley-VCH GmbH 2021).

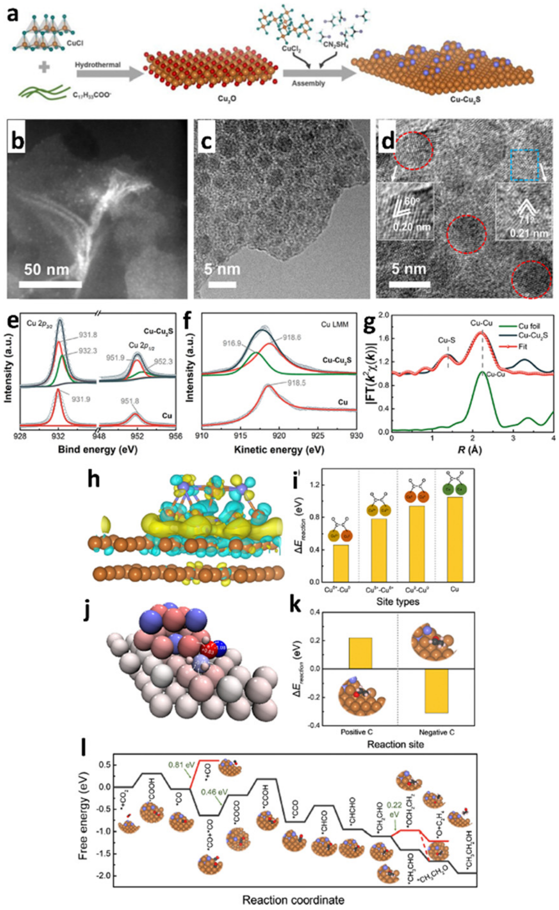

Fig. 18 (a) Schematic illustration of the synthesis of Cu–Cu_2S. Characterization of the Cu–Cu_2S sample. (b) and (c) TEM, (d) high-resolution TEM (HRTEM), (e) high-resolution Cu 2p XP spectra, (f) Cu LMM Auger spectra, and (g) Cu K-edge K_2-weighted $\chi(k)$ function of Fourier transform extended X-ray absorption fine structure (EXAFS) spectra of the sample, where pristine Cu and Cu foil are used as controls in panels (e)–(g), revealing that both Cu(0) and Cu(I) states are involved, respectively. Calculated ECO_2R on Cu–Cu_2S. (h) DFT-calculated charge density difference of Cu–Cu_2S (the Cu and S atoms are in brown and violet, respectively; the yellow and cyan colours represent charge accumulation and depletion, respectively; the isosurface value is 0.002 e $Å^{-3}$). (i) Energy barrier ($\Delta E_{reaction}$) for two *CO forming one *OCCO *via* C–C coupling at $Cu^{\delta+}$–Cu^0, $Cu^{\delta+}$–$Cu^{\delta+}$, and Cu^0–Cu^0 sites of Cu–Cu_2S and at the pristine Cu surface, where $Cu^{\delta+}$ and Cu^0 of Cu–Cu_2S and Cu of pristine are in brown, red, and green, respectively, showing that the energy barrier at the $Cu^{\delta+}$–Cu^0 site of Cu–Cu_2S is the lowest. (j) Bader charge of *CH_2CHO adsorbed on Cu–Cu_2S, where the colour ranging from blue to red indicates the negative to the positive charge of the atoms, respectively. (k) $\Delta E_{reaction}$ for hydrogenation on the positively charged C and negatively charged C of *CH_2CHO converting to CH_2CH_2O* and CH_3CHO*, respectively. (l) Calculated free energy for each step of the reaction pathway converting CO_2 to C_2H_5OH on Cu–Cu_2S (reproduced with permission from ref. 155, copyright ACS 2023).

CuS and ZnS present in the catalysts in attaining methane selectivity. These findings demonstrate that copper's oxidation state is crucial in determining selective product formation using copper-based catalysts. Likewise, the same research group created S-derived copper–cadmium (SD-Cu_xCd_y) electrocatalysts earlier, where x and y denote the molar ratio of Cu/Cd to assist in generating vital intermediates.[157] In 0.1 M $KHCO_3$ solution, the $SDCuCd_2$ catalyst observed 32% ethanol selectivity at a low overpotential of −0.89 V_{RHE}. They exhibited selective ethanol production at lower overpotentials with the best-performing SD-$CuCd_2$ electrocatalyst of Cu_3Cd_{10}alloy/Cu_2S/CdS phased composites, as illustrated in Fig. 19m and n.

Xi and colleagues[158] recently developed and built CeO_2/CuS (Fig. 20a–k) with a −0.5 V_{RHE} overpotential for ECO_2R to ethanol and a $FE_{C_{2+}}$ of 75% at −0.8 V_{RHE}. During ECO_2R, they investigated catalysts' structural development, interactions, and activity sources, as illustrated in transmission electron

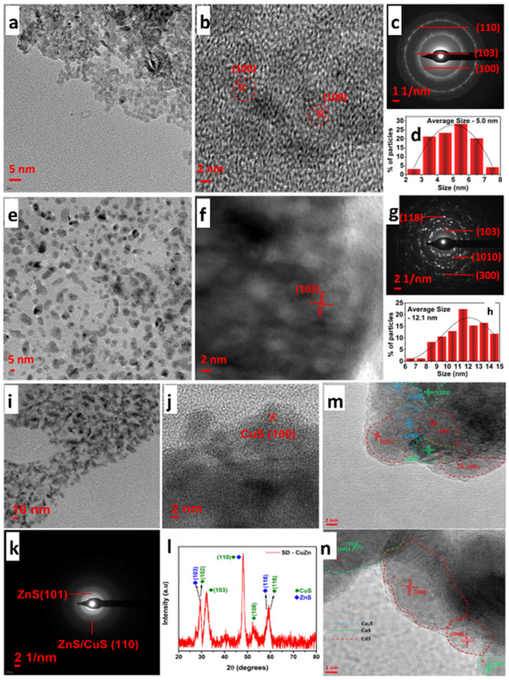

Fig. 19 (a) and (e) TEM images, (b) and (f) HR-TEM images, (c) and (g) SAED pattern and (d) and (h) particle size distribution of (a)–(d) CuS and (e)–(h) ZnS nanoparticles. (i) TEM images, (j) HR-TEM images, (k) SAED pattern, and (l) XRD powder pattern of SD-CuZn nanoparticles obtained upon pre-reduction at −0.80 V *vs.* RHE in 0.10 M $KHCO_3$ solution saturated with CO_2 (blue diamonds (♦) represent the peaks corresponding to ZnS, and green circles (●) represent the peaks corresponding to CuS; reproduced with permission from ref. 156, copyright Elsevier 2024). HR-TEM images of (m) $CuCd_2S$; (n) Cu_2CdS showing boundary distributions of CdS, CuS and Cu_2S (reproduced with permission from ref. 157, copyright Wiley-VCH GmbH 2023).

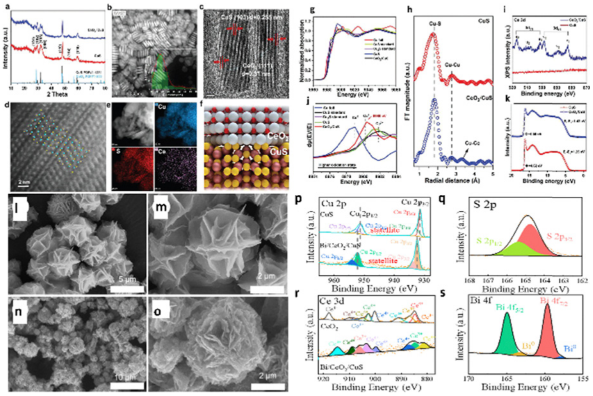

Fig. 20 Crystal structures and composition of CuS and CeO_2/CuS. (a) XRD patterns of CuS and CeO_2/CuS. (b) TEM image of CeO_2/CuS (inset: size distribution). (c) HRTEM image of CeO_2/CuS. (d) The HAADF-STEM image of CeO_2/CuS (inset: CuS 9 000 523. cif). (e) The HAADF-STEM image and corresponding EDS element mapping of CeO_2/CuS. (f) Structural representation of CeO_2/CuS, white: Ce atoms; red: O atoms; yellow: S atoms; gold: Cu atoms. Electronic structures of CuS and CeO_2/CuS. (g)–(i) X-ray absorption spectra of CeO_2/CuS, CuS catalyst, standard CuS, standard Cu_2S, and Cu foil. (g) Normalized Cu K-edge XANES. (h) the first derivative $\mu(E)/dE$. (i) Fourier-transformed $k^2\chi(k)$ of CeO_2/CuS (lower panel) and CuS (upper panel). (j) Ce 3d XPS spectra. (k) UPS spectra (reproduced with permission from ref. 158, copyright Wiley-VCH GmbH 2023). SEM images of (l) and (m) CuS and (n) and (o) Bi/CeO_2/CuS. XPS patterns of Bi/CeO_2/CuS: (p) Cu 2p, (q) S 2p, (r) Ce 3d, and (s) Bi 4f (reproduced with permission from ref. 159, copyright MDPI 2024).

microscopy (TEM) and high-resolution transmission electron microscopy (HRTEM) images (Fig. 20b–d). The fast electron movement route provided by CeO_2 regions in catalysts prevents electron aggregation around Cu^+ sites, preserving Cu^+ sites during ECO_2R. The experimental *in situ* studies and DFT calculations reveal that altering CeO_2 on CuS thermodynamically reduces the production energy for *COCHO compared to CuS nanoplates. The fast water molecule activation near CeO_2 speeds up the synthesis of *COCHO. As a result, the C–C coupling is accelerated *via* the *CHO route, providing CeO_2/CuS catalysts with exceptional electrocatalytic efficacy towards C_{2+} products. Wang *et al.*[159] proved that heterointerfaces of Bi/CeO_2/CuS nanohybrids (Fig. 20l–s) can be advantageously employed as a highly efficient and selective catalyst for ECO_2R to produce formate over a wide potential range. The nanohybrid demonstrated excellent activity at −0.9 V_{RHE}, with a formate efficiency of 88% and a current density of −17 mA cm^{-2}. The morphological analysis showed no change in the structure after a one-hour reaction at −0.9 V_{RHE}, and the FE of formate remained stable at that potential. The Bi/CeO_2/CuS heterostructure substantially decreases the formation energy barrier of OCHO* intermediates because, during electrolysis, Ce^{4+} rapidly suffers Ce^{3+} reduction, forming a conductive network of Ce^{4+}/Ce^{3+}, resulting in high activity and selectivity of ECO_2R to formate. Overall, the system increased electron mobilization, stabilized Cu^+ species, and improved CO_2 adsorption and activation over the catalytic surface. Furthermore, sulfur boosts the transformation of OCHO* to formate.

Han *et al.*[160] employed a simple solution-phase method to synthesize a ternary metal–metal sulfide Bi–Cu_2S heterostructure electrocatalyst (Fig. 21a and b). Due to the high synergistic and interfacial effects between Bi and Cu_2S, the heterostructure showed a lower overpotential (240 mV) than Bi with an outstanding $FE_{formate}$ of >98% and 2.4 and 5.2 times higher partial current density than bare Cu_2S and Bi at −1.0 V_{RHE}. According to the theoretical study, the HCOOH generation was aided by stabilizing the *OCHO intermediates over *COOH and *H due to the higher electron transfer rate between the Bi and Cu_2S interfaces (Fig. 21c–i).

Prasanna *et al.*[161] designed a rationally created novel heterostructure of CuS decorated NH^{4+} ion incorporated stable 1T-WS_2/WO_3 using a simple hydrothermal method followed by a reflux technique (Fig. 22a). The nanohybrid favoured reaction mechanism through the *OCHO route, which reduces (by obtaining $H^+ + e^-$) to $HCOO^-$ ($HCOO^-$ pathway) as the main product. Thus, CuS@1T-N-WS_2/WO_3 nanohybrids yielded 55.6% ± 0.5 at −1.3 V_{RHE} and a j_{geo} of −125.05 mA cm^{-2}. Interestingly, from their analysis, the intercalation of NH^{4+} ions with effective surfaces that donate WO_3 and accept protons from WS_2 stabilized the metallic 1T phase. Besides, an effective hydrogen spillover mechanism in the stable heterointerface of 1T-N-WS_2/WO_3 may provide kinetic support for CuS active

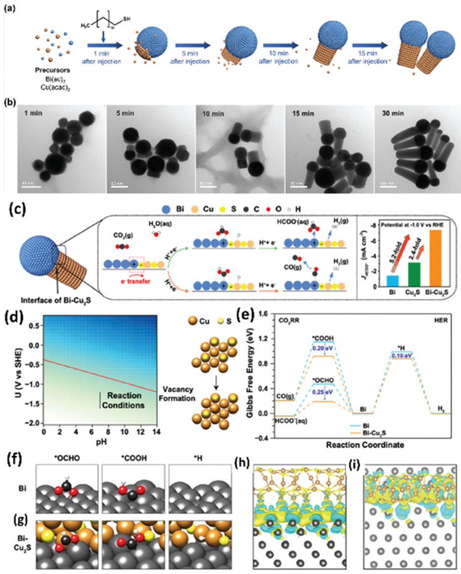

Fig. 21 (a) Schematic illustration of the nucleation and growth of the heterostructured Bi–Cu_2S nanocrystals. (b) TEM images of Bi–Cu_2S at different time intervals after introducing 1-dodecanethiol at 220 1C. (c) Proposed CO_2 reduction mechanism on the Bi–Cu_2S interfacial system. (d) Pourbaix diagram showing the sulfur vacancy formation. (e) Free energy diagrams of the ECO_2R and HER on Bi(001) and Bi–Cu_2S model systems. Optimized geometry structures of key intermediates (*OCHO, *COOH, and *H) on Bi(001) and Bi–Cu_2S systems are shown in (f) and (g), respectively (dark grey, brown, yellow, black, red, and white spheres denote Bi, Cu, S, C, O, and H atoms, respectively). (h) and (i) are the top and front views of the charge density difference for the Bi–Cu_2S interfacial surface, respectively. Cyan corresponds to an isosurface of -0.001 e Bohr^{-3} and yellow corresponds to an isosurface of $+0.001$ e Bohr^{-3} (reproduced with permission from ref. 160, copyright RSC 2022).

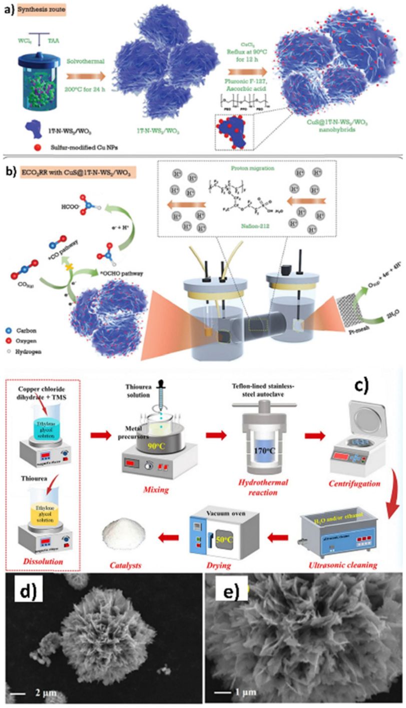

Fig. 22 (a) Schematic illustration of the synthetic process of 1T-N-WS_2/WO_3 and CuS@1T-N-WS_2/WO_3 nanohybrids using a simple solvothermal process and reflux method. (b) Proposed schematic illustration of the ECO_2R in an H-type cell (reproduced with permission from ref. 161, copyright Wiley-VCH GmbH 2023). (c) Schematic diagram of the synthesis procedures and formation of the pristine CuS and TMS-decorated CuS microflower-like structures; SEM images of the MoS_2–CuS catalysts (d) at a low magnification and (e) at a high magnification (reproduced with permission from ref. 162, copyright Springer Nature 2024).

centres, leading to notable improvements in product efficiency and selectivity (Fig. 22b).

Guo *et al.*[162] synthesized transition metal sulfide (TMS)-supported CuS catalysts with microflower-shaped frameworks *via* a facile hydrothermal approach for ECO_2R to CO (Fig. 22c). They investigated the effect of doping TMSs (*i.e.*, ZnS, Bi_2S_3, and MoS_2) with CuS on ECO_2R performance. All the heterostructured catalysts, *i.e.*, ZnS–CuS, Bi_2S_3–CuS and MoS_2–CuS, exhibited flower-shaped morphology, with the doped TMSs (*i.e.*, ZnS, Bi_2S_3, and MoS_2) attached as microcrystals on the surface of petals. On the other hand, strong Cd^{2+} and Cu^{2+} interactions with S^{2-} caused CdS and CuS to aggregate and expand disorderly, forming incomplete sphere-like cage-shaped microstructures. Electrochemical experiments revealed that TMS-supported CuS catalysts outperformed pristine CuS in terms of ECO_2R activity, but their CO_2 conversion rate was reduced. Decorating CuS with MoS_2 resulted in a flower-shaped nanomorphology (Fig. 22d and e), enhancing the catalyst's CO selectivity from 72.67% to 83.20% at -0.6 V_{RHE}. With the increase in applied potential from -0.2 to -1.0 V_{RHE}, CO selectivity initially improved and then decreased, but the CO_2 conversion rate increased considerably from 0.2% to 21.9%. It has been observed that, during a 300-minute electrolysis at -0.6 V_{RHE}, the target MoS_2–CuS catalyst exhibited constant ECO_2R activity, with CO selectivity being improved over a limited range of 73.6–88.5% and j_{CO} remaining stable at about 3.6 mA cm^{-2}. The authors attributed the increased selective CO formation linked to the synergistic effect of the generated GBs, undercoordinated S-vacancies, and edge-exposed Mo sites in boosting CO_2 activation, stabilizing *COOH adsorption, facilitating *CO desorption, and reducing the energy barrier of the potential-limiting step.

3.6 Heteroatom doping effect for improving electrocatalytic performance

Doping is widely regarded as an effective method for modulating the electronic structure of a catalyst through charge redistribution.[163,164] Doping different elements into the lattice of the pristine material can effectively modulate the electronic and physiochemical properties to fine-tune its electrocatalytic activity.[165,166] Also, heteroatom doping has little impact on crystal structure disruption, so the catalyst's main composition remains unchanged. It has been observed that the doping approach can increase the adsorption/desorption energy of the reaction intermediates.[167,168] The doping strategies are divided into metal and nonmetal doping, as described below.

3.6.1 Metal doping. Metal doping can efficiently catalyze the C–C coupling during ECO_2R. Very recently, Hu *et al.*[169] constructed Mo^{4+}-doped CuS nanosheet-assembled hollow spheres for ECO$_2$R to ethanol in a flow cell configuration. They revealed that doping with Mo^{4+} ions makes the movement of the electrons faster from Cu to S, optimizing the surrounding electrical conductivity and broadening the CuS binding sites, resulting in increased coverage of linear $^*CO_L$ on the Cu site away from the Mo site, producing bridge $^*CO_B$ on the Cu site near the Mo site and activating asymmetric C–C coupling of $^*CO_L$–$^*CO_H$ for ethanol generation. Additionally, the highly electron-dense Cu site away from the Mo site favours the cleavage of Cu–O, promoting the hydrogenation of $CH_3CH_2O^*$ to ethanol. Moreover, the nanosheet-assembled hollow sphere structure and hydrophobic Mo^{4+}-doped CuS were prepared by a GDE assisted flow-cell procedure. The best Mo$_{9.0\%}$–CuS achieved an ethanol FE of 67.5% and a j_{ethanol} of 186.5 mA cm^{-2} at -0.6 V$_{\text{RHE}}$ in a flow cell, with good stability over 26 h of continuous operation. In this work, high valence transition metal ions are doped into Cu-based sulfides to modify the coverage and configuration of related intermediates for ethanol production in a flow cell, thereby developing Cu-based materials for catalyzing ECO$_2$R to ethanol. In another work, a Cu-doped Bi (CDB) nanosheet was created by reconstructing a CuS–Bi$_2$S$_3$ heterojunction precursor *in situ* (Fig. 23a).[170] The *in situ* restructuring of the as-synthesized CuS–Bi$_2$S$_3$ heterojunction precursor, as shown in Fig. 23b–g, resulted in an enhanced CDB catalyst with an industrially acceptable ampere-level current density and remarkable stability for the formate production (Fig. 23h–m). The CDB surface with a high concentration of electrons resulting from an increase in the Fermi level not only helped to stabilize the *OCHO intermediate but also successfully lowered the rate-determining step's reaction kinetic barrier, leading to the exceptional electrocatalytic activity of the CDB catalyst. At the same time, the more excellent selectivity to formate can be due to the reduced ΔG_{OCHO^*} on the CDB surface relative to ΔG_{COOH^*} and ΔG_{H^*}. Furthermore, the effective antioxidation capability of the CDB electrocatalyst allows it to exhibit outstanding stability beyond 100 hours at a high current density of 400 mA cm^{-2} in MEA cells (Fig. 22n).

3.6.2 Nonmetal doping. Many studies have also focused on using nonmetal doping to tune the electronic structure of the electrocatalysts. Nonmetals such as N and S have significantly increased ECO$_2$R catalytic activity. For example, Liang *et al.*[171] conducted theoretical and experimental studies to investigate catalytic reactivity effects on N-doped Cu sulfides using the generalized morphology engineering principle of asymmetric metal pair sites, which promotes C–C coupling on electrode surfaces. First, a computational N-doped Cu$_2$S model layer featured electronically asymmetric Cu$^{\delta1+}$–Cu$^{\delta2+}$ $(0 < \delta_1{}^+ < \delta_2{}^+ < 1)$ metal pairs evidenced by considering their non-uniform charge distribution. The asymmetric electronic structure led to distinct CO adsorption energies and the associated self-adjusting structures, which significantly lowered C–C coupling energy barriers. Later, they experimentally validated the computational hypotheses using XPS of Cu–N moieties within N-doped Cu$_2$S layers. *In situ* FTIR spectroscopy confirmed linear *CO and *CO–CO adsorption configurations from the ≈2080 and 1920 cm^{-1} broad peaks, respectively. After N-doping, the catalytic C$_2$ faradaic efficiency can significantly be elevated to 14.72% due to the promotion of C–C coupling (Fig. 24a).

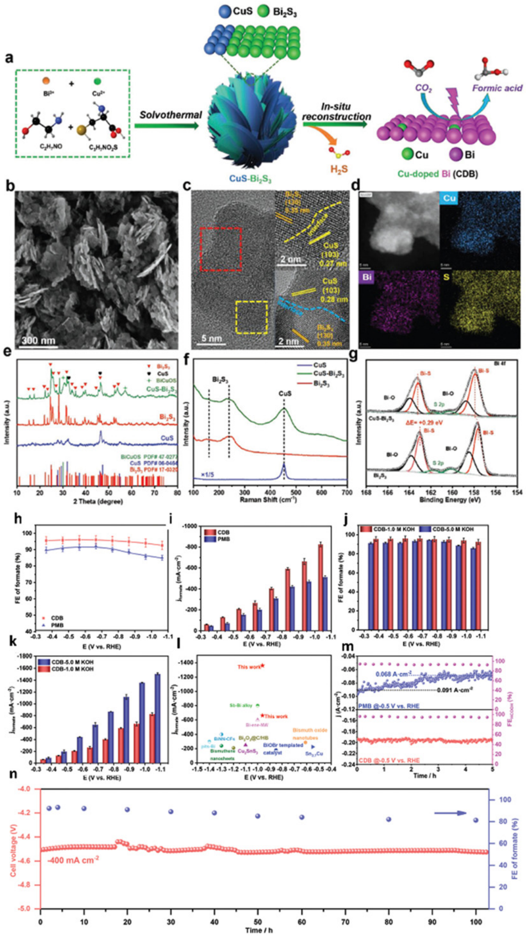

Fig. 23 (a) Synthetic strategy of a CuS–Bi$_2$S$_3$ nano-heterojunction precursor. (b) SEM images of a CuS–Bi$_2$S$_3$ nano-heterojunction precursor. (c) HR-TEM images of a CuS–Bi$_2$S$_3$ nano-heterojunction precursor. (d) Corresponding elemental mapping images of S, Cu, and Bi elements. (e) X-ray diffraction (XRD) patterns of CuS, Bi$_2$S$_3$, and CuS–Bi$_2$S$_3$. (f) Raman spectrum of CuS, Bi$_2$S$_3$, and CuS–Bi$_2$S$_3$. (g) The high-resolution XPS spectra of Bi 4f for Bi$_2$S$_3$ and CuS–Bi$_2$S$_3$. ECO$_2$R measurements in the lab-made flow cell. (h) FE of formate and (i) formate partial current densities at different electrolytic potentials in 1 M KOH electrolyte with CDB and PMB electrocatalysts. (j) FE of formate and (k) formate partial current densities of the CDB electrocatalyst at different electrolytic potentials in 1 M and 5 M KOH electrolytes. (l) Performance comparison of the CDB electrocatalyst with the reported electrocatalysts towards ECO$_2$R to formate in the flow cell. (m) Stability test of PMB and CDB electrocatalysts at the potential of -0.5 V$_{\text{RHE}}$ for 5 h. (n) Continuous 100 h electrolysis in a 5 cm^2 MEA electrolyzer under a constant total current density of -400 mA cm^{-2}. The error bars in (f)–(h) represented the standard deviations of three independent measurements (reproduced with permission from ref. 170, copyright Wiley-VCH GmbH 2022).

In another work, Li *et al.*[172] demonstrated the effective modulation of ECO$_2$R pathways by designing and synthesizing three kinds of copper sulfides (Fig. 24b). Among all, they observed that SNC@Cu$_2$S (Cu$_2$S coated sulfur, nitrogen-co-doped carbon) without Cu vacancies displays a high FE for formate production. In contrast, the other two catalysts,

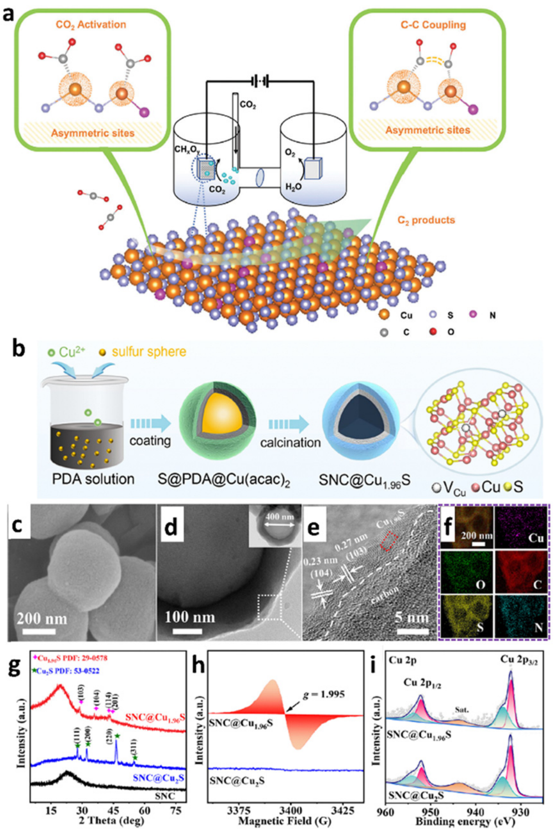

Fig. 24 (a) Illustration of the key hypothesis: the rate of C–C coupling by CO dimerization can be manipulated using structurally asymmetric metal$^{\delta 1+}$–metal$^{\delta 2+}$ pair sites ($0 < \delta_1^{+} \neq \delta_2^{+}$). A well-ordered CuS$_x$ surface facet with surface Cu atoms adsorbing CO$_2$ molecules is shown. Dopant atoms introduce electronic asymmetries in Cu site pairs by adjusting electron-withdrawing/donating properties. Asymmetric CO chemisorption energies favor CO dimerization and hence ECO$_2$R to C$_2$ products. By contrast, sites with even electronic distributions feature strong dipole–dipole repulsion forces during CO$_2$ activation, which seriously hinders CO dimerization (reproduced with permission from ref. 171, copyright Wiley-VCH GmbH 2022). (b) Schematic showing the synthetic process of SNC@Cu$_{1.96}$S. Characterization of Cu vacancies in SNC@Cu$_{1.96}$S. (c) SEM image, (d) TEM image, (e) HR-TEM image, and (f) the elemental mapping images of SNC@Cu$_{1.96}$S. (g) XRD patterns of SNC@Cu$_{1.96}$S, SNC@Cu$_2$S, and SNC. (h) EPR spectra and (i) Cu 2p XPS spectra of SNC@Cu$_{1.96}$S and SNC@Cu$_2$S (reproduced with permission from ref. 172, copyright ACS 2022).

SNC@Cu$_x$S and SNC@Cu$_{1.96}$S, with Cu vacancies, generated CO as the primary product (Fig. 24c–i). Firstly, the Cu vacancies present in Cu$_{1.96}$S modify the S sites' electronic structures and significantly increase the energy barrier of H* formation. At the same time, the Cu vacancies generate the appropriate binding energy for the *COOH intermediate while attenuating the adsorbate–metal interaction. These advantageous characteristics, when combined, result in the favoured formation of CO over formate. Furthermore, the Cu vacancies lower charge transfer resistance, enrich the electronic structure of active sites and increase CO$_2$ adsorption capacity, enhancing the ECO$_2$R activity of SNC@Cu$_{1.96}$S.

Huang and his colleagues[173] synthesized Cu$_2$O-derived Cu catalysts doped with sulfur by immersing the Cu substrates in ammonium polysulfide solutions. Regarding cost, availability, longevity, and catalytic efficacy, the catalyst outperforms alternative materials for ECO$_2$R to formate. Their XPS, ToF-SIMS, and μXRF analyses revealed a positive correlation between catalyst sulfur content and formate production. According to their findings, among all the prepared electrocatalysts, Cu-5000S with 2.7% atomic sulfur has satisfactory catalytic activity with a faradaic efficiency of 75% and a current density of -13.9 mA cm^{-2} at -0.9 V$_{RHE}$ for formate selectivity. Moreover, Cu-5000S exhibits outstanding stability for prolonged CO$_2$ reduction, as evidenced by its formate FE retained at approximately 75% for 12 hours. When sulfur doping was increased, formate production outpaced HER activity, as demonstrated by comparing the SRF-normalized $j_{formate}$ and j_{H_2}. According to investigations of mechanisms, sulfur-doped Cu reduces the binding energy of *COOH intermediates for CO generation, facilitating the synthesis of HCOOH. This work demonstrates that sulfur doping is an effective strategy for enhancing the catalytic selectivity of Cu towards formate and expands the material choice for producing this commercially valuable fuel and chemical.

Li *et al.*[174] examined the influence of the doping strategy on the ECO$_2$R to ethylene using S-doped spherical coral-like CuO catalysts. With a current density of 15.5 mA cm^{-2}, the as-synthesized 5% S–CuO observed a good FE$_{C_2H_4}$ of 48.4% at -1.3 V$_{RHE}$ compared to pure CuO. The 5% S–CuO also retained a consistent FE for C$_2$H$_4$ upon long-term stability testing, with no appreciable drop in current density. The superior performance of 5% S–CuO was derived from the improved dynamic barriers of *CO intermediate dimerization at the Cu active site caused by S-doping, according to the experimental analysis and contact angle measurements. In addition, the hydrophobicity of the 5% S–CuO surface prevented accessible H$_2$O molecules from interacting, thereby preventing competitive HER.

Wang *et al.*[175] discovered various new morphologies of Cu$_2$S-*X* materials reduced to S-Cu$_2$O-*X* during ECO$_2$R in 2022. The researchers found that the optimized electronic structure, aided by the S dopant and microstructure reconstruction, resulted in a large surface area, critical in improving the ECO$_2$R performance and formate selectivity of the S-Cu$_2$O-*X* catalysts. In addition, as compared to Cu(OH)$_2$ and desulfurized Cu$_2$O materials, S-Cu$_2$O-*X* (*X* = 6, 10, and 14) catalysts showed significantly higher catalytic activity in the formation of formate (60–70%). The S-Cu$_2$O-14 catalyst demonstrated a partial current density of 16 mA cm^{-2} at 1.0 V$_{RHE}$ and a FE of 67.2% for formate selectivity with a stability of 20 h among all evaluated electrocatalysts. DFT studies demonstrated that S-doped Cu(111) and S-vacancy (V$_s$) species promoted COOH* or OCHO* intermediates, which accelerated selectivity towards HCOOH pathways.

Recently, Zhang *et al.*[176] showed that S-doped Cu derived from hierarchical hollow-liked CuS polyhedron (CuS-HP) nanostructures synthesised from a MOF significantly improves ECO$_2$R performance in neutral pH water environments (Fig. 25a–j). According to their findings, during electrolysis, the CuS-HP was gradually transformed into an S-doped Cu as the reduction process went on. The *in situ* formed electrocatalyst

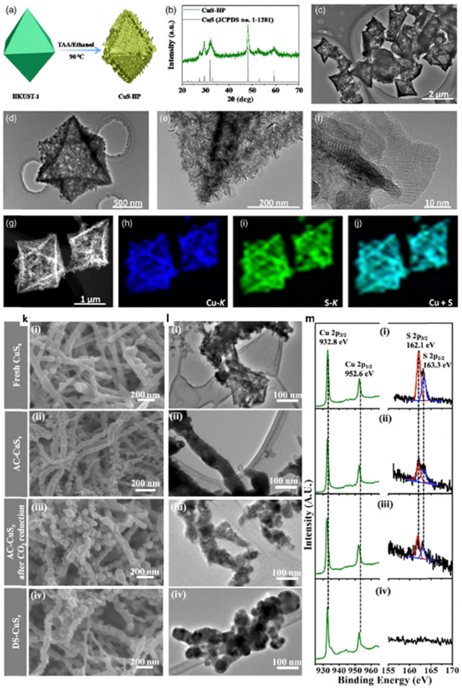

Fig. 25 Structural characterization of CuS-HP. (a) Schematic illustration of the synthetic process. (b) XRD pattern. (c)–(f) TEM images. (g)–(j) HAADF-STEM image and the corresponding EDS elemental mapping images (reproduced with permission from ref. 176, copyright Chinese Chemical Society 2021). (k) SEM images, (l) TEM images, and (m) XPS spectra of (i) fresh CuS_x, (ii) AC-CuS_x, and (iii) AC-CuS_x samples after 40 min of ECO_2R in 0.1 M $KHCO_3$ at -0.85 V_{RHE} and (iv) the DS-CuS_x sample (reproduced with permission from ref. 177, copyright ACS 2018).

exhibited a stability of 36 hours at a $j_{formate}$ of 16 mA cm^{-2} at -0.6 V_{RHE} with a FE of >90%. The DFT study indicates that the Cu(111) facet in S-doped Cu lowers formate activation energy barriers while inhibiting the HER and the reaction intermediates remain unchanged. This work comprehensively explains the mechanisms for improving formate selectivity using CuS electrode materials. Deng *et al.*[177] have experimentally and theoretically demonstrated that sulfur-doped Cu catalyzes the ECO_2R to formate. They synthesized an active CuS_x (AC-CuS_x) catalyst, which exhibited a high FE of 75% and a partial current density of 9 mA cm^{-2} at -0.9 V_{RHE} toward formate production (Fig. 25k–m). It was discovered that sulfur dopants were the key to the increased formate production on the AC-CuS_x surfaces. *Operando* Raman spectroscopy found that S dopants on the catalyst inhibited the CO intermediate formation during ECO_2R, with a lower FE for other products (*i.e.*, CO, hydrocarbons, and alcohols). DFT calculations validated the Raman band assignments. They observed that the adsorption strengths of adsorbed HCOO* were modified by the presence of sulfur on the copper surface, which supported the formation of formate while inhibiting the formation of *COOH, the CO intermediate.

3.7 Catalyst support materials for improving electrocatalytic performance

The supporting materials significantly impact the catalytic performance of electrocatalytic materials. In particular, TMD NSs show promise as supporting materials.[178,179] Composite catalysts have high catalytic performance due to the synergistic interaction of TMDs, supporting materials, and electrocatalysts.[180,181] Kahsay *et al.*[182] successfully deposited copper sulfide nanoparticles onto thermally synthesized copper oxide using a simple and facile SILAR method and examined its catalytic activity for ECO_2R (Scheme 1 in Fig. 26). The modified nanocomposites exhibited high selectivity for formate formation at low overpotential. Remarkably, a maximum faradaic efficiency of 84% and an enhanced partial current density of -20 mA cm^{-2} were obtained at an overpotential of -0.7 V_{RHE}. It was observed that copper sulfides undergo phase changes during ECO_2R, which can contribute to the enhanced electrocatalytic activity. As a result, together with copper oxides, a catalytic synergy is created in the composite, and more favourable adsorption sites are generated to facilitate the ECO_2R. This study paves the way for controlling the composition–selectivity relationship using a facile and scalable catalyst synthesis approach. Also, Li *et al.*[183] produced extremely porous Cu_2O/CuS nanocomposites, as evidenced by X-ray diffraction (XRD), Raman spectroscopy and scanning electron microscopy (SEM) (Fig. 26a–i), showing a better formate FE of 67.6% at a j_{HCOOH} value of 15.3 mA cm^{-2} at -0.5 V_{RHE} in ECO_2R. More significantly, with the same applied potential, the current density remained unchanged for at least 30 hours with an average FE of 62.9%. DFT modelling showed that CuS(110) facets favour HCOOH over CO, with substitutional surface O_S or vacancy V_S species expected to result in lower onset potentials and increased catalytic activity, with both COOH*- and OCHO*-mediated ECO_2R routes predicted to be involved. As a result, this increases the yield of HCOOH with a better current density than the Cu, CuS, and Cu_2O electrocatalysts.

4. Theoretical studies of Cu/S-based ECO_2R Catalysts

As knowledge of electrocatalysis grows, scientists are no longer satisfied with investigating macroscopic phenomena in experimentation; instead, they are exploring the complex microscopic world to gain insight into the mechanism underlying electrocatalytic reactions. This effort is significant for the design and evaluation of highly efficient electrocatalysts. The rapid development of supercomputers has resulted in significantly greater computational speed and performance, enhancing theoretical calculations. In addition, modelling and simulated environments are now closely consistent with the experimental surroundings, resulting in accurate results.[184–186] Nowadays, computational models are used not only to shed light on experimental phenomena but also to direct research strategies and the development of efficient electrocatalysts.[184–186]

Inspired by this, Fonseca *et al.* discussed theoretically how the tuning ratio of Cu/S on 2D CuS_x nanomaterials influenced the ECO_2R performance.[187] Their findings demonstrate that the adsorption modes and strength of the ECO_2R intermediate on CuS_x monolayers vary considerably based on the Cu/S ratio, resulting in different catalytic activities. For instance, $CuS_{0.5}$

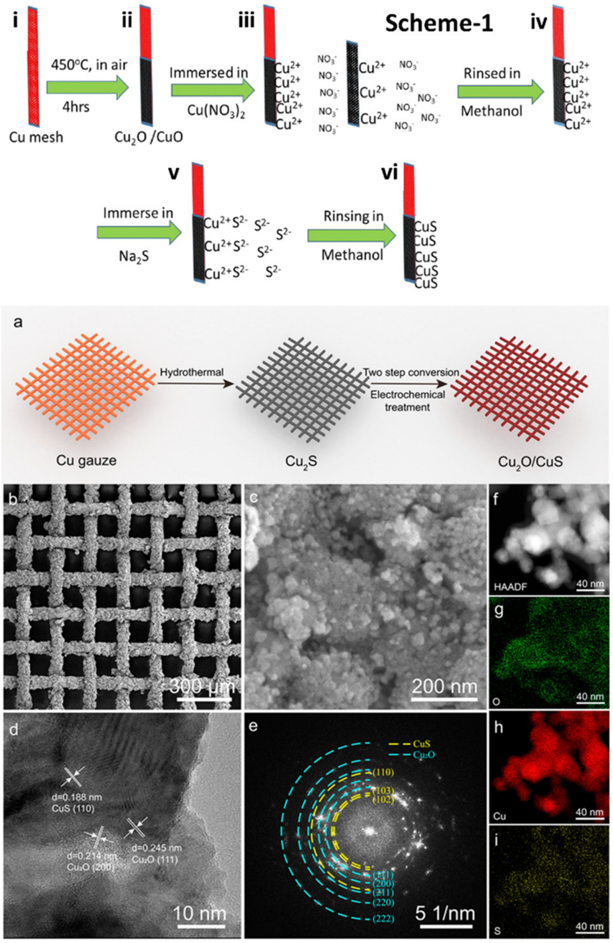

Fig. 26 Scheme 1: illustration of thermal oxidation and SILAR growth: (i) copper mesh before thermal oxidation, (ii) Cu_2O/CuO grown on copper mesh, (iii) adsorption of Cu^{2+} and NO^{3-} and the formation of an electrical double layer, (iv) rinsing (I) removes excess unabsorbed Cu^{2+} and NO^{3-}, (v) reaction of S^{2-} with pre-adsorbed Cu^{2+} ions to form CuS, and (vi) rinsing (II) to remove excess and unreacted species and form the solid solution CuS on surface of the Cu mesh/Cu_2O/CuO (reproduced with permission from ref. 182, copyright Springer 2019). (a) Schematic illustration of the synthesis of Cu_2O/CuS nanocomposites. (b) and (c) SEM images of Cu_2O/CuS nanocomposites grown on a copper gauze collected at different magnifications. (d) HR-TEM image collected from a representative Cu_2O/CuS particle. (e) The corresponding FFT image of (d). Blue and yellow dashed lines highlight the diffraction rings of polycrystalline Cu_2O and CuS particles, respectively. (f)–(i) HAADF-TEM image of Cu_2O/CuS nanocomposites and the corresponding mapping images of elements O, Cu, and S (reproduced with permission from ref. 183, copyright ACS 2021).

catalytic systems showed high onset potential values even though the system was slightly more favourable for reduction toward HCOOH than CO. The CuS system's minimal onset potential for CO or HCOOH suggests that the system could potentially act as a catalyst to form 2e⁻ products. In comparison, $CuS_{1.5}$ revealed minimal onset potential values for the generation of CO, HCOOH, CH_4, and CH_3OH, which are, respectively, 0.19, 0.19, 0.53, and 0.53 (V_{RHE}) less than the values determined for Cu(111). The simulation also revealed that, on $CuS_{1.5}$, the reaction toward CH_4/CH_3OH was limited by the *CO → *COH formation, while on both the $CuS_{1.5}$ and CuS surfaces, the CO_2 → *COOH generation was the potential determining step for CO and HCOOH formation. According to the calculation, the facile *CO desorption on CuS surfaces could restrict the formation of CH_4/CH_3OH. Therefore, methods for breaking the *CO and *COOH or *CHO/*COH interactions' linear scaling could be investigated as well in order to enhance most of these systems, while the performance of CuS as a catalyst for the production of CH_4 and CH_3OH could be improved by simply increasing the CO adsorption strength. In summary, their DFT calculation discovered that increasing the sulfur content in 2D copper sulfide materials promotes CO and HCOOH formation at lower applied potentials and facilitates methane and methanol production. Although these outcomes seem promising from a thermodynamic standpoint, more research into the kinetic behaviour of processes using the most promising systems, considering defect creation under operating conditions, and more research examining additional reaction pathways are essential for strengthening the concept of using these systems as potential electrocatalysts.

Another group proposed experimentally supported theoretical simulation to investigate the mechanism of ECO_2R on S-modified Cu electrocatalysts for HCOOH selectivity.[188] They discovered that the surrounding environment and symmetry of the remaining sulfur atoms greatly influence their stability. Most sulfur exists in somewhat unstable forms that satisfy the strong CO* surface-enhanced infrared absorption spectroscopy signal and the experimentally confirmed negative XPS shift. From the ECO_2R energy graphics, it was revealed that these types of S atoms cannot immediately promote formic acid generation; instead, they produce a highly dominant CO* and have a large CO* adsorption capacity. However, the study discovered that the sulfur atoms' strong CO* adsorption improves the CO* coverage to an almost four times higher level than on a bare Cu. With such a dense CO* coverage, specific surface reactive sites are restricted, resulting in a solution-phase CO_2 reduction pathway leading to the formation of highly selective HCOOH. Also, it has been found that CO* can considerably stabilize residual S, and the adsorption and associated electronic structure modulation studies have revealed the source of CO* adsorption improvement. Lastly, the group proposed a synergy between residual S and CO* dominating the HCOOH formation in ECO_2R using experimental findings from published research and their DFT calculations.[118,177] These findings offer novel insights into the fundamental role of atomic sulfur in the selective formation of ECO_2R products and intermediates on metallic Cu electrodes. Advanced characterization techniques, *i.e.*, *in situ*/*operando* studies[189] and computational approaches,[190,191] must be correlated to better understand the structure–stability–efficiency connections of electrocatalysts. This connection is also essential because of the high selectivity of these catalysts regarding particular catalytic processes and product generation.

5. Perspectives on Cu/S-based ECO_2R catalysts

The catalyst's nanostructure, porosity, morphology, stability, surface area, and particle size influence ECO_2R by affecting the adsorption and desorption of CO_2 molecules. These changes in adsorption and desorption processes lead to different products. In addition to the several modification strategies, the performance of Cu/S-based nanomaterials towards ECO_2R is strongly connected with several other factors. This section highlighted the novelty aspects related to Cu/S-based nanomaterials.

Controlled morphology is critical for understanding the structure–activity relationships of Cu/S-based nanomaterials in ECO_2R catalysis. For example, Cu/S-based nanomaterials have been developed with various nanoscale morphologies, including nanoarrays,[111] cubes,[104] ultrathin nanosheets,[150] hollow polyhedrons,[176] and hierarchical structures.[150] Also, it is to be noted that the morphology and ECO_2R performance vary among Cu/S-based nanomaterials due to the precursor effect.[121] The morphology-related characterization studies showed that different sulfur source precursor materials have different solubilities and rates of release during hydrothermal synthesis, resulting in diverse surface morphologies at the end.[121] Several of these catalysts also have highly porous frameworks,[108] aiding electrolyte permeability. Moreover, a greater surface area might offer more multi-active sites, which is also advantageous for producing an optimal nanostructure for improved ECO_2R activity.[151,153]

Notably, the phase engineering approach also has a vital role in ECO_2R. For example, phase changes in Cu/S-based nanomaterials are observed due to S leaching during ECO_2R. For instance, during the reduction process, XPS and HRTEM analyses showed that thermodynamically unstable CuS undergoes phase changes to metallic Cu, CuO, or Cu_2O.[117] For example, Shinagawa *et al.* employed XPS with SAED studies for the post-electrolysis sample. The group observed that during ECO_2R, S-modified materials lose excess sulfur irrespective of initial sulfur concentration due to the cathodic environment, resulting in modification of particle size and the co-existence of Cu_2S and Cu metal, significantly interfering with the electrocatalyst's activity.[128] Zhao's group[110] performed XPS and HRTEM to demonstrate that CuS nanosheets undergo partial reduction to metallic Cu, and the metallic Cu phase is partially oxidized to CuO after ECO_2R. Zhang *et al.*[176] also did XPS and revealed that CuS-HP synthesized from HKUST-1 was transformed to Cu(S) with a minimal $S^{\delta-}$ ($0 \leq \delta \leq 2$) and metallic Cu. This study revealed that although Cu(S) has minimal S concentrations, the polyhedron structures offer high activity and stability during the ECO_2R. As a result, *in situ* reconstruction of CuS in ECO_2R promotes the ECO_2R activity and product selectivity.

Utilizing highly conducting substrates to load copper sulfides, such as copper oxide,[182] carbon-based materials,[119] and highly porous 3D foams,[111] improves electron conduction and generates more electrocatalytic active sites. Notably, forming copper sulfides–conducting substrate bonds improves catalyst stability, resulting in a longer lifetime.[119]

Other techniques for increasing catalytic activity include the compositional changes of bi-metallic sulfides in comparison to mono-metallic sulfides to generate a heterostructure capable of providing synergistic coupling,[160] interfacial phenomena,[161] and defect-rich structures[142] to maximize the benefits of metals and sulfides. The number of exposed active sites can be increased, and ECO_2R performance can be improved through heterostructure engineering strategies by doping highly functional single-metal nanoparticles[169] and non-metals[171] on metal sulfides. Also, constructing heterostructures can improve ECO_2R efficiency by adjusting the interfaces and electrical states and offering more active sites. So, lower onset potential, increased cathodic current, higher TOF, and lower Tafel slope values can be obtained during the ECO_2R process.[187]

Furthermore, the ECO_2R performance varies across Cu/S-based nanomaterials based on their S content or S-vacancy concentration. Vacancy creation through defect engineering techniques, *i.e.*, S-vacancy[162] and Cu-vacancy,[172] can shift the product selectivity of ECO_2R to C_{2+} products by modifying the electronic structure of S and Cu sites in Cu/S-based nanomaterials.

6. Comparative analysis of Cu/S-based ECO_2R catalysts with other best-performing Cu-based and metal–sulfide-based ECO_2R catalysts

The performance data and recent research of earlier studies on different Cu/S-based nanomaterials are summarized in Table 1. Tables 2 and 3 present the best-performing Cu-based and metal–sulfide-based nanomaterials (MS-based nanomaterials) for ECO_2R (other than copper–sulfide-based) to compare the catalytic efficacy of Cu/S-based nanomaterials (summarized in Table 1) with an emphasis on partial current density and faradaic efficiency. Table 1 indicates that many Cu/S-based nanomaterials have demonstrated acceptable levels of stability during the ECO_2R as well as good partial current density and faradaic efficiency for mainly formate/HCOOH production. However, for C_1 and C_{2+} products, the performance of Cu/S-based nanomaterials is unsatisfactory in terms of faradaic efficiency and product selectivity. Other than HCOOH/formate, several Cu/S-based nanomaterials such as N-doped Cu_2S thin layers,[171] polycrystalline Cu (Cu-s),[100] S-doped spherical coral-like CuO,[174] CSVE-Cu,[142] DSV-engineered CuS,[143] S-HKUST-1,[154] CeO_2-modified CuS nanoplates,[158] and Cu_2S nanocrystal-decorated Cu nanosheets,[155] have yielded C_{2+} products. However, their selectivities are much lower compared to those of best-performing Cu-based catalysts, *i.e.*, $dCu_2O/Ag2.3\%$,[192] Ag–Cu_2O,[193] Cu_3N-derived Cu nanowires,[194] CuO-derived Cu,[195] Cu(salophen)-coated GDE,[196] $Cu@Cu_2(OH)_3NO$,[197] Cu_2O films,[198] oxygen-bearing copper,[199] and nano-defective Cu nanosheets.[200] In conclusion, combining Cu/S-based nanomaterials with other nanomaterials, *i.e.*, metal oxides, single-atom metals, metal selenides and metal phosphides, through various engineering/modifications strategies could be effective for higher C_{2+} product selectivity. In addition, cadmium-based sulfide, molybdenum-based sulfide and zinc-based sulfide, as summarized in Table 3, electrocatalysts exhibited better current density and faradaic efficiency performance than Cu/S-based and Cu-based catalysts for CO production. Furthermore, for CH_4 production, the CuS/Ni foam[110] electrocatalyst offered better

Table 1 A current overview of Cu/S-based catalysts for ECO_2R

Products	Electrocatalysts	Method of synthesis	Potential (V_{RHE})	Electrolyte used	Cell	Partial current density (mA cm^{-2})	Faradaic efficiency (%)	Stability (h)	Ref.
HCOOH	Sulfur-modified Cu_2O	Wet chemistry approach	−0.9	0.1 M $KHCO_3$	H-type cell	260 ± 16	≈90	80	99
C_2H_4	Cu-s	Electrochemical reduction	−1.2	0.1 M $KHCO_3$	H-Type cell	40.8	68.6	8	100
HCOOH	PTFE-coated CuS/BM	One-step chemical bath process	−0.7	0.5 mol L^{-1} $KHCO_3$	H-type cell	50	70	1.5	101
CO	Hollow-shaped CuS microcubes	Galvanic replacement technique	−0.16	0.5 M $KHCO_3$	H-type cell	—	32.7	10	104
HCOOH	Hollow ordered porous copper sulfide cuboctahedra	Hard templating strategy	−1.1	0.1 M $KHCO_3$	H-type cell	7.8	70.3	26	108
C_2H_4	Copper sulfide film consisting of nanoparticles	Thermal decomposition	−0.13	1 M $KHCO_3$	H-type cell	≈0.08 (total)	—	—	109
HCOOH	Cu_2S over copper foam	Electrochemical deposition	−2.0 V (*vs.* Ag/Ag^+)	0.5 mol L^{-1} $BmimBF_4$	H-type cell	5.3	85	6	111
CH_4	CuS/Ni foam	Hydrothermal method	−1.1	0.1 M $KHCO_3$	H-type cell	7.32 (total)	73.5 ± 5	60	110
HCOOH	CuS nanoflowers	Ethylene glycol solvothermal method	−0.8 to ∼−1.0	0.1 M $KHCO_3$	H-type cell	≈6.5	∼52	2	117
HCOOH	$Cu_{1.81}S$@MWCNT-600-OD	Two-step coupling approach	−0.67	0.5 M $KHCO_3$	H-type cell	3.75 (total)	82	20	119
HCOOH	Cu_2S@C	Liquid phase sulfidation	−0.78 ± 0.02	0.5 M KCl + 0.5 M $KHCO_3$	H-type cell	1.5 (total)	12	5	120
CO	CuS catalyst thiourea precursors	Hydrothermal synthesis	−0.51	0.1 M $KHCO_3$	H-type cell	—	72.67	5	121
HCOOH	Cu_2S nanocrystals	Electrochemically driven cation exchange method (ED-CE)	−0.9	0.1 M $NaHCO_3$	H-type cell	19	87.3	9	122
HCOOH	Cu_2S	ED-CE	−0.2	0.05 M K_2CO_3	H-type cell	—	≈70	16	123
CO	S-derived Cu–Sb	Heat-up colloidal nanoparticle route	−1.0	1 M $KHCO_3$	Flow cell	37.6	80.5	24	124
HCOOH	S-CNWs	Chemical oxidation followed by solvothermal reaction	−0.59	0.25 M $KHCO_3$	H-type cell	≈10	∼60	2	125
HCOOH	Submicron-sized Cu–S	Solvothermal approach	−0.8	0.1 M $KHCO_3$	H-type Cell	≈10 (total)	80	12	128
HCOOH	CuS_x nanoparticles	Dipping	−0.6	0.1 M $KHCO_3$	H-type cell	2.5	72	72	129
HCOOH	S-Cu_2O/Cu	Hydrothermal reduction followed by *in situ* reconstruction	−1.0	0.1 M $KHCO_3$	H-type cell	5	70	6	134
HCOOH	CuS 811 derived S-doped Cu_2O	Surfactant-free double-replacement reaction		0.1 M $KHCO_3$	Flow cell	321	80	33	135
Alcohols (ethanol + propanol)	CSVE-Cu	Solution-phase growth	−0.95	1.0 M KOH	Flow cell	126	31.6	16	142
n-Propanol	DSV-engineered CuS_x	Lithium tuning approach	−1.05	0.1 M $KHCO_3$	H-type cell	9.9	15.4 ± 1	10	143
HCOOH	SnO_2@C onto snowflake-like Cu_2S	Hydrothermal method	−1.0	0.1 M $KHCO_3$	H-type cell	15.6	88	50	148
HCOOH	CuS/SnO_2-S derived Cu/Sn/$Cu_{6.26}Sn_5$ catalysts	Redox reaction	−0.8	0.5 M $KHCO_3$	H-type cell	≈18.8	84.9	10	149
CO	SnO_2 confined on CuS nanosheets	One-pot precipitation synthesis	−1.0	0.1 M $KHCO_3$	H-type cell	15.24	>85	24	150
HCOOH	Cu_2SnS_3 nanoplates	Step-growth approach	−1.2	1 M $KHCO_3$	Flow cell	181	72.4	3	151
CO	$CuInS_2$ hollow nanostructures	Template-free approach	−0.7 & −1.0	0.1 M $KHCO_3$	H-type cell	≈13 (total)	82.3	4	152
HCOOH	Graphdiyne/copper sulfide	Hydrothermal followed by *in situ* growth	−0.9	0.1 M $KHCO_3$	H-type cell	65.6 (total)	70	4	153
C_2H_4	S-HKUST-1	Local sulfur doping strategy	−1.94	1.0 M KOH	Flow cell	228	57.2	8	154
Ethanol	Cu_2S nanocrystal-decorated Cu nanosheets	Hydrothermal followed by self-assembly	−1.2	0.1 M $KHCO_3$	H-type cell	$j_{C_2H_5OH} = 20.7$	46	20	155
CH_4	Cu_xZn_yS nanoparticles	Seed-mediated growth method	−0.98	0.1 M $KHCO_3$	H-type cell	$j_{\text{methane}} = 4.58$	76	5	156
Ethanol	SD-$CuCd_2$	Co-Precipitation	−0.8	0.1 M $KHCO_3$	H-type cell	0.6	32	6	157
C_{2+} products	CeO_2-modified CuS nanoplates	Self-assembly method	−0.9	1 M KOH	Flow cell	$J_{C_{2+}} = 75.3$	75	180	158
HCOOH	Bi/CeO_2/CuS	Solvothermal process	−0.9	0.5 M $KHCO_3$	H-type cell	17 (total)	88	6	159
HCOOH	Heterostructure Bi–Cu_2S nanocrystals	One-pot solution-phase approach	−1.0	0.1 M $KHCO_3$	H-type cell	∼17	>98	10	160
HCOOH	CuS@1T-N-WS_2/WO_3	A facile solvothermal process followed by a reflux strategy	−1.3	0.5 M $KHCO_3$	H-type cell	125.05	∼55.6	2	161
CO	MoS_2–CuS	Hydrothermal approach	−0.6	0.1 M $KHCO_3$	H-type cell	3.6	83.2	5.55	162

Table 1 (*continued*)

Products	Electrocatalysts	Method of synthesis	Potential (V_{RHE})	Electrolyte used	Cell	Partial current density (mA cm^{-2})	Faradaic efficiency (%)	Stability (h)	Ref.
Ethanol	Mo^{4+}-doped CuS nanosheet-assembled hollow spheres	One-step solution-phase approach	−0.6	1.0 M KOH	Flow cell	$J_{ethanol} = 186.5$	67.5	14	169
HCOOH	Cu-doped Bi derived from CuS–Bi_2S_3	Solvothermal followed by *in situ* reconstruction	−0.86	1 M KOH	MEA cell	1132	90	100	170
C_2H_4	N-doped Cu_2S thin layers	Annealing process	−0.98	0.1 M $KHCO_3$	H-type cell	∼2.6	14.72	0.25	171
CO	SNC@$Cu_{1.96}S$	Surface coating and calcination	−0.84	0.5 M $KHCO_3$	H-type cell	37.2	85.2	13	172
HCOOH	Cu-5000S	Electrochemical deposition	−0.8	0.1 M $KHCO_3$	H-type cell	13.9	≈75	12	173
C_2H_4	Sulfur-doped spherical coral-like CuO	Local sulfur doping strategy	−1.3	0.1 M $KHCO_3$	H-type cell	15	48.4	20	174
HCOOH	S-Cu_2O-14	Hydrothermal sulfurization method followed by an electrochemical reduction process	−1.0	0.1 M $KHCO_3$	H-type cell	16.3	67.2	20	175
HCOOH	CuS hollow polyhedron derived from a MOF	MOF self-sacrificial template method	−0.6	0.5 M K_2SO_4 aqueous solution	H-type cell	≈16	>90	36	176
HCOOH	AC-CuS_x	Pulsed electrochemical deposition	−0.9	0.1 M $KHCO_3$	H-type cell	9	75	3	177
HCOOH	CuS deposited onto thermally prepared Cu_2O/CuO heterostructure	Thermal oxidation followed by SILAR	−0.7	0.1 M $KHCO_3$	H-type cell	20	84	2.5	182
HCOOH	Cu_2S/Cu_2O nanocomposites	Hydrothermal approach and electrochemical treatment	−0.9	0.1 M $KHCO_3$	H-type cell	12.3	67.6	30	183

performance than Cu/MoS_2[201] and $Fe_{4.5}Ni_{4.5}S_8$[202] regarding partial current density and faradaic efficiency.

7. Practical applications of Cu/S-based ECO_2R catalysts

The execution of ECO_2R on Cu/S-based catalysts on a practical level is still in its initial stages due to several difficulties. The primary challenges to the commercialization of Cu/S-based ECO_2R catalysts are (1) considerable CO_2 extraction and purification costs, as ECO_2R needs highly pure (99.999%) CO_2, (2) high energy consumption, (3) low yield of energy-dense C_{2+} products and (3) a restricted marketplace that is less attractive to investors.[285,286] In addition, there are multiple technical obstacles related to ECO_2R, such as low catalytic performance, poor product selectivity, unsatisfactory catalytic stability, and non-optimization of cell design for use in practice.[287,288] While Cu/S-based materials yielded several products during ECO_2R, producing formate/HCOOH was observed as the main product. However some catalysts can produce hydrocarbons, but their selectivities are much lower than those of copper nanoparticles or oxide-derived copper. This section discusses the possibilities of scaling up ECO_2R technology to the industrial level, focusing on the practical applications of formate/HCOOH production.

Indeed, scaling up an ECO_2R cell for formate/HCOOH production is complex because various factors and constraints must be investigated and carefully evaluated to maintain stable cell efficiency.[289] A study revealed that the cell must maintain consistent operation for at least 8000 hours for commercial applications. Additionally, it should exhibit an overpotential below 1.0 V_{RHE}, a partial current density between 200 and 1000 mA cm^{-2}, and a formate/HCOOH faradaic efficiency of above 90% during stable operation.[290] Another research stated that the electrolyzer should be stable for a minimum of 20 000 hours to be financially viable.[291] In this context, the proton exchange membrane and electrode framework also play a vital role in stabilizing the cell. Among the various membranes reported, bipolar membranes have received much attention for large-scale use because they can maintain pH gradient, decrease liquid crossover, and promote water separation at the membrane electrolyte interface.[292,293] Operating variables such as electrolyte, flow rate, p^H, and CO_2 feed type can all be optimized to improve cell efficiency.[294] Nowadays, there are only a few huge-scale CO_2 electrolyzers for methane, CO, C_1, C_{2+}, and formic acid generation.[295,296] Few academic institutions executed large-scale manufacture of formate/formic acid using ECO_2R. For example, in 2008, a pilot plant was constructed with a maximum output of 146 kg CO_2 per day, leading to approximately 110 kg formic acid per day at an operating pressure of around 10 bar.[297] A different approach to the current scale-up investigation revealed a pre-pilot facility output of 55 kg CO_2 per day, resulting in approximately 12 kg of formate per day at ambient pressure.[298]

While the aforementioned studies demonstrated the practicality of this approach for scaling up, several obstacles must be addressed to maximize plant functionality. One of the primary

Table 2 An overview of other Cu-based ECO_2R catalysts

Electrocatalysts	Main products	Potential (V_{RHE})	Electrolyte used	Cell	Current density (mA cm^{-2})	Faradaic efficiency (%)	Stability (h)	Ref.
Single Cu atom	Acetone	−0.76	0.1 M $KHCO_3$	H-type cell	1.0	36.7	5	203
TS-Cu	Ethylene	3.5	1 M KOH	Flow cell	800	72	200	204
$dCu_2O/Ag2.3\%$	Ethanol	−0.87	1 M KOH	H-type cell	326.4	40.8	12	192
Cu-NC	Ethanol	−1.01	0.1 M $KHCO_3$	H-type cell	—	18.4	8	205
Cu_2O/NCS	Ethylene	−1.3	0.1 M $KHCO_3$	H-type cell	—	24.7	4	206
CuN_4	Ethanol	−1.2	0.1 M $KHCO_3$	Flow cell	16.2	55	1	207
Cu_1Ni_2@N-MWCNT	Formate	−0.53	0.1 M $KHCO_3$	H-type cell	3.0	90	10	208
Cu-doped carbon xerogel	Methane		0.1 M $KHCO_3$	H-type cell	—		5	209
Cu-nanoparticles	Formate	−1.0	0.1 M $KHCO_3$	H-type cell	6.53	54	12	210
GO-VB6-Cu-2	Ethanol	−0.250	0.1 M $KHCO_3$	H-type cell	7.452	56.3	24	211
Cu–N–C	Carbon mono oxide	−0.7	0.1 M $KHCO_3$	H-type cell	3.61	92	60	212
Cu_2O@Cu-MOF	Methane	−1.71	0.1 M $KHCO_3$	H-type cell	8.4	79.4	1	213
PcCu–Cu–O	Ethylene	−1.2	0.1 M $KHCO_3$	H-type cell	7.3	50	4	214
$Cu_{90}In_{10}/C$	Carbon mono oxide	−0.75	0.1 M $KHCO_3$	H-type cell	9.85	85	4	215
CuO/CuTCPP	Formic acid	−1.65	0.5 M $EMIMBF_4$	H-type cell	4.5	85.2	5	216
Cu(111)@Cu-THQ	Ethylene	−1.4	0.1 M $KHCO_3$	H-type cell	14.3	42	8	217
CuZn	C_{2+}	−1.0	0.1 M $KHCO_3$	H-type cell	1.5	25	7	218
Cu@Cu_xO	C_{2+}	−1.78	0.1 M $KHCO_3$	H-type cell	150	70	20	219
Cu–Sn	Carbon monoxide	−0.7	0.1 M $KHCO_3$	H-type cell	4.5	90	12	220
Cu_3N-derived Cu nanowires	C_2	−1.0	0.1 M $KHCO_3$	H-type cell	−50.6	86	28	194
CuO-derived Cu	C_{2+}	−0.48	KH_2PO_4	H-type cell	−210	9.6	1	195
Cu_v–Cu_2O	Ethylene	−0.76	0.1 M $KHCO_3$	H-type cell	15.7	51	10	221
Cu–Zn	Carbon monoxide	−1.1	0.1 M $KHCO_3$	H-type cell	4.3	74	4	222
Cu@$Cu_2(OH)_3NO$	Ethylene	−1.2	0.1 M $KHCO_3$	H-type cell	80	31.8	20	197
Cu_2O-derived Cu/$PdCl_2$	Ethylene	−1.0	0.1 M $KHCO_3$	Flow cell	—	30.1	8	223
Cu_2O films	C_2	−0.99	0.1 M $KHCO_3$	H-type cell	−52	39	1	198
Cu_2O-derived Cu particles	Ethylene	−0.98	0.1 M $KHCO_3$	H-type cell	−13.3	43	1	224
Branched CuO nanoparticles	Ethylene	−1.0	0.1 M $KHCO_3$	H-type cell	−22.0	53	12	225
Cu–Pd alloy	Carbon monoxide	−0.9	0.1 M $KHCO_3$	H-type cell	—	87	5	226
Cu–Pt alloy	Methane	−1.6	0.1 M $KHCO_3$	H-type cell	0.598	21	0.5	227
CuMgAl LDH	Acetic acid	−0.4	0.1 M $KHCO_3$	Flow cell	—		24	228
PD-CuO_x/C	Ethylene	−1.4	0.1 M $KHCO_3$	MEA cell	26.0	45	48	229
$CuCo_2Se_4$	Acetate	−0.25	0.3 M $NaHCO_3$	H-type Cell	26	100	100	230
Cu(salophen)-coated GDE	C_{2+}	−1.2	1 M KOH	H-type cell	121	37	2	196
Ag–Cu_2O	Acetic acid	−0.9	1 M KOH	H-type cell	310	70	20	193
Hydroxo-bridged phenanthroline Cu(II) molecule	Ethylene	−1.25	0.1 M $CsHCO_3$	H-type cell	−5.5	42	15	231
Cu NC spheres	Ethylene	−1.1	0.1 M $KHCO_3$	H-type cell	−9	41	1	232
Copper electrodes	Methane	−1.2	0.1 M $KHCO_3$	H-type cell	5	45	8	233
Oxygen-bearing copper	Ethylene	−0.95	0.3 M $NaHCO_3$	H-type cell	44.7	45	1	199
Nano-defective Cu nanosheets	Ethylene	−1.0	0.1 M K_2SO_4	Flow cell	66.5	83.2	1	200

Table 3 An overview of other metal–sulfide-based ECO_2R catalysts

Metal–sulfides	Electrocatalysts	Potential (V_{RHE})	Electrolyte used	Main products	Cell	Partial current density (mA cm^{-2})	Faradaic efficiency (%)	Stability (h)	Ref.
Cadmium-based sulfide	Ag–CdS_{1-x}	−1.1	1 M $KHCO_3$	CO	H-type cell	53.7	87.1	—	234
	P–Cd|S	−0.8	0.5 M $KHCO_3$	CO	H-type cell	89.8	88	10	235
	Nanoneedle-shaped CdS	−1.2	0.1 M $KHCO_3$	CO	Flow-cell	212	95.5 ± 4.0	24	236
	CdS nanorods	−1.2	0.1 M $KHCO_3$	CO	H-type cell	~22	81	10	237
	CdS with S-vacancy	−0.8 to −1.1	0.5 M $KHCO_3$	CO	H-type cell	~1.3	95	40	238
	S vacancy engineered CdS nanorods	−1.1	0.5 M $KHCO_3$	CO	H-type cell	20.5	100 ± 0.5	10	239
	CdS supported CNTs	−1.2	0.1 M $KHCO_3$	CO	H-type cell	~13 (total)	~95	10	240
	CdS/MXene	−1.0	0.1 M $KHCO_3$	CO	H-type cell	~6	94	8	241
	Ag_2S/CdS	−1.1	0.5 M $KHCO_3$	CO	Flow-cell	10.6	95	20	242
Tin-based sulfide	Hybridized composite of defective SnS_2 nanosheets and Ag nanowires	−0.1	0.5 M $KHCO_3$	HCOOH	H-type cell	23.3	60	10	243
	5% Ni-doped SnS_2 nanosheets	−0.9	0.1 M $KHCO_3$	CO & HCOOH	H-type cell	19.6 (total)	93	8	244
	Sn(S)/Au	−0.75	0.1 M $KHCO_3$	HCOOH	H-type cell	51	93.3	40	245
	Stannous sulfide modified with amino-functionalized carbon	−0.9	0.5 M $KHCO_3$	HCOOH	H-type cell	41.1	92.6	15	246
	SnS_2 nanosheets supported on rGO	−1.4	0.5 M $NaHCO_3$	HCOOH	H-type cell	11.75	84.5	2	247
	Tin(IV) sulfide monolayers	−0.8	0.1 M $KHCO_3$	HCOOH	H-type cell	~45 (total)	94 ± 5	80	248
	N–Sn(S) nanosheets	−0.7	0.1 M $KHCO_3$	HCOOH	Flow-cell	25 (total)	93.3	20	249
	Semimetal phased 1H-SnS_2	−0.8	0.1 M $KHCO_3$	CO	H-type cell	10.9	98.2	15	250
Bismuth-based sulfide	S doped-Bi_2O_3-CNT	−0.9	0.5 M $KHCO_3$	HCOOH	H-type cell	48.64	97.06	10	251
	S-derived Bi	−0.75	0.5 M $NaHCO_3$	HCOOH	H-type cell	5 (total)	84	24	252
	Bi_2S_3–Bi_2O_3/rGO	−0.9	0.1 M $KHCO_3$	HCOOH	H-type cell	~3.8	90	24	253
	Bi–Bi_2S_3	−1.0	0.1 M $KHCO_3$	HCOOH	H-type cell	~14	85	12	254
	S-doped two-dimensional (2D) bismuth subcarbonate (S-BiOC)	−0.9	0.5 M $KHCO_3$	HCOOH	H-type cell	29	>90	20	255
	Bi_2S_3–PPy	−0.9	0.5 M $KHCO_3$	HCOOH	H-type cell	56.95 (total)	91.18	>110	256
	2D defective Bi_2S_3 NSs	−0.93	0.5 M $KHCO_3$	HCOOH	H-type cell	~30	>90%	200	257
Molybdenum-based sulfide	Bulk MoS_2	−0.764	4 mol% EMIM-BF_4 solution	CO	H-type cell	65	98	10	258
	rGO–PEI–MoS_x	−0.65	0.5 M $NaHCO_3$	CO	H-type cell	55 (total)	85.1	—	259
	N-MoS_2@NCDs-180	−0.9	6 mol% EMIM-BF_4 solution	CO	H-type cell	36.2	90.2	10	260
	Cu-g-C_3N_4/MoS_2	−0.67	0.5 M $KHCO_3$	CH_3OH	H-type cell	78	19.7	30	261
	CuO–ZnO–MoS_2	−0.6 & −0.9	0.5 M $KHCO_3$	Methanol & ethanol	H-type cell	121 (total)	24.6 & 11.1	3	262
	NCMSH	−0.7	4 mol% EMIM-BF_4 solution	CO	H-type cell	34.31	92.68	24	263
	Cu/MoS_2	−1.4 V_{SCE}	0.1 M $KHCO_3$	CH_4	H-type cell	~3.2	17.08	48	201
	VA-$Mo_{0.95}Nb_{0.05}S_2$	−0.8	50 vol% EMIM–BF_4	CO	H-type cell	237 (total)	80	—	264
	Cu_2O@MoS_2 nanosheets	−1.3 and −1.1	0.5 M $KHCO_3$	Methanol & ethanol	H-type cell	113 (total)	12.3 & 7.9	2	265
	H-E-MoS_2 with decoration of fluorosilane	−0.9	6 mol% EMIM-BF_4 solution	CO	H-type cell	—	81	10	266
	Monolayers of MoSeS alloys	−0.15	4 mol% EMIM-BF_4 solution	CO	H-type cell	43	45.2	10	267
Indium-based sulfide	In nanoparticles on In_2S_3 nanosheets	−1.0	1 M $KHCO_3$	HCOOH	H-type cell	40.3	76	8	268
	Mn–In_2S_3	−0.9	0.1 M $KHCO_3$	HCOOH	H-type cell	20.1 (total)	90	8	269
	$ZnIn_2S_4$	−1.18	1 M $KHCO_3$	HCOOH	Flow cell	~298	99.3	60	270
	Flower-shaped In_2S_3	−2.3	$BmimPF_6$/MeCN–H_2O solution	HCOOH & CO	H-type cell	25.6	86	10	271
	S–In	−0.98	0.1 M $KHCO_3$	HCOOH	H-type cell	84 (total)	93	10	272

Table 3 (*continued*)

Metal–sulfides	Electrocatalysts	Potential (V_{RHE})	Electrolyte used	Main products	Cell	Partial current density (mA cm^{-2})	Faradaic efficiency (%)	Stability (h)	Ref.
	ZnO NW/CIGS/InS	−0.24	0.1 M $KHCO_3$	HCOOH	H-type cell	0.35	77.2	10	273
	ZnO NF/CIGS/InS	−0.24	0.1 M $KHCO_3$	HCOOH	H-type cell	—	68.1	—	273
Lead-based sulfide	Wafer-structured sulfur-derived Pb	−1.08	0.1 M $KHCO_3$	HCOOH	H-type cell	12	88	—	274
	PbS nanocrystals	−1.2	0.1 M $KHCO_3$	HCOOH	H-type cell	—	97.6 ± 5.3	10	275
Zinc-based sulfide	ZnS@Zn	−2.4 $V_{Fc/Fc+}$	Propylene carbonate/ $(CH_3CH_2CH_2CH_2)_4N(ClO_4)$	CO	H-type cell	6.4	92	4	276
	S–Zn–S nanosheets	−0.8	0.1 M $KHCO_3$	CO	H-type cell	∼11	94.2	15	277
	ZnS@ZnO	−0.56	1 M KOH	CO	H-type cell	∼109	97.2 ± 0.5	40	278
	TA-ZnS	−1.9 $V_{Ag\|AgCl}$	0.1 M $KHCO_3$	CO	H-type cell	∼7	∼83	20	279
Titanium-based sulfide	Semi-metallic titanium disulfide (TiS_2)	−0.5	0.1 M NBu_4–PF_6	CO	H-type cell	5	83	16	280
Other bimetallic-sulfide	Ni_2FeS_4 nanosheets	−0.7	0.1 M $KHCO_3$	CO	H-type cell	—	5.9	1	281
	FeS_2/NiS nanocomposite	−0.6	0.5 M $KHCO_3$	CH_3OH	H-type cell	3.1 (total)	64	4	282
	Bulk Fe/Ni sulfides ($Fe_{4.5}Ni_{4.5}S_8$ pentlandite)	−1.80 V_{NHE}	0.1 M $TBAPF_6$	CO & methane	H-type cell	3 (total)	87 & 13	15	202
	$Fe_3Ni_6S_8$	−1.80 V_{NHE}	0.1 M $TBAPF_6$/acetonitrile solution	CO	H-type cell	15 (total)	3.6	8	283
	$Fe_{4.5}Ni_{4.5}S_4Se_4$	−1.80 V_{NHE}	Acetonitrile	CO	H-type cell	11	84	2	284

challenging tasks is maintaining a higher constant current density (recommended >200 mA cm^{-2}) during the ECO_2R process. The higher current density value denotes a high electrochemical reaction rate, which raises the rate at which different products are produced. Notably, the electrode's properties and structure, as well as that of both the catalyst and the support material, significantly impact the current density. The lower energy efficiency presents another difficulty. The system demonstrated 28% and 33% energy efficiency in a lab-scale three-compartment set-up over a 1000-hour operation at current densities >100 mA cm^{-2}.[299] But, during 450 minutes of operation on a pilot scale, the energy efficiency exceeds 50%.[297] However, data on the energy efficiency of various products formed on a large/pilot scale are scarce. Notably, the FE should be higher and the overpotential lower to maintain high cell energy efficiency. The support material on the working electrode, electrocatalytic properties, and anode materials primarily determine these parameters. In addition, the choice of the membrane is crucial because it may substantially decrease the IR drop between the compartments, *i.e.*, cathodic and anodic, lowering the cell overpotential and increasing energy efficiency. It is advised that the potential is between 2.5 and 3 V and that the FE is higher than 90% for industrial-scale implementation.[300–302]

The cell construction for ECO_2R to formate/formic acid remains to be developed for industrial use. Every design has pros and cons of its own. However, the PEM cell layout appears to be a viable strategy for scaling up.[303] The PEM design demonstrated a reasonably higher FE for formic acid generation for Cu/S-based electrocatalysts with a stable cell procedure of more than 100 hours.[170] However, multiple challenges restrict the commercial use of PEMs for ECO_2R to formate/formic acid and other products (*i.e.*, C_1 and C_{2+} products), including declination of membrane performance over time and GDE flooding. When the cell is operated at high pressure, the mechanical strength of the membrane becomes a significant issue, leading to a higher crossover rate of formic acid and membrane damage. Also, further research must be carried out on enhancing cell stability and efficiency. Although the PEM cell demonstrated a FE of 90% and steady performance for 100 hours,[170] industrial applications necessitate cell performance for a minimum of 8000 hours with a FE greater than 90%.[290] Design aspects and operational variables should be considered when designing a cell assembly that can sustain long-term operation, encounter commercial operation demands, and be cost-effective. However, membranes are costly and need periodic replacement. According to researchers, membrane-less ECO_2R cells require more care to prevent frequent maintenance or membrane damage. Another significant problem is the overflow of GDE with electrolytes, which could harm the electrode structure and lower CO_2 conversion. Gas-phase ECO_2R cells may avoid such issues, so more research into these cells is needed to develop efficient, stable, and long-lasting ECO_2R cells.

8. Summary and outlook

This review discusses several strategies for modifying Cu/S-based nanomaterials, which are recognized as highly promising electrocatalysts for ECO_2R. These strategies include adjustments to morphologies, structures, nanosize effects, and heterointerfaces, all of which contribute to triggering electronic modulation effects within the nanomaterials. This modulation leads to the generation of multiple active sites and facilitates charge redistribution, ultimately boosting the adsorption energy of intermediates and enhancing electrocatalytic activity. Additionally, recent advancements in engineered Cu/S-based nanomaterials for ECO_2R are summarized, shedding light on the interplay between engineering strategies, reaction mechanisms, and electrocatalytic performance. This article provides insights into the formation mechanisms, synthetic strategies, and the diverse morphological and compositional variations observed in Cu/S-based nanomaterials.

Despite the progress achieved for the engineered Cu/S-based nanomaterials, there are still some challenges and opportunities that should be addressed based on the following aspects:

(1) Regarding the design and development of Cu/S-based nanomaterials, novel synthesis procedures are required to develop copper sulfide materials with various unique morphologies (*i.e.*, nano-tips, nanoparticles, two-dimensional layered structures, and so on) and crystal and phase structures (*i.e.*, $Cu_{1.97}S$, $Cu_{1.80}S$, and so on) to increase their performance. Also, combining different phases and components of low-cost $Cu_{2-x}S$ templates to create versatile and multifunctional nanocomposite heterostructures promotes ECO_2R catalysis with multi-active sites and synergistic effects.

(2) The actual role of phase changing CuS in the electrolysis process without converting it to CuO, Cu_2O and metallic Cu should be investigated. It is also conceivable to examine the approach of stabilizing S vacancies from a different angle. Therefore, a long-term stability analysis is advised to evaluate the poisoning or degradation of the catalyst, which is vital for the catalyst's design and development.

(3) C_{2+} product selectivity and stability of Cu/S-based nanomaterials for CO_2 reduction should be improved. Most Cu/S-based nanomaterials have relatively high ECO_2R catalytic selectivity and high faradaic efficiency towards CO and HCOOH (as summarised in Table 1), and other C_1 products and high-energy-dense C_2 products are challenging to generate. Thus, obtaining high-energy-dense C_2 products is crucial for commercial electrochemical CO_2 conversion.

(4) Sophisticated characterization technologies should be implemented. For heterogenous electrocatalysis, the catalyst's surface is an essential active site for the catalytic reaction. The interaction between the surface-active sites and the reaction intermediates is the primary factor influencing the catalytic activity. As a result, more cutting-edge *in situ* characterization techniques, such as *in situ* Raman, Fourier transform infrared spectroscopy (FTIR), and X-ray absorption spectroscopy (XAS), must be used to identify the nature of active sites and binding/adsorption energies between active sites and intermediates during ECO_2R on Cu/S-based electrocatalysts.

(5) Execution of comprehensive and advanced theoretical techniques Theoretical modelling and simulation are mandatory to understand the reaction process and establish the structure–activity relationship. Several studies have shown that DFT is a practical approach for determining the energy values of chemical intermediates. Also, many reported theoretically expected processes may differ between DFT models. Also, several computational outcomes may be theoretically possible but not experimentally viable. Thus, DFT analysis is closely linked with experimental outcomes, especially *in situ* technique results, confirming its viability for understanding reaction processes.

Closing the gap between lab-scale research and industrial applications is crucial. Momentous improvements have been observed in the study and in the lab-scale use of Cu/S-based nanomaterials for ECO_2R. However, implementing Cu/S-based electrocatalysts on a large scale for real-world applications remains a significant challenge. Smaller batch preparation and controlled laboratory conditions make academic research much more straightforward, while industrial manufacturing requires additional factors like instrument stability, process consistency, and scaling up experiments. Although Cu/S-based electrocatalysts have advanced significantly in terms of practical uses, there is still more work to be done before vast commercial applications. Therefore, reducing the gap between lab-scale research and industrial applications is crucial for Cu/S-based electrocatalysts.

Author contributions

A. M. conducted the literature search, wrote the final manuscript, and created figures and tables. MA, SSM, and BCR supervised and revised the manuscript. All authors were involved in the discussion and critical revision, and the final version of the manuscript was approved.

Data availability

No primary research results, software or codes have been included and no new data have been generated or analysed as part of this review.

Conflicts of interest

The authors declare no conflict of interest.

Acknowledgements

The authors gratefully acknowledge the Birla Institute of Technology, Mesra, for providing the institute research fellowship and Indian Science Technology and Engineering facilities Map (I-STEM/catalytic grant/acad_18/2022-2023) for financial support.

References

1 N. Patel and D. Mehta, *Int. J. Thermofluids*, 2023, **20**, 100397.

2 B. Doğan, M. Shahbaz, M. F. Bashir, S. Abbas and S. Ghosh, *Renewable Sustainable Energy Rev.*, 2023, **184**, 113551.

3 Y. Huang, Z. Kuldasheva, S. Bobojanov, B. Djalilov, R. Salahodjaev and S. Abbas, *Environ. Sci. Pollut. Res.*, 2023, **30**, 10854–10866.

4 L. J. R. Nunes, *Environ.*, 2023, **10**, 66.

5 E. Liu, X. Lu and D. Wang, *Energies*, 2023, **16**, 2865.

6 B. Dziejarski, R. Krzyżyńska and K. Andersson, *Fuel*, 2023, **342**, 127776.

7 N. Yusuf, F. Almomani and H. Qiblawey, *Fuel*, 2023, **345**, 128178.

8 W. Chung, W. Jeong, J. Lee, J. Kim, K. Roh and J. H. Lee, *Comput. Chem. Eng.*, 2023, **170**, 108106.

9 J.-Y. Chen, M. Li and R.-Z. Liao, *Inorg. Chem.*, 2023, **62**, 9400–9417.

10 M. Li, K. Yang, M. Abdinejad, C. Zhao and T. Burdyny, *Nanoscale*, 2022, **14**, 11892–11908.

11 G. Bhattacharya, R. Manna, P. Sardar, S. Rahut and A. N. Samanta, *Ind. Eng. Chem. Res.*, 2024, **63**(28), 12361–12372.

12 Y. Fang, Y. Liu, L. Qi, Y. Xue and Y. Li, *Chem. Soc. Rev.*, 2022, **51**, 2681–2709.

13 S. Bierbaumer, M. Nattermann, L. Schulz, R. Zschoche, T. J. Erb, C. K. Winkler, M. Tinzl and S. M. Glueck, *Chem. Rev.*, 2023, **123**, 5702–5754.

14 S. Wei, W. Liu, C. Yang, P. Bai, X. Kong, W. Sun and L. Xu, *Mater. Chem. Front.*, 2023, **7**, 4723–4743.

15 M. Abdinejad, A. Seifitokaldani, C. Dao, E. H. Sargent, X. A. Zhang and H. B. Kraatz, *ACS Appl. Energy Mater.*, 2019, **2**, 1330–1335.

16 S. Kaur, M. Kumar, D. Gupta, P. P. Mohanty, T. Das, S. Chakraborty, R. Ahuja and T. C. Nagaiah, *Nano Energy*, 2023, **109**, 108242.

17 M. Abdinejad, M. N. Hossain and H. B. Kraatz, *RSC Adv.*, 2020, **10**, 38013–38023.

18 C. He, Y. Gong, S. Li, J. Wu, Z. Lu, Q. Li, L. Wang, S. Wu and J. Zhang, *Adv. Mater.*, 2024, 2311628.

19 M. Abdinejad, T. Yuan, K. Tang, S. Duangdangchote, A. Farzi, H. P. Iglesias van Montfort, M. Li, J. Middelkoop, M. Wolff, A. Seifitokaldani, O. Voznyy and T. Burdyny, *Chem. – Eur. J.*, 2023, **29**, e202203977.

20 I. Masood ul Hasan, L. Peng, J. Mao, R. He, Y. Wang, J. Fu, N. Xu and J. Qiao, *Carbon Energy*, 2021, **3**, 24–49.

21 M. Abdinejad, I. Santos da Silva and H. B. Kraatz, *J. Mater. Chem. A*, 2021, **9**, 9791–9797.

22 M. Abdinejad, E. Irtem, A. Farzi, M. Sassenburg, S. Subramanian, H. P. Iglesias Van Montfort, D. Ripepi, M. Li, J. Middelkoop, A. Seifitokaldani and T. Burdyny, *ACS Catal.*, 2022, **12**, 7862–7876.

23 Z. Masood and Q. Ge, *Catal. Today*, 2023, **409**, 53–62.

24 Q. Cheng, M. Huang, L. Xiao, S. Mou, X. Zhao, Y. Xie, G. Jiang, X. Jiang and F. Dong, *ACS Catal.*, 2023, **13**, 4021–4029.

25 A. Mukherjee, M. Abdinejad, S. S. Mahapatra and B. C. Ruidas, *J. Mater. Chem. A*, 2023, **11**, 9300–9332.

26 M. Isegawa, *Chem. Phys.*, 2023, **565**, 111758.

27 K. Kim, P. Wagner, K. Wagner and A. J. Mozer, *Molecules*, 2023, **28**, 5179.

28 X. Song, L. Xu, X. Sun and B. Han, *Sci. China: Chem.*, 2023, **66**, 315–323.

29 M. Todoroki, K. Hara, A. Kudo and T. Sakata, *J. Electroanal. Chem.*, 1995, **394**, 199–203.

30 J. W. Jang, S. Cho, G. Magesh, Y. J. Jang, J. Y. Kim, W. Y. Kim, J. K. Seo, S. Kim, K. H. Lee and J. S. Lee, *Angew. Chem., Int. Ed.*, 2014, **53**, 5852–5857.

31 G. O. Larrazábal, A. J. Martín, S. Mitchell, R. Hauert and J. Pérez-Ramírez, *ACS Catal.*, 2016, **6**, 6265–6274.

32 B. Ávila-Bolívar, L. García-Cruz, V. Montiel and J. Solla-Gullón, *Molecules*, 2019, **24**, 2032.

33 Q. Li, J. Fu, W. Zhu, Z. Chen, B. Shen, L. Wu, Z. Xi, T. Wang, G. Lu, J. J. Zhu and S. Sun, *J. Am. Chem. Soc.*, 2017, **139**, 4290–4293.

34 S. Santra, V. Streibel, L. I. Wagner, N. Cheng, P. Ding, G. Zhou, E. Sirotti, R. Kisslinger, T. Rieth, S. Zhang and I. D. Sharp, *ChemSusChem*, 2024, **17**, e202301452.

35 W. Zhu, R. Michalsky, Ö. Metin, H. Lv, S. Guo, C. J. Wright, X. Sun, A. A. Peterson and S. Sun, *J. Am. Chem. Soc.*, 2013, **135**, 16833–16836.

36 W. Zhu, Y. J. Zhang, H. Zhang, H. Lv, Q. Li, R. Michalsky, A. A. Peterson and S. Sun, *J. Am. Chem. Soc.*, 2014, **136**, 16132–16135.

37 K. Sun, L. Wu, W. Qin, J. Zhou, Y. Hu, Z. Jiang, B. Shen and Z. Wang, *J. Mater. Chem. A*, 2016, **4**, 12616–12623.

38 R. Wang, H. Haspel, A. Pustovarenko, A. Dikhtiarenko, A. Russkikh, G. Shterk, D. Osadchii, S. Ould-Chikh, M. Ma, W. A. Smith, K. Takanabe, F. Kapteijn and J. Gascon, *ACS Energy Lett.*, 2019, **4**, 2024–2031.

39 D. H. Won, H. Shin, J. Koh, J. Chung, H. S. Lee, H. Kim and S. I. Woo, *Angew. Chemie*, 2016, **128**, 9443–9446.

40 W. Luo, J. Zhang, M. Li and A. Züttel, *ACS Catal.*, 2019, **9**, 3783–3791.

41 A. Klinkova, P. De Luna, C. T. Dinh, O. Voznyy, E. M. Larin, E. Kumacheva and E. H. Sargent, *ACS Catal.*, 2016, **6**, 8115–8120.

42 J. Zeng, W. Zhang, Y. Yang, D. Li, X. Yu and Q. Gao, *ACS Appl. Mater. Interfaces*, 2019, **11**, 33074–33081.

43 F. A. Hanc-Scherer, M. A. Montiel, V. Montiel, E. Herrero and C. M. Sánchez-Sánchez, *Phys. Chem. Chem. Phys.*, 2015, **17**, 23909–23916.

44 M. Umeda, Y. Niitsuma, T. Horikawa, S. Matsuda and M. Osawa, *ACS Appl. Energy Mater.*, 2020, **3**, 1119–1127.

45 J. Yin, J. Jin, Z. Yin, L. Zhu, X. Du, Y. Peng, P. Xi, C. H. Yan and S. Sun, *Nat. Commun.*, 2023, **14**, 1–10.

46 S. Pérez-Rodríguez, G. García, L. Calvillo, V. Celorrio, E. Pastor and M. J. Lázaro, *Int. J. Electrochem.*, 2011, **2011**, 1–13.

47 H. Bin Yang, S. F. Hung, S. Liu, K. Yuan, S. Miao, L. Zhang, X. Huang, H. Y. Wang, W. Cai, R. Chen, J. Gao, X. Yang, W. Chen, Y. Huang, H. M. Chen, C. M. Li, T. Zhang and B. Liu, *Nat. Energy*, 2018, **3**, 140–147.

48 J. Han, B. Tu, P. An, J. Zhang, Z. Yan, X. Zhang, C. Long, Y. Zhu, Y. Yuan, X. Qiu, Z. Yang, X. Huang, S. Yan and Z. Tang, *Adv. Mater.*, 2024, **36**, 2313926.

49 R. Chen, X. Zu, J. Zhu, Y. Zhao, Y. Li, Z. Hu, S. Wang, M. Fan, S. Zhu, H. Zhang, B. Ye, Y. Sun and Y. Xie, *Adv. Mater.*, 2024, **36**, 2314209.

50 Y. Hori, *Mod. Asp. Electrochem.*, 2008, 89–189.
51 C. Kong, G. Jiang, Y. Sheng, Y. H. Liu, F. Gao, F. Liu and X. Duan, *Chem. Eng. J.*, 2023, **460**, 141803.
52 M. Li and J. N. Zhang, *Sci. China: Chem.*, 2023, **66**, 1288–1317.
53 J. Yan, H. Ma, J. Ni, J. Ma, J. Xu, J. Qi, S. Zhu and L. Lu, *J. Colloid Interface Sci.*, 2023, **648**, 558–566.
54 Q. Zhao, J. M. P. Martirez and E. A. Carter, *J. Am. Chem. Soc.*, 2021, **143**(16), 6152–6164.
55 J. Zhang, C. Guo, S. Fang, X. Zhao, L. Li, H. Jiang, Z. Liu, Z. Fan, W. Xu, J. Xiao and M. Zhong, *Nat. Commun.*, 2023, **14**, 1–11.
56 M. Ding, Z. Chen, C. Liu, Y. Wang, C. Li, X. Li, T. Zheng, Q. Jiang and C. Xia, *Mater. Rep. Energy*, 2023, **3**, 100175.
57 D. Song, Y. Lian, M. Wang, Y. Su, F. Lyu, Z. Deng and Y. Peng, *eScience*, 2023, **3**, 100097.
58 M. Abdinejad, S. Subramanian, K. Motlagh, M. Noroozifar, S. Duangdangchote, I. Neporozhnii, D. Ripepi, D. Pinto, M. Li, K. Tang, J. Middelkoop, A. Urakawa, O. Voznyy, H.-B. Kraatz, T. Burdyny, M. Abdinejad, S. Subramanian, D. Ripepi, D. Pinto, M. Li, J. Middelkoop, A. Urakawa, T. Burdyny, M. K. Motlagh, M. Noroozifar, S. Duangdangchote, I. Neporozhnii, K. Tang, O. Voznyy and H.-B. Kraatz, *Adv. Energy Mater.*, 2023, **13**, 2300402.
59 S. Nitopi, E. Bertheussen, S. B. Scott, X. Liu, A. K. Engstfeld, S. Horch, B. Seger, I. E. L. Stephens, K. Chan, C. Hahn, J. K. Nørskov, T. F. Jaramillo and I. Chorkendorff, *Chem. Rev.*, 2019, **119**, 7610–7672.
60 M. Li, Y. Hu, T. Wu, A. Sumboja and D. Geng, *Mater. Today*, 2023, **67**, 320–343.
61 K. Yang, Y. Sun, S. Chen, M. Li, M. Zheng, L. Ma, W. Fan, Y. Zheng, Q. Li and J. Duan, *Small*, 2023, **19**, 2301536.
62 Y. Hori, H. Wakebe, T. Tsukamoto and O. Koga, *Surf. Sci.*, 1995, **335**, 258–263.
63 Y. Hori, I. Takahashi, O. Koga and N. Hoshi, *J. Mol. Catal. A: Chem.*, 2003, **199**, 39–47.
64 R. Reske, H. Mistry, F. Behafarid, B. Roldan Cuenya and P. Strasser, *J. Am. Chem. Soc.*, 2014, **136**, 6978–6986.
65 J. Chen, S. K. Iyemperumal, T. Fenton, A. Carl, R. Grimm, G. Li and N. A. Deskins, *ACS Catal.*, 2018, **8**, 10464–10478.
66 W. Tang, A. A. Peterson, A. S. Varela, Z. P. Jovanov, L. Bech, W. J. Durand, S. Dahl, J. K. Nørskov and I. Chorkendorff, *Phys. Chem. Chem. Phys.*, 2011, **14**, 76–81.
67 Z. Lyu, S. Zhu, M. Xie, Y. Zhang, Z. Chen, R. Chen, M. Tian, M. Chi, M. Shao and Y. Xia, *Angew. Chem., Int. Ed.*, 2021, **60**, 1909–1915.
68 Y. Wang, C. Niu, Y. Zhu, D. He and W. Huang, *ACS Appl. Energy Mater.*, 2020, **3**, 9841–9847.
69 T. T. H. Hoang, S. Ma, J. I. Gold, P. J. A. Kenis and A. A. Gewirth, *ACS Catal.*, 2017, **7**, 3313–3321.
70 A. S. Malkani, M. Dunwell and B. Xu, *ACS Catal.*, 2019, **9**(1), 474–478.
71 R. M. Arán-Ais, R. Rizo, P. Grosse, G. Algara-Siller, K. Dembélé, M. Plodinec, T. Lunkenbein, S. W. Chee and B. Roldan Cuenya, *Nat. Commun.*, 2020, **11**, 1–8.
72 J. Shen, L. Wang, X. He, S. Wang, J. Chen, J. Wang and H. Jin, *ChemSusChem*, 2022, **15**, e202201350.
73 L. Wan, X. Zhang, J. Cheng, R. Chen, L. Wu, J. Shi and J. Luo, *ACS Catal.*, 2022, **12**, 2741–2748.
74 D. Majumdar, *J. Electroanal. Chem.*, 2021, **880**, 114825.
75 K. Samdhyan, P. Chand, H. Anand and S. Saini, *J. Energy Storage*, 2022, **46**, 103886.
76 Y. Xie, A. Riedinger, M. Prato, A. Casu, A. Genovese, P. Guardia, S. Sottini, C. Sangregorio, K. Miszta, S. Ghosh, T. Pellegrino and L. Manna, *J. Am. Chem. Soc.*, 2013, **135**, 17630–17637.
77 R. J. Goble, *Can. Mineral.*, 1985, **23**, 6–76.
78 G. Kalimuldina, A. Nurpeissova, A. Adylkhanova, D. Adair, I. Taniguchi and Z. Bakenov, *ACS Appl. Energy Mater.*, 2020, **3**, 11480–11499.
79 P. Roy and S. K. Srivastava, *CrystEngComm*, 2015, **17**, 7801–7815.
80 F. di Benedetto, M. Borgheresi, A. Caneschi, G. Chastanet, C. Cipriani, D. Gatteschi, G. Pratesi, M. Romanelli and R. Sessoli, *Eur. J. Mineral.*, 2006, **18**, 283–287.
81 R. Zeinodin, F. Jamali-Sheini and M. Cheraghizade, *Mater. Sci. Semicond. Process.*, 2021, **123**, 105501.
82 Z. Song, Y. Liu, B. Zhang, S. Song, Z. Zhou, Y. Huang and Z. Zhao, *New J. Chem.*, 2023, **47**, 2286–2295.
83 J. Tirado, C. Roldán-Carmona, F. A. Muñoz-Guerrero, G. Bonilla-Arboleda, M. Ralaiarisoa, G. Grancini, V. I. E. Queloz, N. Koch, M. K. Nazeeruddin and F. Jaramillo, *Appl. Surf. Sci.*, 2019, **478**, 607–614.
84 P. Tetyana, N. Mphuthi, A. N. Jijana, N. Moloto, P. M. Shumbula, A. Skepu, L. S. Vilakazi and L. Sikhwivhilu, *Nanomaterials*, 2023, **13**, 481.
85 E. M. Mkawi, M. W. Iqbal, Y. Al-Hadeethi, H. Hassan, B. Arkook, F. G. ALmehmadi and J. O. Dennis, *J. Energy Storage*, 2023, **67**, 107656.
86 J. He, K. Ramachandraiah, T. Huang, T. Yuan, X. Liu, H. Zhang and F. Ke, *Biochem. Biophys. Res. Commun.*, 2023, **638**, 51–57.
87 S. Chandrasekaran, L. Yao, L. Deng, C. Bowen, Y. Zhang, S. Chen, Z. Lin, F. Peng and P. Zhang, *Chem. Soc. Rev.*, 2019, **48**, 4178–4280.
88 O. C. Pore, A. V. Fulari, C. D. Chavare, D. S. Sawant, S. S. Patil, R. V. Shejwal, V. J. Fulari and G. M. Lohar, *Chem. Phys. Lett.*, 2023, **824**, 140551.
89 S. K. Godlaveeti, A. R. Somala and R. R. Nagireddy, *Appl. Phys. A: Mater. Sci. Process.*, 2023, **129**, 1–12.
90 N. Badar, H. M. Yusoff, K. Elong and N. Kamarulzaman, *Adv. Powder Technol.*, 2023, **34**, 104102.
91 H. Bian, R. Wang, K. Zhang, H. Zheng, M. Wen, Z. Li, Z. Li, G. Wang, G. Xie, X. Liu and L. Jiang, *Surf. Coatings Technol.*, 2023, **459**, 129407.
92 E. Aboobakri, T. Heidari and M. Jahani, *Carbon Lett.*, 2023, **33**, 1629–1638.
93 M. H. Patel, T. K. Chaudhuri and V. K. Patel, *J. Mater. Sci.: Mater. Electron.*, 2023, **34**, 1–9.
94 E. Gribov, E. Koshevoy, I. Chikunova and V. Parmon, *Catalysts*, 2023, **13**, 168.
95 T. Singh and V. Mutreja, *AIP Conf. Proc.*, 2023, **2535**(1), 060002.

96 Y. Chen, K. Chen, J. Fu, A. Yamaguchi, H. Li, H. Pan, J. Hu, M. Miyauchi and M. Liu, *Nano Mater. Sci.*, 2020, **2**, 235–247.

97 Y. Tian, B. Li, J. Wang, Y. Ge, W. Gao, L. Yu, L. Ma, Y. Li, L. Wang, Z. Liu and J. Chen, *Chem. Eng. J.*, 2024, **490**, 151704.

98 C. Ye, B. Liu, Q. Li, M. Yu, Y. Liu, Z. Tai, Z. Pan and Y. Qiu, *Small*, 2024, **20**, 2309856.

99 X. Ma, Y. Zhang, T. Fan, D. Wei, Z. Huang, Z. Zhang, Z. Zhang, Z. Zhang, Y. Dong, Q. Hong, Z. Chen and X. Yi, *Adv. Funct. Mater.*, 2023, **33**, 2213145.

100 C. He, D. Duan, J. Low, Y. Bai, Y. Jiang, X. Wang, S. Chen, R. Long, L. Song and Y. Xiong, *Nano Res.*, 2023, **16**, 4494–4498.

101 T. Dou, Y. Qin, F. Zhang and X. Lei, *ACS Appl. Energy Mater.*, 2021, **4**, 4376–4384.

102 G. Janani, S. Surendran, D. K. Lee, S. Shanmugapriya, H. Lee, Y. Subramanian and U. Sim, *Aggregate*, 2024, **5**, e430.

103 C. Zhou, Y. Wu, X. Zhang, C. Ye, G. Peng and W. Yuan, *J. Nanoparticle Res.*, 2024, **26**, 1–11.

104 P. Shao, S. Ci, L. Yi, P. Cai, P. Huang, C. Cao and Z. Wen, *ChemElectroChem*, 2017, **4**, 2593–2598.

105 L. Zhang, X. Shi, A. Xu, W. Zhong, J. Zhang and S. Shen, *Nano Res.*, 2024, **17**, 3693–3699.

106 M. Ravipati and S. Badhulika, *ACS Appl. Nano Mater.*, 2024, **7**, 7277–7288.

107 L. Meng, C. W. Kao, Z. Wang, J. Ma, P. Huang, N. Zhao, X. Zheng, M. Peng, Y. R. Lu and Y. Tan, *Nat. Commun.*, 2024, **15**, 1–10.

108 W. Zhu, L. Fan, Q. Geng, C. Wang, X. Fan, Y. Zhang and C. Li, *Chem. Eng. J.*, 2024, **489**, 151316.

109 A. Yabuki, Y. Iwamura, T. Tachibana and J. H. Lee, *New J. Chem.*, 2022, **46**, 19633–19637.

110 Z. Zhao, X. Peng, X. Liu, X. Sun, J. Shi, L. Han, G. Li and J. Luo, *J. Mater. Chem. A*, 2017, **5**, 20239–20243.

111 Q. G. Zhu, X. F. Sun, X. C. Kang, J. Ma, Q. L. Qian and B. X. Han, *Wuli Huaxue Xuebao*, 2016, **32**, 261–266.

112 Z. Kou, X. Li, L. Zhang, W. Zang, X. Gao and J. Wang, *Small Sci.*, 2021, **1**, 2100011.

113 C. Yan, J. Huang, C. Wu, Y. Li, Y. Tan, L. Zhang, Y. Sun, X. Huang and J. Xiong, *J. Mater. Sci. Technol.*, 2020, **42**, 10–16.

114 C. Kim, S. H. Kim, S. Lee, I. Kwon, S. Kim, C. Seok, Y. S. Park and Y. Kim, *J. Energy Chem.*, 2022, **64**, 364–371.

115 K. Fan, H. Zou, Y. Lu, H. Chen, F. Li, J. Liu, L. Sun, L. Tong, M. F. Toney, M. Sui and J. Yu, *ACS Nano*, 2018, **12**, 12369–12379.

116 T. X. Nguyen, Y. H. Su, C. C. Lin and J. M. Ting, *Adv. Funct. Mater.*, 2021, **31**, 2106229.

117 J. Chen, Y. Tu, Y. Zou, X. Li and J. Jiang, *Mater. Lett.*, 2021, **284**, 128919.

118 K. R. Phillips, Y. Katayama, J. Hwang and Y. Shao-Horn, *J. Phys. Chem. Lett.*, 2018, **9**, 4407–4412.

119 B. Zhang, M. Wang, J. Ding, Y. Li, G. Cao, M. T. Bernards, Y. He and Y. Shi, *J. CO2 Util.*, 2020, **39**, 101169.

120 C. H. M. van Oversteeg, M. Tapia Rosales, K. H. Helfferich, M. Ghiasi, J. D. Meeldijk, N. J. Firet, P. Ngene, C. de Mello Donegá and P. E. de Jongh, *Catal. Today*, 2021, **377**, 157–165.

121 Y. Gao, Y. Guo, Y. Zou, W. Liu, Y. Luo, B. Liu and C. Zhao, *ACS Appl. Energy Mater.*, 2023, **6**, 1340–1354.

122 W. He, I. Liberman, I. Rozenberg, R. Ifraemov and I. Hod, *Angew. Chem., Int. Ed.*, 2020, **59**, 8262–8269.

123 J. Li, J. Li, C. Dun, W. Chen, D. Zhang, J. Gu, J. J. Urban and J. W. Ager, *RSC Adv.*, 2021, **11**, 23948–23959.

124 D. Y. Y. Goh, K. M. Yam, L. Rekhi, A. D. Handoko, Y. C. Tan, Y. Wang, J. M. R. Tan, T. S. Choksi, Y. Lum and L. H. Wong, *J. Mater. Chem. A*, 2024, **12**, 1840–1851.

125 E. Cui, W. Zhang, X. Zhou, L. Lv, W. Chen, L. Zhou and L. Mai, *ACS Appl. Nano Mater.*, 2023, **6**, 9361–9368.

126 X. Zhang, Y. Zhang, X. Wei, C. Wei and Y. Song, *Nanoscale Adv.*, 2021, **3**, 5777–5784.

127 T. Wu, M. Y. Han and Z. J. Xu, *ACS Nano*, 2022, **16**, 8531–8539.

128 T. Shinagawa, G. O. Larrazábal, A. J. Martín, F. Krumeich and J. Pérez-Ramírez, *ACS Catal.*, 2018, **8**, 837–844.

129 J. W. Lim, W. J. Dong, J. Y. Park, D. M. Hong and J. L. Lee, *ACS Appl. Mater. Interfaces*, 2020, **12**, 22891–22900.

130 H. K. Park, H. Ahn, T. H. Lee, J. Y. Lee, M. G. Lee, S. A. Lee, J. W. Yang, S. J. Kim, S. H. Ahn, S. Y. Kim, C. H. Lee, E. S. Park and H. W. Jang, *Small Methods*, 2021, **5**, 2000755.

131 X. Zhong, E. Yuan, F. Yang, Y. Liu, H. Lu, J. Yang, F. Gao, Y. Zhou, J. Pan, J. Zhu, C. Yu, C. Zhu, A. Yuan and E. H. Ang, *Proc. Natl. Acad. Sci. U. S. A.*, 2023, **120**, e2306673120.

132 X. Xu, Y. Zhong, M. Wajrak, T. Bhatelia, S. P. Jiang and Z. Shao, *InfoMat*, 2024, e12608.

133 R. Zhang, L. Wang, Y. H. Ma, L. Pan, R. Gao, K. Li, X. Zhang and J. J. Zou, *J. Mater. Chem. A*, 2019, **7**, 10010–10018.

134 R. Yang, X. Zheng, H. Fu, X. Cao, Y. Hu and Y. Huang, *ChemSusChem*, 2024, **17**, e202301771.

135 Y. Wang, H. Xu, Y. Liu, J. Jang, X. Qiu, E. P. Delmo, Q. Zhao, P. Gao and M. Shao, *Angew. Chem., Int. Ed.*, 2024, **63**, e202313858.

136 K. Wu, C. Lyu, J. Cheng, W. Ding, J. Wu, Q. Wang, W. M. Lau and J. Zheng, *Carbon Energy*, 2024, **6**, e485.

137 Y. Wang, Z. Lu, S. Wu, Z. Zou, X. Zhang and Y. Wang, *J. Environ. Chem. Eng.*, 2024, **12**, 112839.

138 Y. Liu, Z. Yang, Y. Zou, S. Wang and J. He, *Energy Environ. Mater.*, 2024, **7**, e12576.

139 J. Liang, S. Li, F. Li, L. Zhang, Y. Jiang, H. Ma, K. Cheng and L. Qing, *J. Colloid Interface Sci.*, 2024, **655**, 296–306.

140 L. Hong, B. Li, C. Jing, Z. Zhuang, Y. Zhang, H. Huang, Q. Jiang and J. Tang, *J. Environ. Chem. Eng.*, 2024, **12**, 111946.

141 Z. Guo, M. Bi, H. He, Z. Liu, Y. Duan and W. Cao, *J. Colloid Interface Sci.*, 2024, **654**, 785–794.

142 T. T. Zhuang, Z. Q. Liang, A. Seifitokaldani, Y. Li, P. De Luna, T. Burdyny, F. Che, F. Meng, Y. Min, R. Quintero-Bermudez, C. T. Dinh, Y. Pang, M. Zhong, B. Zhang, J. Li, P. N. Chen, X. L. Zheng, H. Liang, W. N. Ge, B. J. Ye,

D. Sinton, S. H. Yu and E. H. Sargent, *Nat. Catal.*, 2018, **1**, 421–428.

143 C. Peng, G. Luo, J. Zhang, M. Chen, Z. Wang, T. K. Sham, L. Zhang, Y. Li and G. Zheng, *Nat. Commun.*, 2021, **12**, 1–8.

144 R. He, X. Huang and L. Feng, *Energy Fuels*, 2022, **36**, 6675–6694.

145 M. Li and L. Feng, *Chin. J. Struct. Chem.*, 2022, **41**, 2201019–2201024.

146 H. Liu, D. Zhao, P. Hu, K. Chen, X. Wu and D. Xue, *Mater. Today Phys.*, 2020, **13**, 100197.

147 S. Zhang, C. Tan, R. Yan, X. Zou, F. L. Hu, Y. Mi, C. Yan and S. Zhao, *Angew. Chem., Int. Ed.*, 2023, **62**, e202302795.

148 H. Tao, T. Jia, L. Zhang, X. Li, P. Li, Y. Zhou and C. Zhai, *J. Colloid Interface Sci.*, 2024, **655**, 909–919.

149 T. Dou, J. He, S. Diao, Y. Wang, X. Zhao, F. Zhang and X. Lei, *J. Energy Chem.*, 2023, **82**, 497–506.

150 X. Wang, J. Lv, J. Zhang, X. L. Wang, C. Xue, G. Bian, D. Li, Y. Wang and T. Wu, *Nanoscale*, 2020, **12**, 772–784.

151 Y. Liu, Z. Jiang, C. Huang, S. Jeong, A. L. Coughlin, S. Zhang, Y. Liu and X. Ye, *Nano Lett.*, 2023, **23**, 5911–5918.

152 C. He, S. Chen, R. Long, L. Song and Y. Xiong, *Sci. China: Chem.*, 2020, **63**, 1721–1726.

153 S. Cao, Y. Xue, X. Chen, C. Zhang, Y. Gao and Y. Li, *Mater. Chem. Front.*, 2023, **7**, 2620–2627.

154 C. F. Wen, M. Zhou, P. F. Liu, Y. Liu, X. Wu, F. Mao, S. Dai, B. Xu, X. L. Wang, Z. Jiang, P. Hu, S. Yang, H. F. Wang and H. G. Yang, *Angew. Chemie*, 2022, **134**, e202111700.

155 Y. Li, Y. Chen, T. Chen, G. Shi, L. Zhu, Y. Sun and M. Yu, *ACS Appl. Mater. Interfaces*, 2023, **15**, 18857–18866.

156 V. S. S. Mosali, G. Puxty, M. D. Horne, A. M. Bond and J. Zhang, *Electrochim. Acta*, 2024, **475**, 143628.

157 V. S. S. Mosali, X. Zhang, Y. Liang, L. Li, G. Puxty, M. D. Horne, A. Brajter-Toth, A. M. Bond and J. Zhang, *ChemSusChem*, 2021, **14**, 2924–2934.

158 Z. Yang, D. Ji, Z. Li, Z. He, Y. Hu, J. Yin, Y. Hou, P. Xi and C. H. Yan, *Small*, 2023, **19**, 2303099.

159 Q. Wang, T. Bao, X. Zhao, Y. Cao, J. Cao, Q. Li and W. Si, *Molecules*, 2024, **29**, 2948.

160 X. Han, T. Mou, S. Liu, M. Ji, Q. Gao, Q. He, H. Xin and H. Zhu, *Nanoscale Horiz.*, 2022, **7**, 508–514.

161 M. Prasanna, N. Logeshwaran, S. Ramakrishnan and D. J. Yoo, *Small*, 2024, **20**, 2306165.

162 Y. Guo, Y. Gao, B. Guo, Y. Luo, G. Zhao, J. Sun, W. Li, R. Wang and C. Zhao, *Carbon Neutrality*, 2024, **3**, 1–20.

163 Y. Wang, Y. Wang, J. Zhao, T. Tang, B. Lv, Y. Chang, T. Hu, J. Zhang, E. Luo and J. Jia, *ACS Sustainable Chem. Eng.*, 2024, **12**, 6982–6989.

164 Y. Zhang, Y. Dong, X. Yan, H. Peng, S. Xu, M. Zhu, Z. Jin, L. Han and J. Zhang, *J. Energy Storage*, 2024, **84**, 111023.

165 X. Cheng, D. Wu, H. Xu and W. Zhang, *J. Phys. Chem. C*, 2024, **128**, 12101–12108.

166 W. Cheng, H. Yang, T. Wang, X. He, L. Tian and Z. Li, *Chem. Rec.*, 2024, **24**, e202300088.

167 Y. Jia, Y. Zhang, H. Xu, J. Li, M. Gao and X. Yang, *ACS Catal.*, 2024, **14**, 4601–4637.

168 P. Xu, Z. Bao, Y. Zhao, L. Zheng, Z. Lv, X. Shi, H. E. Wang, X. Fang and H. Zheng, *Adv. Energy Mater.*, 2024, **14**, 2303557.

169 Y. Hu, J. Zhu, X. Wang, X. Zheng, X. Zhang, C. Wu, J. Zhang, C. Fu, T. Sheng and Z. Wu, *Inorg. Chem.*, 2024, **63**, 9983–9991.

170 H. Shen, Y. Zhao, L. Zhang, Y. He, S. Yang, T. Wang, Y. Cao, Y. Guo, Q. Zhang and H. Zhang, *Adv. Energy Mater.*, 2023, **13**, 2202818.

171 L. Liang, L. Yang, T. Heine, A. Arinchtein, X. Wang, J. Hübner, J. Schmidt, A. Thomas and P. Strasser, *Adv. Energy Mater.*, 2024, **14**, 2304224.

172 S. Li, H. Duan, J. Yu, C. Qiu, R. Yu, Y. Chen, Y. Fang, X. Cai and S. Yang, *ACS Catal.*, 2022, **12**, 9074–9082.

173 Y. Huang, Y. Deng, A. D. Handoko, G. K. L. Goh and B. S. Yeo, *ChemSusChem*, 2018, **11**, 320–326.

174 T. Jia, L. Wang, L. Zhang, Z. Zhu, K. Zhang, B. Zhu, X. Li, C. Zhai, S. Li, Y. Zhou and H. Tao, *Surf. Interfaces*, 2023, **38**, 102841.

175 H. Yuan, Z. Liu, S. Sang and X. Wang, *Appl. Surf. Sci.*, 2023, **613**, 156130.

176 X. Zhang, R. Sa, F. Zhou, Y. Rui, R. Liu, Z. Wen and R. Wang, *CCS Chem.*, 2021, **3**, 199–207.

177 Y. Deng, Y. Huang, D. Ren, A. D. Handoko, Z. W. Seh, P. Hirunsit and B. S. Yeo, *ACS Appl. Mater. Interfaces*, 2018, **10**, 28572–28581.

178 E. Meza, R. E. Diaz and C. W. Li, *ACS Nano*, 2020, **14**, 2238–2247.

179 P. Vancsó, Z. I. Popov, J. Petö, T. Ollár, G. Dobrik, J. S. Pap, C. Hwang, P. B. Sorokin and L. Tapasztó, *ACS Energy Lett.*, 2019, **4**, 1947–1953.

180 Y. Liu, Y. Guo, Y. Liu, Z. Wei, K. Wang and Z. Shi, *Energy Fuels*, 2023, **37**, 2608–2630.

181 H. Wang, T. Yang, J. Wang, Z. Zhou, Z. Pei and S. Zhao, *Chem*, 2024, **10**, 48–85.

182 A. W. Kahsay, K. B. Ibrahim, M. C. Tsai, M. K. Birhanu, S. A. Chala, W. N. Su and B. J. Hwang, *Catal. Lett.*, 2019, **149**, 860–869.

183 S. Wang, T. Kou, J. B. Varley, S. A. Akhade, S. E. Weitzner, S. E. Baker, E. B. Duoss and Y. Li, *ACS Mater. Lett.*, 2021, **3**, 100–109.

184 J. Wang, M. G. Sandoval, M. Couillard, E. A. González, P. V. Jasen, A. Juan, A. Weck and E. A. Baranova, *ACS Sustainable Chem. Eng.*, 2024, **12**(29), 11044–11055.

185 N. K. Singh, P. Kumar, A. Yadav and V. C. Srivastava, *J. Colloid Interface Sci.*, 2024, **654**, 895–905.

186 X. Li, L. Jiang, Y. Zhou and Q. Yu, *Langmuir*, 2024, **40**(30), 15580–15587.

187 H. A. B. Fonseca, L. G. Verga and J. L. F. Da Silva, *J. Phys. Chem. C*, 2023, **127**, 24118–24128.

188 D. Liu, Y. Liu and M. Li, *J. Phys. Chem. C*, 2020, **124**, 6145–6153.

189 C. L. Dong and L. Vayssieres, *Chem. – Eur. J.*, 2018, **24**, 18356–18373.

190 K. T. Butler, D. W. Davies, H. Cartwright, O. Isayev and A. Walsh, *Nat.*, 2018, **559**, 547–555.

191 A. Chandrasekaran, D. Kamal, R. Batra, C. Kim, L. Chen and R. Ramprasad, *npj Comput. Mater.*, 2019, **5**, 1–7.

192 P. Wang, H. Yang, C. Tang, Y. Wu, Y. Zheng, T. Cheng, K. Davey, X. Huang and S. Z. Qiao, *Nat. Commun.*, 2022, **13**, 1–11.

193 R. Dorakhan, I. Grigioni, B. H. Lee, P. Ou, J. Abed, C. O'Brien, A. Sedighian Rasouli, M. Plodinec, R. K. Miao, E. Shirzadi, J. Wicks, S. Park, G. Lee, J. Zhang, D. Sinton and E. H. Sargent, *Nat. Synth.*, 2023, **2**, 448–457.

194 Y. Mi, S. Shen, X. Peng, H. Bao, X. Liu and J. Luo, *ChemElectroChem*, 2019, **6**, 2393–2397.

195 L. R. L. Ting, R. García-Muelas, A. J. Martín, F. L. P. Veenstra, S. T.-J. Chen, Y. Peng, E. Y. X. Per, S. Pablo-García, N. López, J. Pérez-Ramírez and B. S. Yeo, *Angew. Chemie*, 2020, **132**, 21258–21265.

196 L. J. Zhu, D. H. Si, F. X. Ma, M. J. Sun, T. Zhang and R. Cao, *ACS Catal.*, 2023, **13**, 5114–5121.

197 M. Wang, Q. Zhang, Q. Xie, L. Wan, Y. Zhao, X. Zhang and J. Luo, *Nanoscale*, 2020, **12**, 17013–17019.

198 D. Ren, Y. Deng, A. D. Handoko, C. S. Chen, S. Malkhandi and B. S. Yeo, *ACS Catal.*, 2015, **5**, 2814–2821.

199 W. Zhang, C. Huang, Q. Xiao, L. Yu, L. Shuai, P. An, J. Zhang, M. Qiu, Z. Ren and Y. Yu, *J. Am. Chem. Soc.*, 2020, **142**, 11417–11427.

200 P. De Luna, R. Quintero-Bermudez, C.-T. Dinh, M. B. Ross, O. S. Bushuyev, P. Todorović, T. Regier, S. O. Kelley, P. Yang and E. H. Sargent, *Nat. Catal.*, 2018, **1**, 103–110.

201 G. Shi, L. Yu, X. Ba, X. Zhang, J. Zhou and Y. Yu, *Dalton Trans.*, 2017, **46**, 10569–10577.

202 S. Piontek, K. Junge Puring, D. Siegmund, M. Smialkowski, I. Sinev, D. Tetzlaff, B. Roldan Cuenya and U. P. Apfel, *Chem. Sci.*, 2019, **10**, 1075–1081.

203 K. Zhao, X. Nie, H. Wang, S. Chen, X. Quan, H. Yu, W. Choi, G. Zhang, B. Kim and J. G. Chen, *Nat. Commun.*, 2020, **11**, 1–10.

204 W. Fang, R. Lu, F. M. Li, C. He, D. Wu, K. Yue, Y. Mao, W. Guo, B. You, F. Song, T. Yao, Z. Wang and B. Y. Xia, *Angew. Chem., Int. Ed.*, 2024, **63**, e202319936.

205 Y. S. Cheng, X. P. Chu, M. Ling, N. Li, K. L. Wu, F. H. Wu, H. Li, G. Yuan and X. W. Wei, *Catal. Sci. Technol.*, 2019, **9**, 5668–5675.

206 H. Ning, X. Wang, W. Wang, Q. Mao, Z. Yang, Q. Zhao, Y. Song and M. Wu, *Carbon N. Y.*, 2019, **146**, 218–223.

207 D. Karapinar, N. T. Huan, N. Ranjbar Sahraie, J. Li, D. Wakerley, N. Touati, S. Zanna, D. Taverna, L. H. Galvão Tizei, A. Zitolo, F. Jaouen, V. Mougel and M. Fontecave, *Angew. Chem., Int. Ed.*, 2019, **58**, 15098–15103.

208 M. Wang, Z. Cai, B. Zhang, K. Yang, T. Shou, M. T. Bernards, P. Xie, Y. He and Y. Shi, *Energy Fuels*, 2022, **36**, 5833–5842.

209 A. F. Pérez-Cadenas, C. H. Ros, S. Morales-Torres, M. Pérez-Cadenas, P. J. Kooyman, C. Moreno-Castilla and F. Kapteijn, *Carbon N. Y.*, 2013, **56**, 324–331.

210 S. Dongare, N. Singh and H. Bhunia, *J. CO2 Util.*, 2021, **44**, 101382.

211 J. Yuan, W. Y. Zhi, L. Liu, M. P. Yang, H. Wang and J. X. Lu, *Electrochim. Acta*, 2018, **282**, 694–701.

212 F. Yang, X. Mao, M. Ma, C. Jiang, P. Zhang, J. Wang, Q. Deng, Z. Zeng and S. Deng, *Carbon*, 2020, **168**, 528–535.

213 X. Tan, C. Yu, C. Zhao, H. Huang, X. Yao, X. Han, W. Guo, S. Cui, H. Huang and J. Qiu, *ACS Appl. Mater. Interfaces*, 2019, **11**, 9904–9910.

214 X. F. Qiu, H. L. Zhu, J. R. Huang, P. Q. Liao and X. M. Chen, *J. Am. Chem. Soc.*, 2021, **143**, 7242–7246.

215 X. Ma, J. Tian, M. Wang, X. Jin, M. Shen and L. Zhang, *Catal. Sci. Technol.*, 2021, **11**, 6096–6102.

216 J. X. Wu, S. Z. Hou, X. Da Zhang, M. Xu, H. F. Yang, P. S. Cao and Z. Y. Gu, *Chem. Sci.*, 2019, **10**, 2199–2205.

217 Z. H. Zhao, K. Zheng, N. Y. Huang, H. L. Zhu, J. R. Huang, P. Q. Liao and X. M. Chen, *Chem. Commun.*, 2021, **57**, 12764–12767.

218 S. Juntrapirom, J. Santatiwongchai, A. Watwiangkham, S. Suthirakun, T. Butburee, K. Faungnawakij, P. Chakthranont, P. Hirunsit and B. Rungtaweevoranit, *Catal. Sci. Technol.*, 2021, **11**, 8065–8078.

219 K. Yao, Y. Xia, J. Li, N. Wang, J. Han, C. Gao, M. Han, G. Shen, Y. Liu, A. Seifitokaldani, X. Sun and H. Liang, *J. Mater. Chem. A*, 2020, **8**, 11117–11123.

220 Y. Zhao, C. Wang and G. G. Wallace, *J. Mater. Chem. A*, 2016, **4**, 10710–10718.

221 X. Ren, X. Zhang, X. Cao and Q. Wang, *J. CO2 Util.*, 2020, **38**, 125–131.

222 J. Zeng, T. Rino, K. Bejtka, M. Castellino, A. Sacco, M. A. Farkhondehfal, A. Chiodoni, F. Drago and C. F. Pirri, *ChemSusChem*, 2020, **13**, 4128–4139.

223 C. S. Chen, J. H. Wan and B. S. Yeo, *J. Phys. Chem. C*, 2015, **119**, 26875–26882.

224 A. D. Handoko, C. W. Ong, Y. Huang, Z. G. Lee, L. Lin, G. B. Panetti and B. S. Yeo, *J. Phys. Chem. C*, 2016, **120**, 20058–20067.

225 J. Kim, W. Choi, J. W. Park, C. Kim, M. Kim and H. Song, *J. Am. Chem. Soc.*, 2019, **141**, 6986–6994.

226 Y. Mun, S. Lee, A. Cho, S. Kim, J. W. Han and J. Lee, *Appl. Catal., B*, 2019, **246**, 82–88.

227 X. Guo, Y. Zhang, C. Deng, X. Li, Y. Xue, Y. M. Yan and K. Sun, *Chem. Commun.*, 2014, **51**, 1345–1348.

228 M. Serafini, F. Mariani, A. Fasolini, E. T. Brandi, E. Scavetta, F. Basile and D. Tonelli, *Adv. Funct. Mater.*, 2023, **33**, 2300345.

229 T. Gao, Y. Gu, M. Wu, Y. Liu, L. Yang, T. Han, S. Zhang, S. Li, W. Wei, W. Chen and X. Dong, *Energy Fuels*, 2023, **37**, 19053–19062.

230 A. Saxena, S. Kapila, J. E. Medvedeva and M. Nath, *ACS Appl. Mater. Interfaces*, 2023, **15**(11), 14433–14446.

231 N. Liu, S. Bartling, A. Springer, C. Kubis, O. S. Bokareva, E. Salaya, J. Sun, Z. Zhang, S. Wohlrab, A. M. Abdel-Mageed, H. Q. Liang and R. Francke, *Adv. Mater.*, 2024, **36**, 2309526.

232 A. Loiudice, P. Lobaccaro, E. A. Kamali, T. Thao, B. H. Huang, J. W. Ager and R. Buonsanti, *Angew. Chem., Int. Ed.*, 2016, **55**, 5789–5792.

233 Y. Hori, A. Murata and R. Takahashi, *J. Chem. Soc., Faraday Trans. 1*, 1989, **85**, 2309–2326.

234 C. Dong, L. Cui, Y. Kong, C. Chen, H. Liu, Y. Zhang, W. Zhu and R. He, *J. Phys. Chem. C*, 2022, **126**, 102–109.

235 Y. Wu, P. Zhai, S. Cao, Z. Li, B. Zhang, Y. Zhang, X. Nie, L. Sun and J. Hou, *Adv. Energy Mater.*, 2020, **10**, 2002499.

236 F. Gao, S. Hu, X. Zhang, Y. Zheng, H. Wang, Z. Niu, P. Yang, R. Bao, T. Ma, Z. Dang, Y. Guan, X. Zheng,

X. Zheng, J. Zhu, M. Gao and S. Yu, *Angew. Chemie*, 2020, **132**, 8784–8790.

237 R. He, A. Zhang, Y. Ding, T. Kong, Q. Xiao, H. Li, Y. Liu and J. Zeng, *Adv. Mater.*, 2018, **30**, 1705872.

238 Y. H. Li, L. Cheng, P. F. Liu, L. Zhang, M. Y. Zu, C. W. Wang, Y. H. Jin, X. M. Cao, H. G. Yang and C. Li, *ChemSusChem*, 2018, **11**, 1421–1425.

239 L. Cheng, Y. Li, A. Chen, Y. Zhu and C. Li, *Chem. Commun.*, 2020, **56**, 563–566.

240 B. Qin, Y. Li, H. Wang, G. Yang, Y. Cao, H. Yu, Q. Zhang, H. Liang and F. Peng, *Nano Energy*, 2019, **60**, 43–51.

241 Y. Wang, R. Du, Z. Li, H. Song, Z. Chao, D. Zu, D. Chong, N. Gao and C. Li, *Ceram. Int.*, 2021, **47**, 28321–28327.

242 L. Cheng, Y. Wang, Y. Li, Y. Shen, Y. Zhen, Z. Xing, L. Lin, A. Chen, Y. Zhu and C. Li, *ChemCatChem*, 2021, **13**, 1161–1164.

243 R. He, X. Yuan, P. Shao, T. Duan and W. Zhu, *Small*, 2019, **15**, 1904882.

244 A. Zhang, R. He, H. Li, Y. Chen, T. Kong, K. Li, H. Ju, J. Zhu, W. Zhu and J. Zeng, *Angew. Chem., Int. Ed.*, 2018, **57**, 10954–10958.

245 X. Zheng, P. De Luna, F. Pelayo García De Arquer, X. Du, P. Yang, E. H. Sargent, B. Zhang, N. Becknell, M. B. Ross, Y. Li, M. N. Banis, Y. Li, M. Liu, O. Voznyy, C. T. Dinh, T. Zhuang, P. Stadler and Y. Cui, *Joule*, 2017, **1**, 794–805.

246 Z. Chen, X. Zhang, M. Jiao, K. Mou, X. Zhang and L. Liu, *Adv. Energy Mater.*, 2020, **10**, 1903664.

247 F. Li, L. Chen, M. Xue, T. Williams, Y. Zhang, D. R. MacFarlane and J. Zhang, *Nano Energy*, 2017, **31**, 270–277.

248 J. He, X. Liu, H. Liu, Z. Zhao, Y. Ding and J. Luo, *J. Catal.*, 2018, **364**, 125–130.

249 H. Cheng, S. Liu, J. Zhang, T. Zhou, N. Zhang, X. S. Zheng, W. Chu, Z. Hu, C. Wu and Y. Xie, *Nano Lett.*, 2020, **20**, 6097–6103.

250 J. Xu, S. Lai, M. Hu, S. Ge, R. Xie, F. Li, D. Hua, H. Xu, H. Zhou, R. Wu, J. Fu, Y. Qiu, J. He, C. Li, H. Liu, Y. Liu, J. Sun, X. Liu and J. Luo, *Small Methods*, 2020, **4**, 2000567.

251 S. Q. Liu, M. R. Gao, R. F. Feng, L. Gong, H. Zeng and J. L. Luo, *ACS Catal.*, 2021, **11**, 7604–7612.

252 Y. Zhang, F. Li, X. Zhang, T. Williams, C. D. Easton, A. M. Bond and J. Zhang, *J. Mater. Chem. A*, 2018, **6**, 4714–4720.

253 X. Yang, P. Deng, D. Liu, S. Zhao, D. Li, H. Wu, Y. Ma, B. Y. Xia, M. Li, C. Xiao and S. Ding, *J. Mater. Chem. A*, 2020, **8**, 2472–2480.

254 X. Shao and Y. Liu, *J. Electrochem. Soc.*, 2022, **169**, 026505.

255 J. Wang, J. Mao, X. Zheng, Y. Zhou and Q. Xu, *Appl. Surf. Sci.*, 2021, **562**, 150197.

256 C. Li, Z. Liu, X. Zhou, L. Zhang, Z. Fu, Y. Wu, X. M. Lv, G. Zheng and H. Chen, *Energy Environ. Sci.*, 2023, **16**, 3885–3898.

257 Y. Li, J. Chen, S. Chen, T. Lu, X. Liao, T. Zhao, F. Cheng and H. Wang, *Appl. Catal., B*, 2024, **349**, 123874.

258 M. Asadi, B. Kumar, A. Behranginia, B. A. Rosen, A. Baskin, N. Repnin, D. Pisasale, P. Phillips, W. Zhu, R. Haasch, R. F. Klie, P. Král, J. Abiade and A. Salehi-Khojin, *Nat. Commun.*, 2014, **5**, 1–8.

259 F. Li, S. F. Zhao, L. Chen, A. Khan, D. R. MacFarlane and J. Zhang, *Energy Environ. Sci.*, 2016, **9**, 216–223.

260 K. Lv, W. Suo, M. Shao, Y. Zhu, X. Wang, J. Feng and M. Fang, *Nano Energy*, 2019, **63**, 103834.

261 N. Hussain, M. A. Abdelkareem, H. Alawadhi, K. Elsaid and A. G. Olabi, *Chem. Eng. Sci.*, 2022, **258**, 117757.

262 N. Hussain, M. A. Abdelkareem, H. Alawadhi, S. Begum, K. Elsaid and A. G. Olabi, *J. Power Sources*, 2022, **549**, 232128.

263 H. Li, X. Liu, S. Chen, D. Yang, Q. Zhang, L. Song, H. Xiao, Q. Zhang, L. Gu and X. Wang, *Adv. Energy Mater.*, 2019, **9**, 1900072.

264 P. Abbasi, M. Asadi, C. Liu, S. Sharifi-Asl, B. Sayahpour, A. Behranginia, P. Zapol, R. Shahbazian-Yassar, L. A. Curtiss and A. Salehi-Khojin, *ACS Nano*, 2017, **11**, 453–460.

265 N. Hussain, M. A. Abdelkareem, H. Alawadhi, A. H. Alami and K. Elsaid, *Appl. Phys. A: Mater. Sci. Process.*, 2022, **128**, 1–11.

266 K. Lv, C. Teng, M. Shi, Y. Yuan, Y. Zhu, J. Wang, Z. Kong, X. Lu and Y. Zhu, *Adv. Funct. Mater.*, 2018, **28**, 1802339.

267 J. Xu, X. Li, W. Liu, Y. Sun, Z. Ju, T. Yao, C. Wang, H. Ju, J. Zhu, S. Wei and Y. Xie, *Angew. Chem., Int. Ed.*, 2017, **56**, 9121–9125.

268 X. Yuan, Y. Luo, B. Zhang, C. Dong, J. Lei, F. Yi, T. Duan, W. Zhu and R. He, *Chem. Commun.*, 2020, **56**, 4212–4215.

269 A. Zhang, Y. Liang, H. Li, X. Zhao, Y. Chen, B. Zhang, W. Zhu and J. Zeng, *Nano Lett.*, 2019, **19**, 6547–6553.

270 L. P. Chi, Z. Z. Niu, X. L. Zhang, P. P. Yang, J. Liao, F. Y. Gao, Z. Z. Wu, K. Bin Tang and M. R. Gao, *Nat. Commun.*, 2021, **12**, 1–9.

271 J. Feng, H. Gao, J. Feng, L. Liu, S. Zeng, H. Dong, Y. Bai, L. Liu and X. Zhang, *ChemCatChem*, 2020, **12**, 926–931.

272 W. Ma, S. Xie, X. G. Zhang, F. Sun, J. Kang, Z. Jiang, Q. Zhang, D. Y. Wu and Y. Wang, *Nat. Commun.*, 2019, **10**, 1–10.

273 C. T. Altaf, T. O. Colak, E. Karagoz, J. Wang, Y. Liu, Y. Chen, M. Liu, U. Unal, N. D. Sankir and M. Sankir, *ACS Omega*, 2024, **9**(17), 19209–19218.

274 J. E. Pander, J. W. J. Lum and B. S. Yeo, *J. Mater. Chem. A*, 2019, **7**, 4093–4101.

275 Z. Zhang, C. Liu, J. T. Brosnahan, H. Zhou, W. Xu and S. Zhang, *J. Mater. Chem. A*, 2019, **7**, 23775–23780.

276 J. Z. Zhen, J. X. Liu, T. Y. Chen, F. Shi, Y. N. Dai, B. Yang, Y. F. Li, X. Wang, T. G. Nong, Y. Q. Hu and J. Shi, *J. Alloys Compd.*, 2019, **771**, 994–999.

277 C. Li, G. Shen, R. Zhang, D. Wu, C. Zou, T. Ling, H. Liu, C. Dong and X. W. Du, *J. Mater. Chem. A*, 2019, **7**, 1418–1423.

278 Y. Song, Y. Wang, J. Shao, K. Ye, Q. Wang and G. Wang, *ACS Appl. Mater. Interfaces*, 2022, **14**(18), 20368–20374.

279 H. il Nam, K. Ryeol Park, Y. W. Choi, H. Ji Sim, K. Yong Sohn and D. H. Lim, *Appl. Surf. Sci.*, 2023, **612**, 155646.

280 A. Aljabour, H. Coskun, X. Zheng, M. G. Kibria, M. Strobel, S. Hild, M. Kehrer, D. Stifter, E. H. Sargent and P. Stadler, *ACS Catal.*, 2020, **10**, 66–72.

281 C. Simon, J. Zander, T. Kottakkat, M. Weiss, J. Timm, C. Roth and R. Marschall, *ACS Appl. Energy Mater.*, 2021, **4**, 8702–8708.

282 S. Zhao, S. Guo, C. Zhu, J. Gao, H. Li, H. Huang, Y. Liu and Z. Kang, *RSC Adv.*, 2017, **7**, 1376–1381.

283 D. Tetzlaff, K. Pellumbi, K. Junge Puring, D. Siegmund, W. S. K. Polet, M. P. Checinski and U. P. Apfel, *ChemElectroChem*, 2021, **8**, 3161–3167.

284 K. Pellumbi, M. Smialkowski, D. Siegmund and U. P. Apfel, *Chem. – Eur. J.*, 2020, **26**, 9938–9944.

285 T. J. Wang, W. S. Fang, Y. M. Liu, F. M. Li, P. Chen and Y. Chen, *J. Energy Chem.*, 2022, **70**, 407–413.

286 C. Xia, X. Wang, C. He, R. Qi, D. Zhu, R. Lu, F. M. Li, Y. Chen, S. Chen, B. You, T. Yao, W. Guo, F. Song, Z. Wang and B. Y. Xia, *J. Am. Chem. Soc.*, 2024, **146**(29), 20530–20538.

287 J. Qiao, Y. Liu, F. Hong and J. Zhang, *Chem. Soc. Rev.*, 2013, **43**, 631–675.

288 D. Du, R. Lan, J. Humphreys and S. Tao, *J. Appl. Electrochem.*, 2017, **47**, 661–678.

289 B.-Q. Miao, W.-S. Fang, B. Sun, F.-M. Li, X.-C. Wang, B.-Y. Xia and Y. Chen, *Chin. J. Struct. Chem.*, 2023, **42**, 100095.

290 S. Verma, B. Kim, H. R. M. Jhong, S. Ma and P. J. A. Kenis, *ChemSusChem*, 2016, **9**, 1972–1979.

291 R. Lin, J. Guo, X. Li, P. Patel and A. Seifitokaldani, *Catal.*, 2020, **10**, 473.

292 Y. C. Li, D. Zhou, Z. Yan, R. H. Gonçalves, D. A. Salvatore, C. P. Berlinguette and T. E. Mallouk, *ACS Energy Lett.*, 2016, **1**, 1149–1153.

293 S. A. Al-Tamreh, M. H. Ibrahim, M. H. El-Naas, J. Vaes, D. Pant, A. Benamor and A. Amhamed, *ChemElectroChem*, 2021, **8**, 3207–3220.

294 M. Zeng, W. Fang, Y. Cen, X. Zhang, Y. Hu and B. Y. Xia, *Angew. Chem.*, 2024, **136**, e202404574.

295 H. Veldhuizen, M. Abdinejad, P. J. Gilissen, J. Albertsma, T. Burdyny, F. D. Tichelaar, S. van der Zwaag and M. A. van der Veen, *ACS Appl. Mater. Interfaces*, 2024, **16**, 34010–34019.

296 O. G. Sánchez, Y. Y. Birdja, M. Bulut, J. Vaes, T. Breugelmans and D. Pant, *Curr. Opin. Green Sustainable Chem.*, 2019, **16**, 47–56.

297 C. Oloman and H. Li, *US Pat.*, App. 12/090,052, 2008.

298 D. Ewis, M. Arsalan, M. Khaled, D. Pant, M. M. Ba-Abbad, A. Amhamed and M. H. El-Naas, *Sep. Purif. Technol.*, 2023, **316**, 123811.

299 H. Yang, J. J. Kaczur, S. D. Sajjad and R. I. Masel, *J. CO2 Util.*, 2020, **42**, 101349.

300 M. Jouny, W. Luc and F. Jiao, *Ind. Eng. Chem. Res.*, 2018, **57**, 2165–2177.

301 A. J. Martín, G. O. Larrazábal and J. Pérez-Ramírez, *Green Chem.*, 2015, **17**, 5114–5130.

302 F. Proietto, U. Patel, A. Galia and O. Scialdone, *Electrochim. Acta*, 2021, **389**, 138753.

303 W. Fang, W. Guo, R. Lu, Y. Yan, X. Liu, D. Wu, F. M. Li, Y. Zhou, C. He, C. Xia, H. Niu, S. Wang, Y. Liu, Y. Mao, C. Zhang, B. You, Y. Pang, L. Duan, X. Yang, F. Song, T. Zhai, G. Wang, X. Guo, B. Tan, T. Yao, Z. Wang and B. Y. Xia, *Nature*, 2024, **626**, 86–91.